Title

Fundamental Study on Sulfur Reactions for Energy Storage Applications

Author

Liu, Rongli

Publication Date

2022

UNIVERSITY OF CALIFORNIA

Los Angeles

Fundamental Study on Sulfur Reactions for Energy Storage Applications

A dissertation submitted in partial satisfaction of the

requirements for the degree Doctor of Philosophy

in Chemistry

by

Rongli Liu

2022

ABSTRACT OF THE DISSERTATION

Fundamental Study on Sulfur Reactions for Energy Storage Applications

by

Rongli Liu

Doctor of Philosophy in Chemistry

University of California, Los Angeles, 2022

Professor Xiangfeng Duan, Chair

High performance energy storage technologies are being developed to more effectively utilize renewable energies, as a result of the steadily expanding energy consumption for portable electronics and electric cars. Batteries with sulfur cathodes have attracted a lot of attention due to their inexpensive cost and great charge storage capacity. Polysulfide shuttling, the main issue in metal sulfur batteries, results in significant sulfur loss and quick deterioration. Despite significant efforts being devoted to improving their performance, the chemical pathway and shuttling mechanism in lithium/sodium sulfur batteries are still up for debate. In order to better mitigate the polysulfide shuttling issue, this work intends to examine the sulfur reaction mechanism and deposition behavior from a fundamental perspective. Additionally, effective catalysts can offer

adequate active sites to improve the kinetics of sulfur reactions during charge/discharge, speeding up the conversion of polysulfides and reducing polysulfide accumulation that results in shuttling. To determine how catalysts affect the reaction network and battery performance, various catalysts are examined. This information could be employed to guide the rational design of the catalysts for sulfur cathodes in the future.

In this work, **Chapter 1** provides a background introduction for the tasks that follow. The behavior of sulfur deposition and basic reaction mechanisms such as the shuttling mechanism and molecular pathway in lithium sulfur batteries, were studied in **Chapter 2** and **Chapter 3** using heteroatom doped holey graphene frameworks as the modeling system. After building a systematic methodology to comprehend the reaction mechanism by combining electrochemistry (cyclic voltammetry), *in situ* Raman, and density functional theory, we further analyzed different catalysts in **Chapter 4** and **Chapter 5**, including different heteroatom doped holey graphene frameworks and nitrogen doped mesoporous carbon materials. Finally, in **Chapter 6**, we took a step forward from lithium to sodium, and demonstrated a useful technique for separator modification to reduce polysulfide shuttling in sodium sulfur batteries.

These findings attempt to address the shuttling issue by studying the fundamental reaction mechanism in metal sulfur batteries and would be very helpful as a blueprint for creating the next generation high energy density batteries.

The dissertation of Rongli Liu is approved.

Ximin He

Richard B. Kaner

Jeffrey I. Zink

Xiangfeng Duan, Committee Chair

University of California, Los Angeles 2022

Dedicated to my family and friends.

TABLE OF CONTENTS

LIST OF FIGURES

LIST OF TABLES

ACKNOWLEDGMENTS

First and foremost, I'd like to thank my advisor, Prof. Xiangfeng Duan. Words cannot express how grateful I am to him for his invaluable advice, unwavering support, and patience throughout my PhD journey. Thank you for being such a fantastic advisor who always keeps me on the right track in science. I would never have gotten this far without your assistance. I would also like to thank Prof. Yu Huang for the technical support on my project, as well as my committee members, Prof. Jeffrey Zink, Prof. Richard Kaner, and Prof. Ximin He, for their help and advice with my PhD study. Special thanks go to Dr. Johnny Pang; it has been such a wonderful time teaching with you! I'd also like to take this opportunity to thank a few staffs in the chemistry department for all of their help throughout my PhD. Thank you Ignacio for all the technical support for my project and MCTP. Thanks to Maria and Zanita in the lab support, I was able to fix any issue that arose during my instruction. I also want to thank chemical store and the graduate office for their assistance with my research and general business. I feel so lucky to be surrounded by all these lovely people who have supported me on my trip.

I would also like to express my gratitude to all the SCALAR members. Special thanks to Prof. Philippe Sautet and Ziyang for their great computation help on my projects. Thank you to Prof. Ram Seshadri, Prof. Kimberly See, Arava, and Joshua for their help on the Raman data collection. And I would like to express my gratitude to Prof. Sarah Tolbert, Prof. Bruce Dunn, and Prof. Brad Chmelka for their insightful comments on my research on T3 meetings.

I am extremely grateful to all of my labmates. I want to thank Lele and Dan for being such an incredible mentor and for introducing me to the battery field and teaching me all the necessary knowledge and skills. Thank you Frank, Dan, Wang, Leyuan, Shuanghao, and Zhuoying for all the insightful discussions. I would like to thank every member in the Duan lab. My time studying and living at UCLA has been fantastic thanks to their thoughtful assistance and support.

Next, there are a few people special to me that I would like to thank: RDJ, JD, CJ, AL, WL, GA, YCF, WZ, JM, ZJY, and BBB. Without you, I would not have survived such a challenging period in my life. I also appreciate all of my friends' support. Danyang, Shaoshuang, Lu, Xinyi, Kejing, Xun, love you all! You are always there for me when I need someone to share my joys and struggles with. And I must express my heartfelt gratitude to my parents and family for their unceasing support and encouragement throughout my years of study. I could not have undertaken this journey without you.

VITA

2017	Bachelor of Science in Chemistry Peking University Beijing, China

Previous Publications and Contributions of Co-Authors

Chapter 2, 3, and **4** are a version of:

Title: Deciphering the reaction networks for the sixteen-electron sulfur reduction reaction.

Authors: Rongli Liu, Ziyang Wei, Lele Peng, Arava Zohar, Rachel Schoeppner, Peiqi Wang, Chengzhang Wan, Dan Zhu, Haotian Liu, Zhaozong Wang, Sarah Tolbert, Bruce Dunn, Yu Huang, Philippe Sautet, and Xiangfeng Duan.

Status: In preparation for publication.

Chapter 5 is a version of:

Title: Correlated atomic-scale compositions, structures, and reduction activities of non-precious-metal mesoporous N-carbon electrocatalysts.

Authors: Shona M. Becwar, Zachariah J. Berkson, Niels P. Zussblatt, Ziyang Wei, Philipp Selter, Lele Peng, Rongli Liu, Walter Rosas Arbelaez, Anders E. C. Palmqvist, Xiangfeng Duan, Nina Fechler, Philippe Sautet, and Bradley F. Chmelka.

Status: In preparation for publication.

Chapter 6 are some preliminary results for a new project where all experiments were performed by me.

CHAPTER 1: INTRODUCTION AND BACKGROUND

1.1 Batteries for Energy Storage Applications

1.1.1 Energy Storage Devices

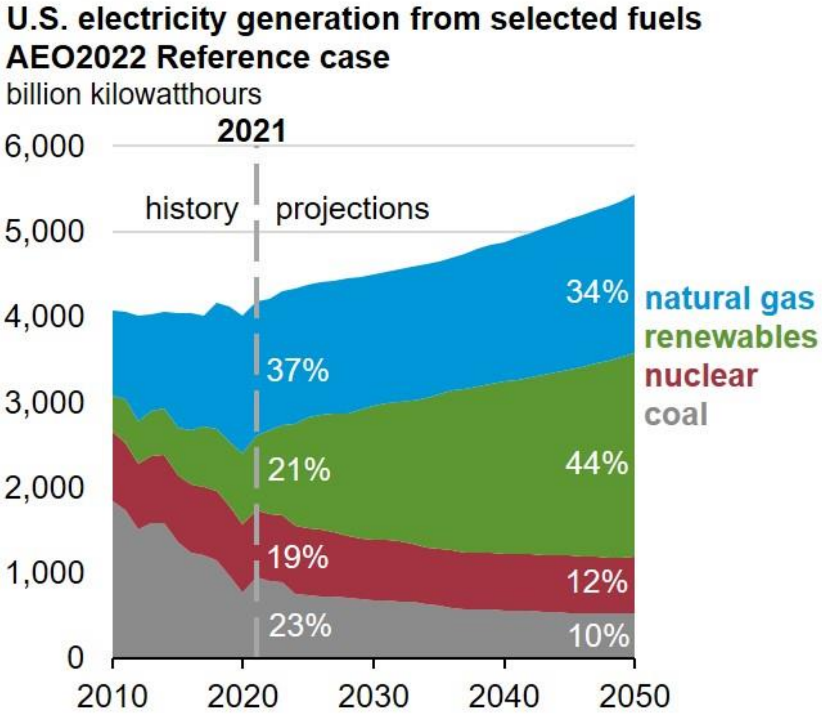

Figure 1. U.S. electricity generation and shares for selected fuels.[1]

Global economic development and growth are closely correlated with rising energy usage. According to the U.S. Energy Information Administration (EIA), the U.S. Department of Energy forecasted that the country's power consumption will reach a record high of 4,045 billion kilowatt-hours (kWh) in 2023.[1] However, the over use of non-renewable resources for power generation, like fossil fuels, has a detrimental effect on both the environment and human health. Renewable energy sources such as wind, solar, geothermal energy, and hydropower are considered as attractive substitutes for a greener future.[2-4] As said by EIA projections, during the period 2022-2050, the share of renewable energy in total power generation will rise from 21% to 44%, while the continued retirement of fossil fuels is denoted by to its decrease from 60% to 44% (**Figure 1**).[1] Renewable energy is replenished naturally and thus will never deplete, allowing us to solve the climate problem once and for all; however, it is strictly limited in time and location.[2,4] As a result, there has never been a greater need for the development and promotion of next-generation energy storage devices.

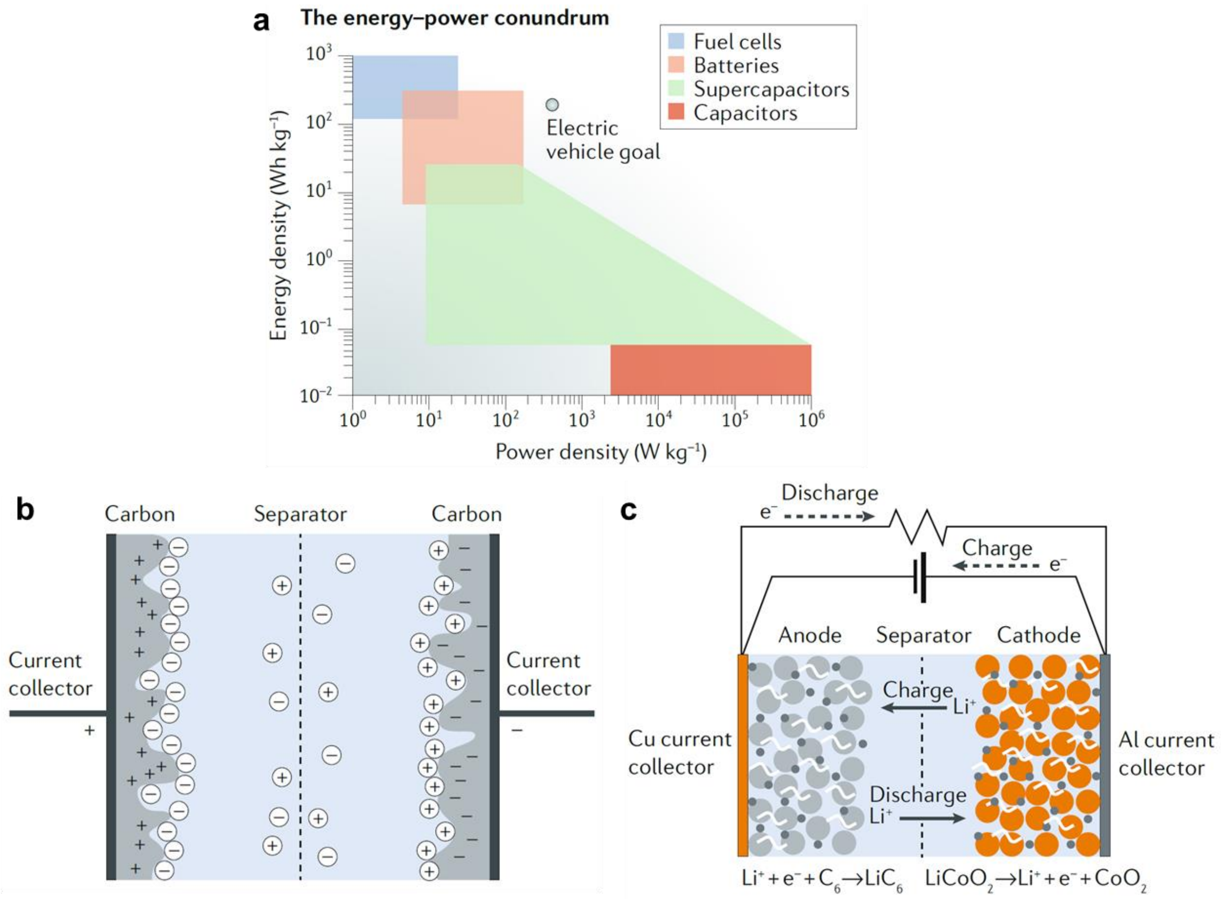

Figure 2. Various categories of energy storage devices. **a,** A Ragone plot of energy storage technologies. **b,** Schematic diagram of an electrical double layer supercapacitor. **c,** Schematic diagram of a conventional Lithium ion battery.[5]

By plotting the energy density versus power density, the Ragone figure in **Figure 2** compares the four basic categories of energy storage devices: capacitors, supercapacitors, batteries, and fuel cells. Power density is the rate at which energy is transferred, whereas energy density refers to how much energy a device can store. For instance, power displays how quickly a vehicle can move while energy decides how far it can travel. In an ideal energy storage device, high power density and high energy density exist simultaneously.[6] However, because of the built-in charge storage mechanism, it is usually extremely difficult to meet these two requirements at the same time. Due to their superior energy or power density, batteries and supercapacitors are the two most researched and commercialized energy storage systems among all the categories.[5] Conventional capacitors contain two electrical conductors with a dielectric medium sandwiched in between. Charge accumulation is caused by an electric field, which results in capacitance. Supercapacitors utilize highly porous materials with a large surface area to dramatically increase charge storage ability. Electrostatic double-layer capacitors and electrochemical pseudocapacitors, two common categories of supercapacitors, are both based on surface processes, either charge adsorption/desorption or faradaic reactions. As a result, supercapacitors have a high power density and are widely used in applications that require fast charge/discharge and short-term storage.[7] Batteries, on the other hand, store energy through ion intercalation or chemical reactions deep within the crystal lattice. Despite the fact that power density is sacrificed as a result of slower ion diffusion, the extremely high energy density that batteries can achieve encourages their use in large-scale applications ranging from automobiles to microchips.[5,8]

1.1.2 Batteries

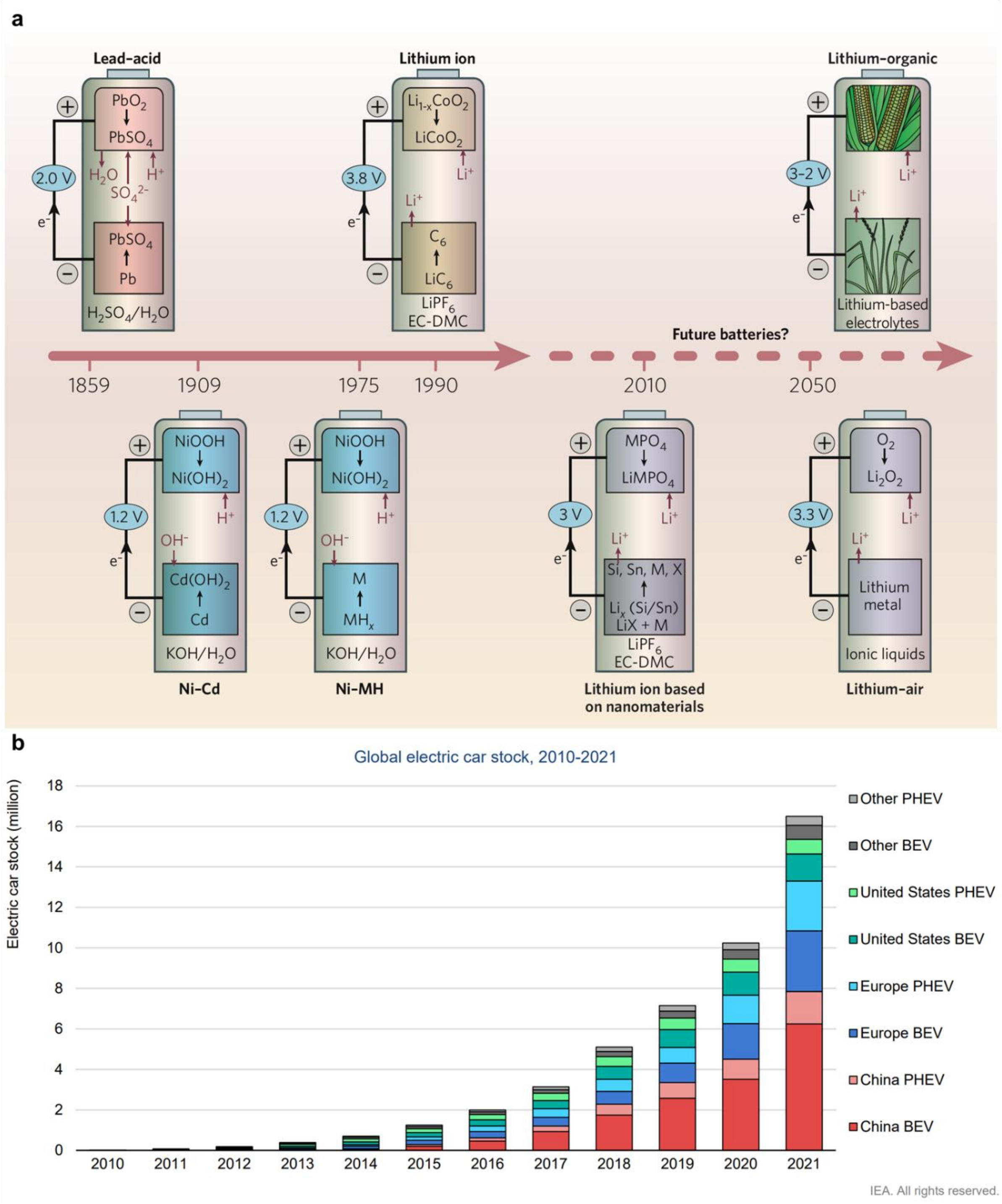

Figure 3. Battery history and the expanding global market for electric vehicles. **a**, The history of battery over years.[8] Some significant advancements include lead-acid, Ni-Cd, Ni-MH, and Lithium ion batteries. **b**, The emerging global EV markets in the past decade.[9] Electric vehicles are becoming more prevalent worldwide, not just in America.

Alessandro Volta created the first Zn-Cu battery in 1800, which marks the beginning of battery history. Following that, lead-acid batteries, one of the oldest and most durable rechargeable batteries, were invented, and they continue to hold a significant market share today. Despite their low cost and high recycling rate, they are not competitive in portable applications due to their low energy density and short lifespan.[10] The Ni-Cd and Ni-MH alkali batteries that were later developed have low energy and a slow charge rate, as well. Therefore, a more compact, safe energy storage solution with a higher energy density was required to meet the extensively spread of and continually rising demand for portable electronics and electric cars. Since Sony released its first commercial lithium ion battery in 1991, a new era has begun with the advent of a mobile world made possible by cutting-edge batteries. The safety problem with lithium cobalt oxide ($LiCoO_2$) was substantially resolved along with the breakthrough of nanoscale lithium iron phosphate ($LiFePO_4$) in the 1990s, and lithium ion batteries began to emerge everywhere in the world, from phones to computers to cars to grid energy storage.[8,10] John B. Goodenough, M. Stanley Whittingham, and Akira Yoshino received the 2019 Nobel Prize in Chemistry in recognition of their dedication to the advancement of the lithium-ion battery and to acknowledge the significance of lithium-ion batteries. The growth of lithium ion batteries also promoted the advent of electric vehicles, as a solution for sustainable development. The American government unveiled a number of plans to increase domestic production of EV batteries and power clean energy technologies in order to meet the country's goal of being carbon neutral by 2050. For instance, the Bipartisan Infrastructure Law awarded around $3 billion in February 2022 to 20 businesses spread across 12 states for advanced battery supply chains.[9] Within the past decade, the EV market has experienced incredible growth not just in America but also globally (**Figure 3b**). A sustainable energy revolution is taking place thanks to new batteries' continually improving capabilities.

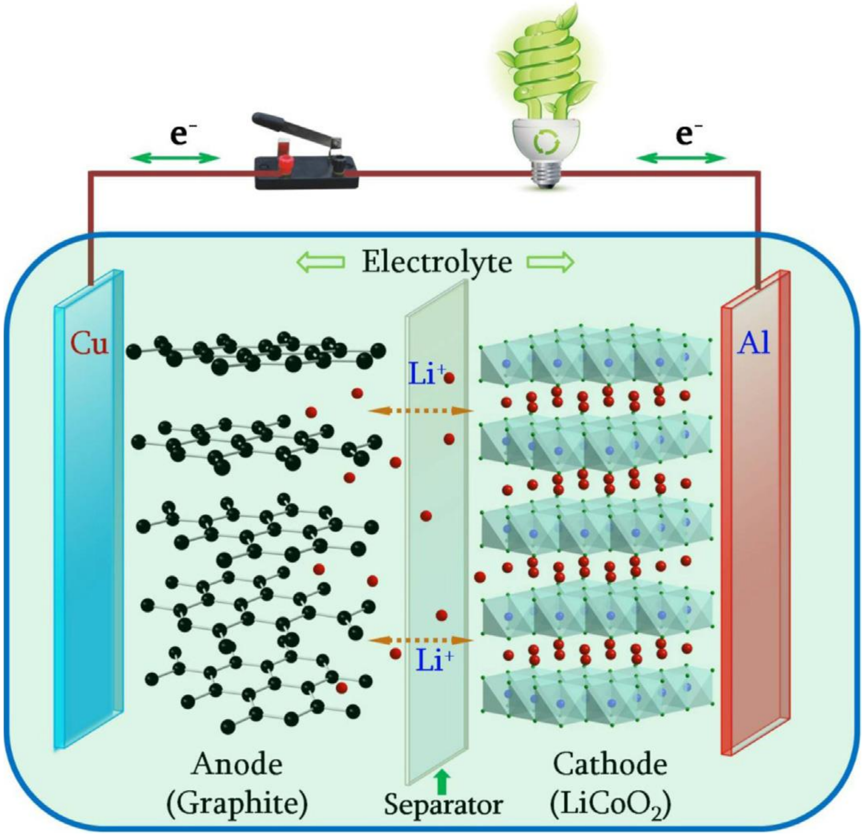

Figure 4. A schematic showing how rechargeable Li-ion batteries work.[11]

As shown in **Figure 4,** a common "rocking chair" lithium ion battery contains a graphite anode, a layer-structured $LiCoO_2$ cathode, and a separator in between. Electrolyte connecting cathode and anode allows for lithium ion transportation back and forth between two electrodes.[11] During the charge process, Li ions are stripped away from the cathode and intercalated into the anode; the opposite reaction takes place during the discharge process. Both graphite and $LiCoO_2$ are layered substances that enable lithium to intercalate, which results in the storage of energy. Different chemical potential between the cathode and anode when linked to an external device causes electrons to flow via the external circuit to produce electrical energy.[8,11,12]

Coulometric capacity is a measure of a battery's total ampere-hours when it is completely discharged. The following equation can be used to compute theoretical specific capacity:

$$C = \frac{\mathrm{nF}}{3600\mathrm{Mw}}$$

Equation 1

Where C = Specific Capacity (mAh g^{-1})

n = number of electrons

F = Farady constant (96485 s A mol^{-1})

Mw = molecular weight of the material (g mol^{-1})

Due to numerous losses in the practical configuration, experimental capacity is often lower than the theoretical limit. Galvanostatic charge discharge (GCD) is a common battery performance testing method in which the battery is cycled at a specific current in a specific voltage window. The cycling time for each cycle represents the amount of time required to achieve a full charge/discharge. The experimental specific capacity (mAh g^{-1}) can be calculated by multiplying the discharge current I (in Amps) and the discharge time t (in hours), then dividing by the electrode's mass M (in grams):

$$C = \frac{It}{\mathrm{M}}$$

Equation 2

Furthermore, one can obtain the gravitational energy density by multiplying the voltage by the specific capacity (Wh kg^{-1}):

$$E = C \times V$$

Equation 3

When displaying the performance of batteries, C-rate is commonly used to characterize the discharge current to normalize the battery capacity between different batteries. 1C implies discharging the battery to its full theoretical capacity in one hour. When testing at a high C-rate, slower ion transport speed and shallow intercalating depth result in worse cycle stability. C-rate is related to the internal resistance of the battery as well. Internal resistance includes ohmic internal resistance and polarization internal resistance, the latter of which can be further divided into electrochemical polarization internal resistance and concentration polarization internal resistance. Larger resistance at high C rates tends to impede the movement of ions and electrons, eventually reducing battery life.[4,13]

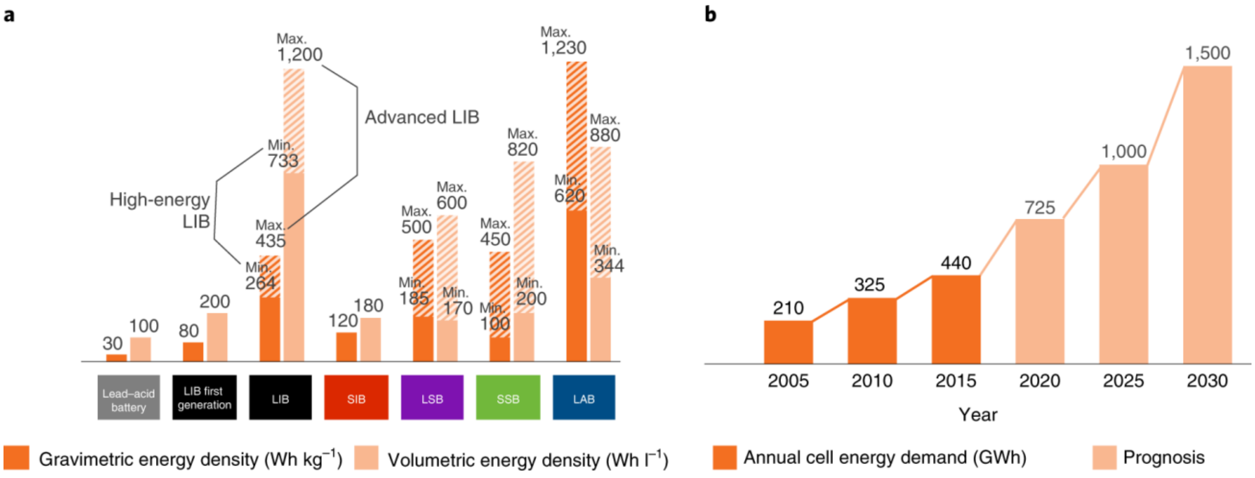

Figure 5. Volumetric and gravimetric energy densities for practical technologies, as well as the growth of the rechargeable battery market over time.[14] **a,** Gravimetric and volumetric energy densities for different kinds of batteries in practical cell level. For LIB, the minimum value is obtained from current high-energy LIB cell, and the maximum value from advanced LIB configuration (for example, cell with a silicon-based anode). For lithium-metal-based systems, prototype cell data for SIB, LSB, SSB, and LAB are provided, along with minimum and maximum values. **b,** Market growth for rechargeable batteries from 2005 to 2030.

Despite significant resources (both human and financial) being invested in lithium ion battery research and development, conventional commercial lithium ion batteries continue to have drawbacks such as limited energy density, rising costs, and safety concerns. The mostly used anode material, graphite, has a capacity limit of 372 mAh g^{-1}.[15] The nickel-cobalt-manganese (NCM) ternary cathode material's capacity as of right now is less than 200 mAh g^{-1}.[16] Thus, the search for innovative battery components has never stopped. Inferring from **Equation 3**, high capacity and a wide voltage window are believed to be the two key areas of battery research in order to obtain high energy density.

Table 1. Comparison of different anode materials in lithium ion batteries.[17]

Materials	Li	C	Si	Sn	Sb	Al	Mg
Density (g cm^{-3})	0.53	2.25	2.3	7.3	6.7	2.7	1.3
Lithiated phase	Li	LiC_6	$Li_{4.4}Si$	$Li_{4.4}Sn$	Li_3Sb	LiAl	Li_3Mg
Theoretical specific capacity (mAh g^{-1})	3862	372	4200	994	660	993	3350
Volume change (%)	100	12	420	260	200	96	100
Potential versus Li (V)	0	0.05	0.4	0.6	0.9	0.3	0.1

In recent decades, silicon and lithium metal have distinguished themselves as a possible substitute for graphite anode. As shown in **Table 1**, silicon has the highest theoretical capacity of 4200 mAh g^{-1} and a relatively low delithiation voltage when compared to other anode materials.[18] This, combined with its abundance and environmental friendliness, has piqued the interest of academic and industry researchers.[17,19,20] With the development of nanotechnology, the major issue with silicon electrodes, fast degradation during cycling due by volume change, has made significant strides, and silicon carbon negative anodes have begun to be produced on a commercial scale.[21] Another area of interest for battery research at the time was lithium metal anode, which has one of the greatest capacities.[22] The potential difference between cathode and anode determines the voltage window. With the lowest potential among all metal electrodes, -3.04 V versus standard hydrogen electrode (SHE), lithium is thought to be able to build the largest voltage window in a battery.[23] The unstable solid electrolyte interphase (SEI) on the electrode surface, however, results in dendrites, drastically reduces cycle life, and raises safety issues including fire and explosion.[24] In-depth research on SEI is still required before lithium metal anode may be used in practical applications.

Table 2. Comparison of several kinds of batteries based on different electrochemical reactions.[25]

Battery	Cell voltage (V)	Theoretical specifc energy (Wh kg^{-1})	Theoretical energy density (Wh L^{-1})
Li-ion	3.8	387	1015
Zn-air	1.65	1086	6091
Li-S	2.2	2567	2199
Li-O_2 (non-aqueous)	3.0	3505	3436
Li-O_2 (aqueous)	3.2	3582	2234

On the cathode side, sulfur and oxygen have both been studied in great detail. They are seen to be one of the most promising choices to advance energy storage systems since they can offer both a high energy density and low cost.[25] Despite the noteworthy accomplishment, difficulties still exist. They have several issues regarding both the electrodes and electrolytes leading to their limited cycle life that need to be solved before being produced on a wide scale. For instance, the bottleneck problems of lithium air batteries include electrolyte decomposition caused by oxygen species attack and high voltage, together with related side reactions that would produce cathode inactivation. For the lithium anode, there is an urgent need for safety precautions since the lithium anode is susceptible to severe corrosion from H_2O and its byproducts. High-performance Li-air batteries need to have all of its components function simultaneously.[26-28] As for lithium sulfur battery, although it has been investigated in greater detail, there are also still several issues. As one of our primary research areas of interest, it will be covered in more detail in the following section and more mechanism study will be displayed in **Chapter 2-5**.

In addition, sodium is viewed as a potential replacement for lithium due to its abundance and the rising price of lithium material.[29-31] However, sodium ion batteries differ greatly from lithium ion batteries due to the larger size of sodium ions, therefore they have not yet attained the required level of performance for commercial use. To completely comprehend the fundamental issues and solutions, more thorough research is required for both sodium ion batteries and sodium metal anode batteries.[10,32] We will talk about sodium sulfur batteries in **Chapter 6** where we will investigate the prospect of replacing lithium in metal sulfur batteries with sodium.

1.2 Metal Sulfur Batteries

1.2.1 Lithium Sulfur Batteries

Although the notion of lithium sulfur (Li-S) battery has recently come to light, research on them dates back to the 1960s.[33] The amount of time spent on the relevant research can show how challenging it will be to develop a commercial Li-S battery. Li-S batteries have lately returned to the forefront of the battery industry thanks to the boom of research on the next generation of high energy density batteries. As shown in **Figure 6a**, a Li-S battery consists of a lithium anode and a sulfur cathode, together with a separator made of a porous polymer (usually polypropylene) and a particular electrolyte (most commonly the ether electrolyte LiTFSI/DOL/DME) for transporting lithium ions.[34,35] Unlike commercialized lithium ion batteries, which rely on lithium ion intercalation and do not involve any chemical reactions, Li-S batteries are based on the reaction between lithium and sulfur. As a cathode, during discharge, sulfur in the form of S_8 molecules is reduced into Li_2S by obtaining electrons from the external circuit and lithium ions from the internal electrolyte. The lithium anode, on the other side, loses electrons that enter the external circuit and release lithium ions into the electrolyte to maintain lithium ion equilibrium in the solution. Operating backwards, When the battery is charged, lithium ions in the electrolyte capture electrons and deposit as lithium metal on the lithium anode. In the meantime, Li_2S loses electrons and lithium ions and is oxidized, depositing as S_8 on the cathode side.

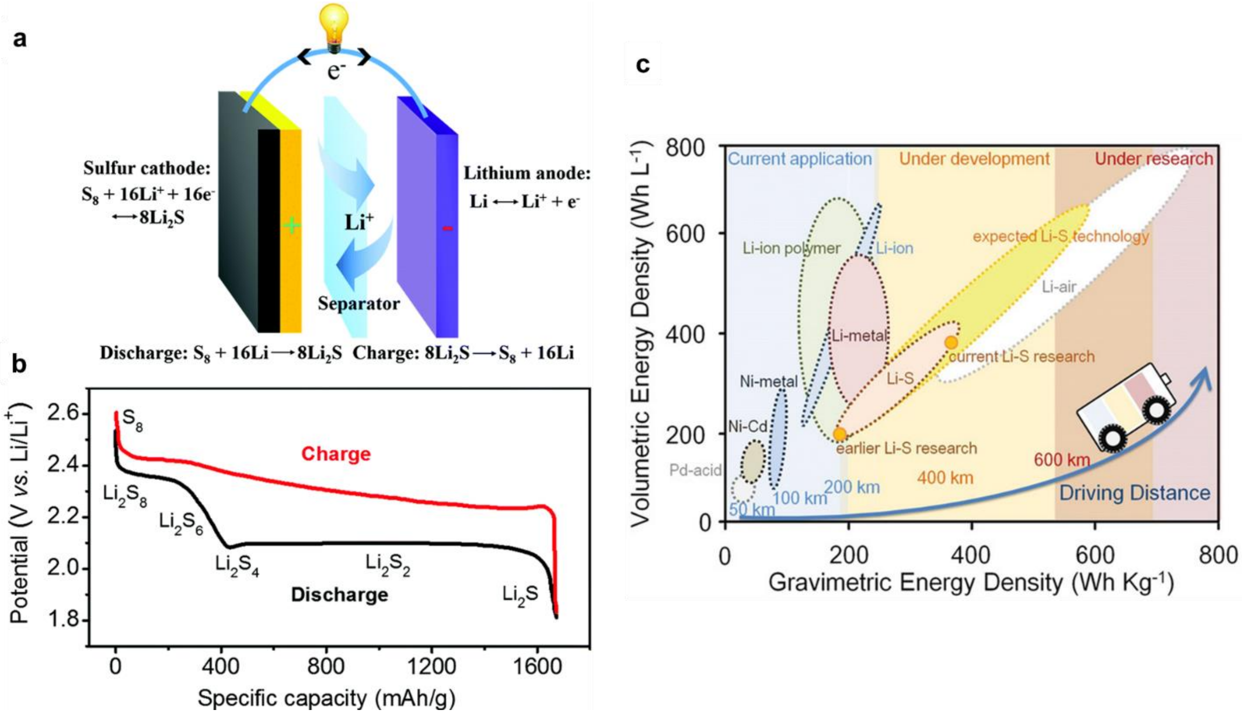

Figure 6. Configuration, reaction and energy density of Li-S battery. **a,** Schematic of the electrochemical reactions and working mechanism in Li-S batteries. **b,** A typical Li-S battery charge/discharge voltage curve with two plateaus in ether-based electrolytes. **c,** Batteries for future market. Li-S batteries are predicted to have a bright future in enhancing the capabilities of electric vehicles.[35,36]

Because of its abundant natural resources, sulfur is extremely cheap (you can purchase 200 tons of sulfur for the price of one ton of cobalt), making it an appealing nontoxic material for use in batteries. Additionally, sulfur maintains a high theoretical specific capacity of 1672 mAh g^{-1}, which, if completely utilized, is roughly 8 fold greater than the present lithium-ion batteries.[25,34,37,38] The lithium metal anode, on the other end, not only has a high theoretical specific capacity of 3862 mAh g^{-1} but also has the lowest reduction potential, which can increase the voltage window and significantly boost the energy density.[23] Consequently, lithium-sulfur batteries show great promise as the next generation of high-energy batteries.

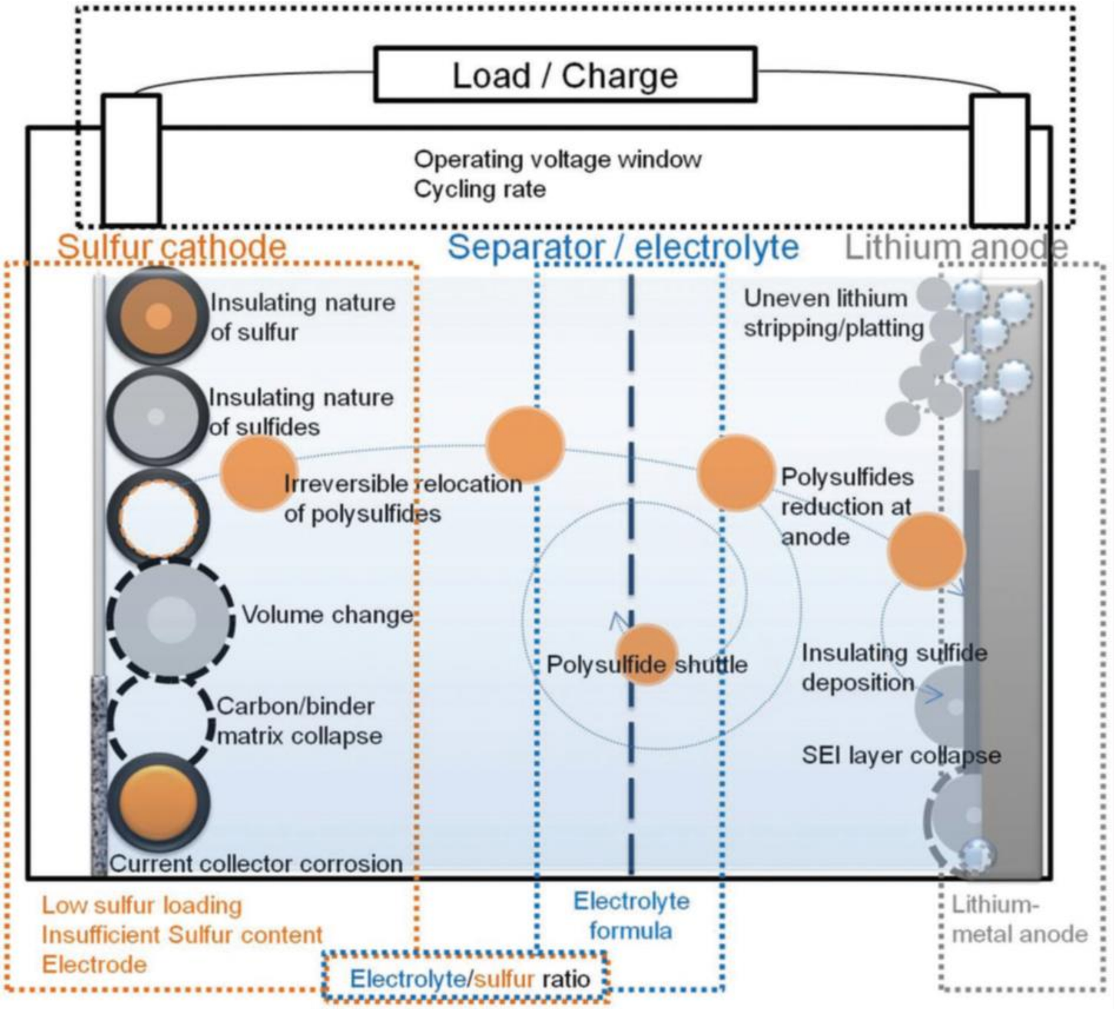

Figure 7. Lithium-sulfur batteries have both intrinsic material issues and external cell-assembly difficulties.[36]

Despite the great hopes that people have for Li-S batteries, several key challenges hindered the commercial applications of Li-S battery.[36] A basic concern of sulfur cathode is the poor electrical conductivity of both S_8 and Li_2S. Huge overpotential is introduced especially in the beginning of the reaction as a consequence of bad electron conduction and ion diffusion to access all the active sites in the electrode. Li_2S has a low tendency to initiate reactions, which passivates the cathode surface and results in inadequate utilization of the active material.[39]

What's more, there is another aspect, volume change, that must be taken into account while designing the sulfur host. Because of the chemical reactions taking place in the battery, ions do not simply do intercalations like that in lithium ion batteries; Instead, a chemical reaction occurs between S_8 (2.03 g cm^{-3}) and Li_2S (1.66 g cm^{-3}), resulting in an ~80% volume expansion. Considerable volume change causes structure pulverization and an increase in dead sulfur, eventually leading to cell failure.[40]

The notorious shuttling problem, for which people have long been persecuted, is one of the most serious challenges with Li-S batteries. Sulfur is gradually reduced to Li_2S during discharge, passing through a number of distinct lithium polysulfide (LiPS) intermediates. Sulfur and Li_2S cannot be dissolved in the commonly used ether electrolyte, while the LiPSs can be easily dissolved. This leads to the loss of active sulfur, since LiPSs have a tendency to diffuse to the lithium anode and react with lithium there to produce lower order polysulfides or Li_2S, which could then either deposit on lithium metal or diffuse back to the cathode side. During charge, lower order polysulfides that have diffused back from the anode may participate in the oxidation on cathode and either be oxidized back to S_8 or be oxidized into higher order polysulfides that may return to the lithium anode once again. This leads to a LiPS transportation back and forth between cathode and anode, eventually building an equilibrium which is observed as a "overcharge" phenomenon in charge discharge cycling, and lowering coulombic efficiency. The significant loss of sulfur during shuttling reduces cycle life and speeds up cell degradation.[40-42]

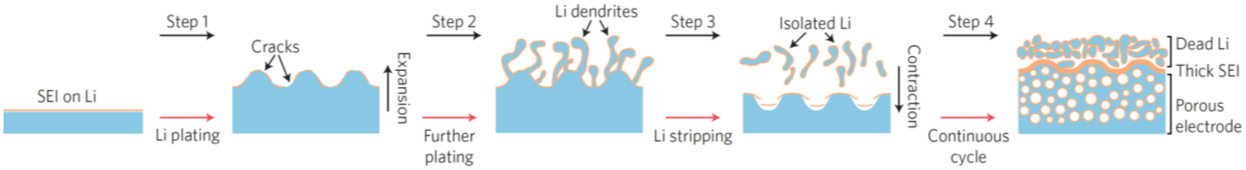

Figure 8. Schematic showing the process of Li plating and stripping.[24] Step 1: Volume expansion brought on by lithium plating breaks the SEI film. Step 2: Li dendrites emerge from the cracks as further plating is applied. Step 3: Li stripping results in detached Li that joins the "dead" Li, while volume contraction causes additional SEI fracture. Step 4: Steps 1-3 are repeated as a result of continuous cycling, which eventually leads to an accumulation of dead Li, thick SEI, and porous Li electrode.

Last but not least, because Li-S batteries contain lithium metal as an anode, all of the disadvantages associated with lithium metal electrodes exist in Li-S batteries, which are primarily caused by unstable dendrites. SEI is a layer formed by electrolyte decomposition at the interface of a solid electrode and a liquid electrolyte. Ideal SEI allows for easy diffusion of lithium ions but is not conductive to prevent further electrolyte decomposition. However, the huge volume change from lithium ions (0%) to lithium metal (100% lithium plating) causes cracks on the fresh SEI and dendrite growth from the cracks. The dendrites become isolated dead lithium during the subsequent lithium stripping. In the following cycle, new SEI continue to form on the fresh lithium surface. After cycles, the lithium anode becomes a porous electrode with a thick SEI and a large amount of dead lithium on top, which blocks ion diffusion, causes substantial loss on active lithium, and causes safety issues due to sharp dendrites.[24] As a result, commercialization of Li-S batteries is not possible unless a secure method of using lithium metal as an anode is developed.

1.2.2 Advancements in Lithium Sulfur Batteries

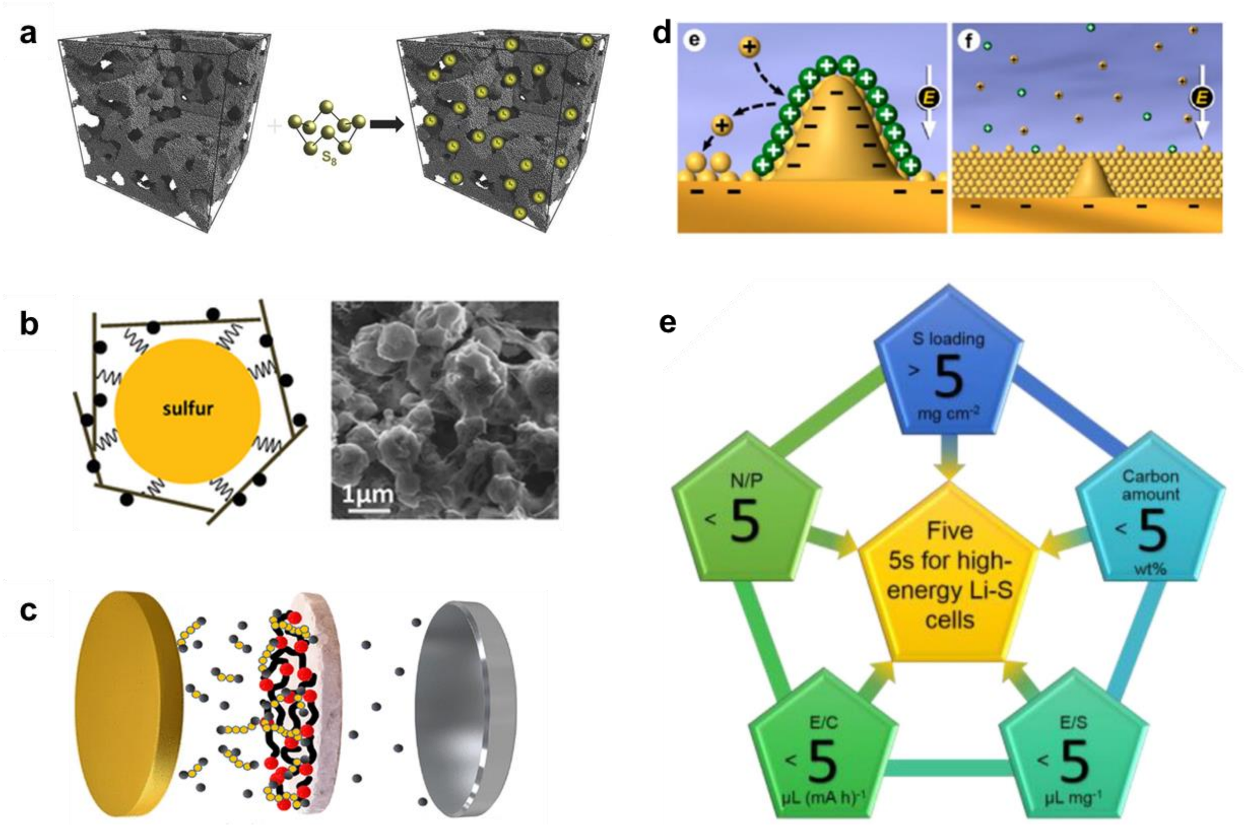

Figure 9. Tremendous effort for solving the problems in Li-S battery. **a,** Conductive carbon mixed with sulfur to improve the conductivity of insulating S_8 and Li_2S.[43] **b,** Flexible host in sulfur cathode to control the volume change.[44] **c,** Physically blocking or catalysis strategy to mitigate the shuttling of polysulfides.[45] **d,** Methods to suppress lithium dendrites on lithium metal anode.[46] **e,** "five 5s": the critical metrics that are essential for an ideal Li-S battery meeting the high-energy target of Li-S systems.[37]

Different designs have been taken into consideration to address the aforementioned issues in order to take advantage of the high energy density of Li-S batteries. To enhance the conductivity, some carbon substrates have been introduced as a host for sulfur (**Figure 9a**). Similar to the typical slurry used as electrode in traditional batteries, which blends active elements with carbon black to promote electron transit, mixing with carbon materials can greatly enhance the conductivity of the sulfur cathode. Nearly all kinds of common carbon substrates including carbon black[47], graphite[48], graphene[44,49], carbon nanotubes[50,51], and carbon nanofibers[52,53], have been extensively studied.

When mixed with 2D or 3D carbon materials like graphene[44,54] (**Figure 9b**), the high flexibility and excellent volume tolerant ability provided by the carbon substrate can effectively alleviate the volume extension of sulfur electrodes, which is beneficial for maintaining the electrode integrity and high stability during cycling.

Additionally, porous carbon host or modified separator were used to physically trap LiPSs intermediates in the cathode side (**Figure 9c**), hence reducing shuttling. Numerous modifications on separators[45,55,56] have been explored for their effectiveness in inhibiting LiPSs. Adding polar active sites increases the attractive force for LiPSs;[57] enriching the negative charges on the separator surface pushes negative polysulfides away from the separator, trapping them in the cathode;[58] and introducing catalysts on the separator could also accelerate LiPS conversion, as it does in the cathodes.[59] When applied in real-world applications, functionalization on separators is sometimes easier than on cathode, making it more convenient and cost-effective.

Unfortunately, carbon itself lacks enough active sites to attract sulfur or LiPSs to reduce shuttling, because carbon is a nonpolar substance with low intermolecular force towards polar polysulfides. Therefore, as the development of Li-S technology, the physically blocking strategy is gradually replaced by catalysis, a more effective method for trapping LiPSs.[60]

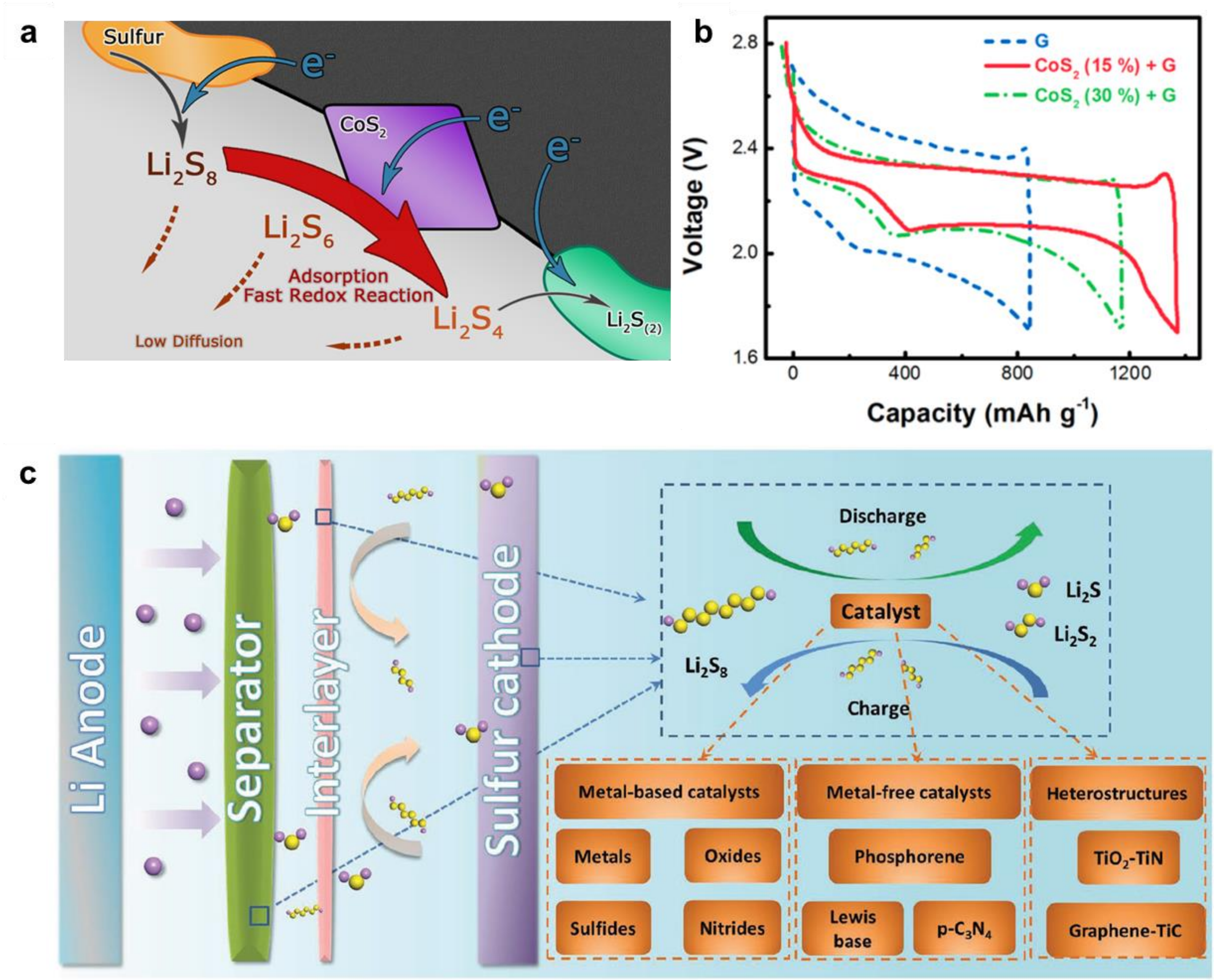

Figure 10. Catalytic strategy for solving LiPS shuttling problem in Li-S batteries. **a,** Schematic showing the CoS_2 as catalysts for LiPS conversion. **b,** GCD curve comparsion between electrodes with CoS_2 and without CoS_2. Electrode with 15% CoS_2 shows the best performance with highest capacity.[61] **c,** Illustration of catalysts in Li-S batteries. The catalysts can be modified on either sulfur cathode or separator, or be independent as an interlayer. Additionally, various different catalysts have been studied for sulfur conversion.[62]

By incorporating catalysts into the sulfur cathode, the modified host with active sites gains more polarity and intermolecular force with LiPSs, enhancing the adsorption of LiPS intermediates and making the cathode more powerful for trapping LiPSs. What’s even more important is that the catalysts are able to speed up the conversion between polysulfides, hence decrease the LiPS accumulation, and mitigate the severe shuttling problem. **Figure 10a and b** show one of the earliest catalytic designs in Li-S batteries based on CoS_2 catalysts. Incorporating sulfiphilic cobalt disulfide (CoS_2) into carbon/sulfur cathodes led to a significant interaction between LiPSs and CoS_2 during operation. Polar polysulfides were strongly adsorbed and activated at the interfaces between CoS_2 and electrolyte, which sped up polysulfide redox processes. In addition to effectively mitigating polarization and increasing energy efficiency by 10%, the high polysulfide reactivity also promised excellent discharge capacity and stable cycling performance for 2000 cycles. At 0.5 C, a high initial capacity of 1368 mAh g^{-1} and a moderate capacity decay rate of 0.034% per cycle was attained.[61] Catalyzing effect has been confirmed in various systems, including the doped heteroatoms on carbon materials[63], single metal atoms[64], metal nanoparticles[65], sulfides[61], oxides[66], phosphides[60], carbides[67], nitrides[68], and borides[69]. In addition, catalyst decoration is not limited to sulfur cathodes; separators and electrolytes can also be used to load catalysts (**Figure 10c**).[62] Catalysts offers an approach to combat the shuttling problem fundamentally and comprehensively.

Figure 11 illustrates the mechanism behind catalytic design. **Figure 11a** shows the activation energy at different voltage during the sulfur reducing process. Due to the low activation energy at high voltage, the initial reduction of sulfur to the soluble LiPSs is relatively simple. However, the subsequent conversion of the LiPSs into the insoluble Li_2S_2/Li_2S has a much higher activation energy, causing the polysulfide accumulation and aggravating the polysulfide shuttling effect. A good catalyst for sulfur conversion reactions should be able to catalytically tailoring reaction kinetics to accelerate the polysulfide conversion process, especially in the low voltage regime where soluble LiPSs are reduced into insoluble sulfides, to improve the conversion efficiency in rate-determining step and combat the polysulfide shuttling effect.[70]

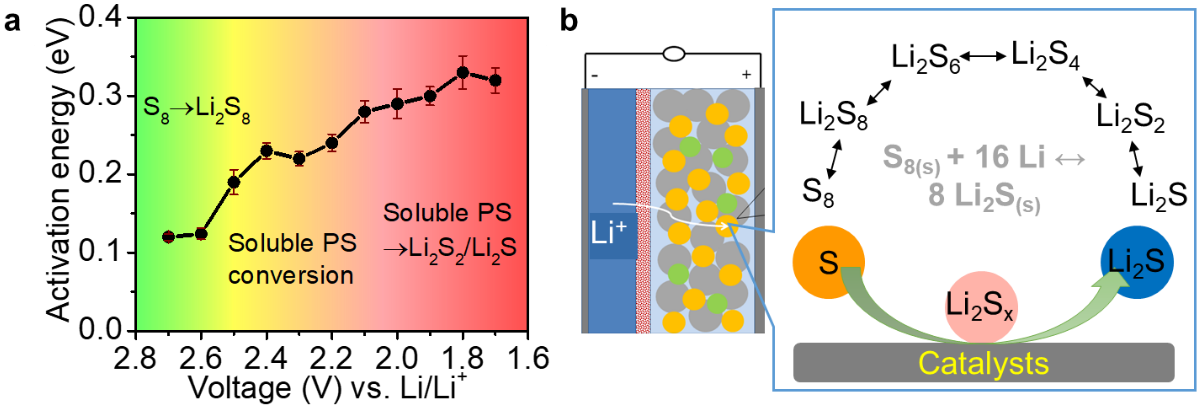

Figure 11. Activation energy and catalytic mechanism in sulfur reduction and polysulfide conversion reaction. **a,** Activation energy profiles at various voltages which confirms the rate-determining step to be the final conversion step, where LiPSs is reduced into insoluble products. The high activation energy explains polysulfide buildup and shuttling.[70] **b,** Catalytic design for sulfur conversion.

The unstable lithium metal anode, as mentioned in the previous section, is another major impediment to the commercialization of Li-S batteries. Multiple solutions have been developed that have considerately improved the lithium metal stability. Electrolyte additives such as Cs^+[46], LiPSs[71,72], and $LiNO_3$[73,74], facilitate the creation of smoother SEI, hence lowering the risk of separator puncture. Surface modification by introducing an extra interlayer prohibits dendrite growth; 2D materials like graphene[75], BN[76], black phosphorus[77], fluorinated reduced graphene oxide[78], and MoS_2[79], can be fabricated into insulating and lithium ion conductive only interlayers serving as artificial SEI, with some of them continuing to function well even after thousands of hours of operation. Besides, graphene-related materials with many lithiophilic sites are drawing a lot of attention recently as a 3D host for lithium metal.[80] The decorated graphene frameworks have several benefits, including countless lithium deposition sites, flexible volume control, and low local current density to minimize the number of dendrites. The lithium metal revolution is still in its early stages, and safety remains the primary concern when constructing a commercial lithium metal cell.

1.2.3 Mechanism Study in Lithium Sulfur Batteries

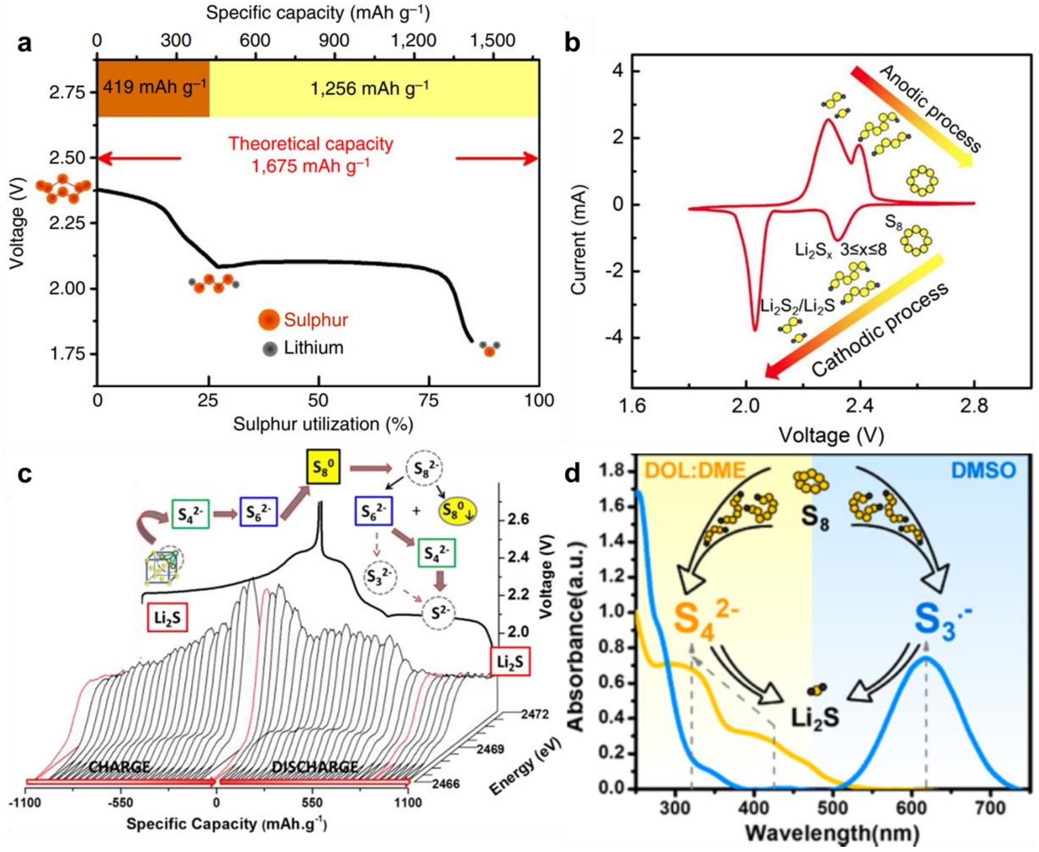

Figure 12. Mechanism investigation in Li-S batteries. **a,** Galvanostatic charge discharge profile of sulfur reduction reaction.[81] **b,** Cyclic voltammetry of sulfur reduction reaction.[82] **c,** Operando X-ray absorption spectroscopy and mechanism proposed for sulfur reaction.[83] **d,** Operando UV-vis spectroscopic study on sulfur redox reactions in different solvents.[84]

In order to more effectively address issues with Li-S batteries, understanding the mechanism is critical for rational cell design, such as catalyst design. However, the fundamental sulfur reduction reaction (SRR) mechanism is still up for discussion, despite some Li-S batteries being able to operate at nearly theoretical capacity in a laboratory environment. Almost all kinds of characterization methods have been performed for analyzing of the reaction mechanism. A molecular level computation work explored the possible reaction pathways based on reduction potentials and Gibbs free energies, and deduced the most likely and abundant intermediates to be

S_8^{2-} and S_3^{2-}.[85] In terms of electrochemistry, galvanostatic charge discharge (GCD) and cyclic voltammetry (CV) are two common approaches for electrochemical reaction investigation. As shown in **Figure 12a**, GCD curve for sulfur reduction typically involves two plateaus indicating two separates reduction steps.[81] The two primary stages could be similarly interpreted by the two discrete peaks on the CV curve in **Figure 12b** from high to low potential along the backward scan.[82] Besides, the rotating-ring disk electrode (RRDE) technique has been used to investigate the kinetics and mechanism of the SRR. Due to different solvation ability of different electrolyte to polysulfides, different reduction waves and $S_3^{\bullet-}$ stabilities were observed in DMSO and DOL/DME, notwithstanding that the reactions observed in RRDE only involves 4-5 electrons out of the 16 electrons from S_8 to Li_2S, and the remained steps are finished through nonelectrochemical chain-growth and disproportionation reactions.[86]

Besides density functional theory (DFT) calculations and electrochemistry, operando and advanced observation techniques have been applied to explore the molecular pathway as well, with a focus on identifying and differentiating various LiPSs and elucidating their cross reactions. Operando high performance liquid chromatography[87,88], UV-vis Spectroscopy[84,87], X-ray Absorption Spectroscopy[83,89], X-ray diffraction[90] are all powerful tools to detect LiPSs intermediates, despite the fact that it is extremely difficult to clearly differentiate each LiPS with a different chain lengths. Thus, each study concluded with its own explainable reaction networks, and on most occasions the LiPSs are simply sorted by high order and low order forms, without further indicating the specific chain length of the intermediates involved in each step.

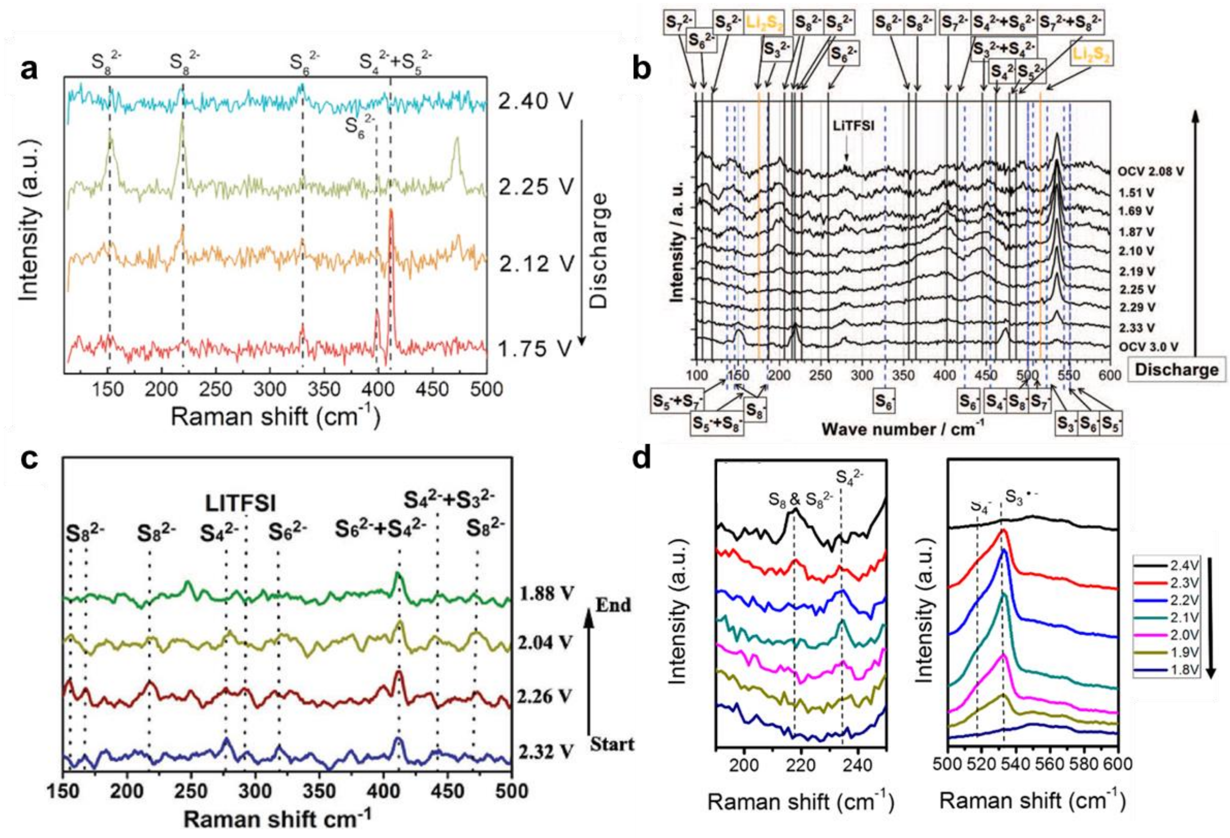

Figure 13. Some *in situ* Raman results in literature. Raman spectra from different studies show different peak assignments and quality of data.[91-94]

Raman spectroscopy is one of the most often used methods to examine the sulfur reaction process because it can distinguish between the signals of various sulfur species. However, the peak assignments are arbitrary and complex, which can be concluded from **Figure 13**.[91-94] It is impossible to obtain a pure LiPS solution or solid crystal due to the instability of LiPSs and their high inclination to disproportionate; consequently, there are no standard samples that can be used to create a standard Raman spectrum library for all the species.[83,87] Although the *in situ* cell used for testing has a long history of development,[95] the testing environment, taking into account varying laboratory instruments and settings in various facilities, could nevertheless have an impact on the results. DFT calculations are able to predict Raman spectrum for each LiPS, but various simulated circumstances yield different outcomes.[93,96] Consequently, each study's peak assignments are distinct, which explains the variety of explanations that have been suggested based on these findings. Meanwhile, because most of the examined LiPSs are dissolved in electrolyte and it is challenging to gather powerful Raman peaks for liquid samples, the quality of the LiPSs' Raman signal is relatively poor. This makes deconvolving and interpreting Raman peaks as well as examining the entire reaction pathway much more challenging. For a fundamental understanding of the mechanism via Raman spectroscopy, higher resolution data and systematical analysis are needed.

1.2.4 Sodium Sulfur Batteries

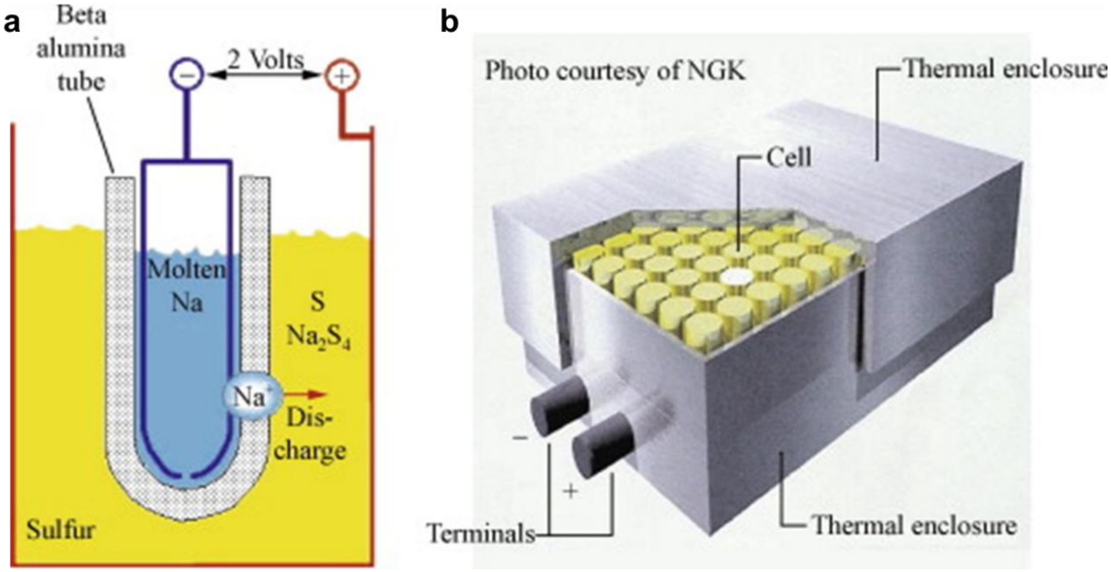

Figure 14. Schematic of high temperature Na-S battery.[97]

Finding a novel anode material is becoming increasingly necessary because of the scarcity of resources and the high price of lithium. Similar to lithium in the same group, sodium has a low potential (-2.71 V versus standard hydrogen electrode) and high capacity (1165 mAh g^{-1}).[98,99] If used in next-generation batteries, sodium's far greater abundance could drastically reduce the cost. As a result, sodium sulfur (Na-S) batteries are becoming a new focus in academic research for high energy density batteries. Na-S batteries are based on the reaction between sodium and sulfur to form sodium sulfide, similar to that in Li-S batteries. It has been realized in stationary energy storage systems under high temperature (>300℃) with a solid electrolyte, “beta alumina”. In this traditional high temperature Na-S battery setup, both sulfur and sodium are molten to liquid in order to accelerate the chemical reaction. However, the reaction between sodium and sulfur can only go to Na_2S_x ($x \geq 3$) even under such critical conditions, resulting in a capacity lower than 557 mAh g^{-1} and energy density at about 110 Wh kg^{-1}.[100] This entire setup is expensive and energy consuming, and raises safety concerns, which has encouraged the development of Na-S batteries that can operate at ambient temperature.

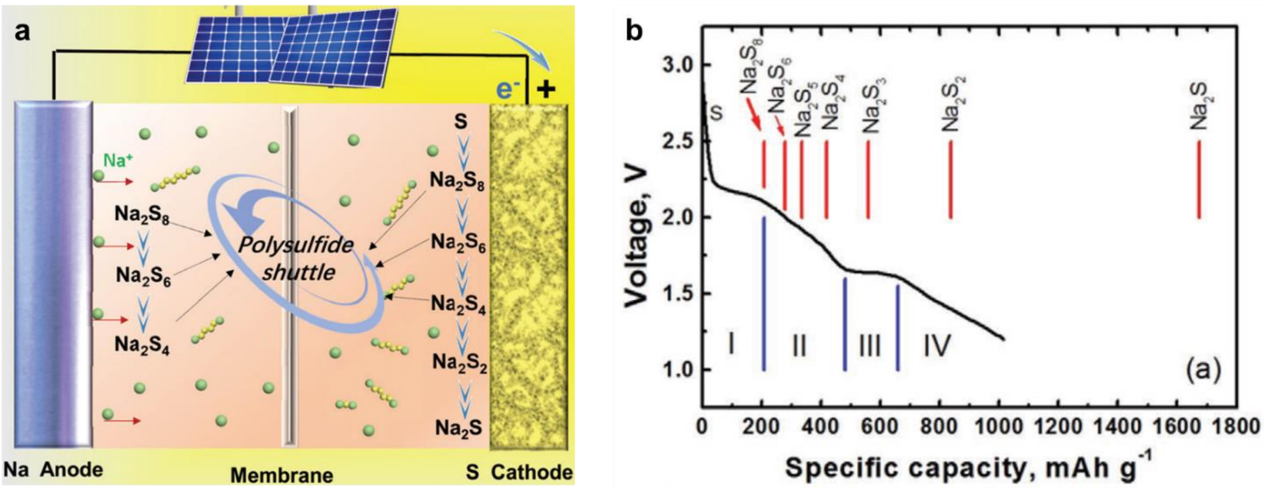

Figure 15. Room temperature Na-S battery. **a,** working principle of room temperature Na-S battery and shuttling problem.[100] **b,** Discharge profile of room temperature Na-S battery. Limited capacity was obtained due to the uncompleted sulfur reduction.[101]

The investigation of Na-S batteries that operate at room temperature is still in its early stages. Solid electrodes are used in the room temperature Na-S battery, which has greater safety, lower toxicity, and higher energy output. The theoretical capacity of Na-S battery is 1672 mAh g^{-1} when sulfur is fully utilized, with a theoretical energy density of 1274 Wh kg^{-1}, which is about three times higher than that of Li-ion batteries (420 Wh kg^{-1}).[102] Most importantly, the abundance and accessibility of both Na and S ensure the low cost, noticing that the price of Na raw material is only 1/25 of that of Li (Na: 23,600 mg kg^{-1} versus Li: 20 mg kg^{-1} in the earth's crust).[102] Nevertheless, similar to Li-S batteries, some practical issues must first be tackled despite these promising beginnings.

Much more severely than their Li-S analogs (80%), the sodium acquisition of sulfur poses a serious volume expansion of up to 171%. The increased size of sodium ions causes slower ion transport and electrochemical kinetics, which in turn slows down the polysulfide conversion and restricts the amount of material that can be used. Since sodium polysulfides are soluble, too, like lithium polysulfides, the problem of shuttling is very serious, especially when the conversion takes a long time. Compared to Li-S cells with an average working voltage at around 2.2 V, Na-S cell functions a mid-point voltage of about 1.7~1.8 V (versus Na/Na^+). Thus, it is more difficult for Na-S battery to achieve a high energy density.[102] Additionally, its development is hindered by the poor conductivity of S and Na_2S as well as the unstable SEI on the Na anode.[100] As a result, there is still much work to be done in the development of Na-S batteries.

In contrast to Li-S batteries, which have widely accepted separator (polypropylene) and electrolyte systems (LiTFSI/DOL/DME), the separator and electrolyte in Na-S batteries are currently being studied. A typical but possibly not the optimum combination is glassy fiber and PC/EC,[100,103-105] which is completely different from what is used in Li-S batteries. This highlights the notable differences between sodium and lithium, explains why switching from lithium to sodium might be challenging. A more systematical fundamental study and a widely accepted construction of Na-S battery is urgently needed. In **Chapter 6**, we will discuss some preliminary results on Na-S study, mostly focusing on the separator design to eliminate the severe shuttling in the cell and improve the cycling stability.

1.3 Holey Graphene Frameworks for Energy Storage Applications

1.3.1 Graphene

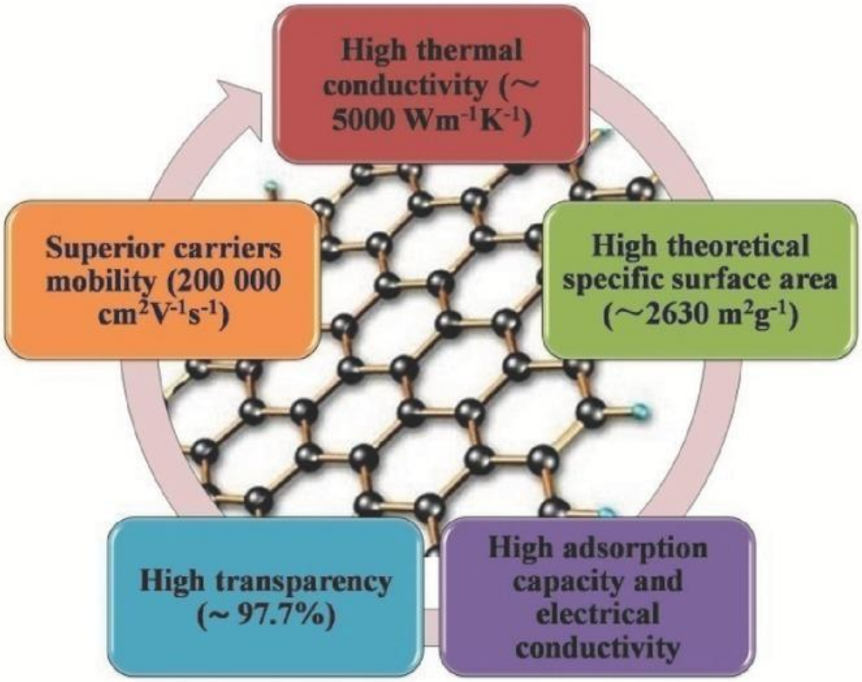

Figure 16. Properties of graphene.[106]

Since its discovery in 2004[107], graphene has gained enormous attention as a star material. Graphene is an atomically thin layer of graphite. Graphite is a ubiquitous material in daily life that can be produced on a massive scale and used in anything from lubricants to pencils. When graphite is exfoliated into a single layer, some intriguing physical and electrical features emerge. Graphene is a layer of sp^2 carbon atoms bonded to three nearby carbons in a benzene ring structure. It is transparent,[108] and has a high mechanical strength with high theoretical specific surface area (2630 $m^2\ g^{-1}$)[109], and its big π bond hovering over the honeycomb plane allows for extraordinary electron and hole mobility of up to 200000 $cm^2\ V^{-1}\ s^{-1}$ [110].

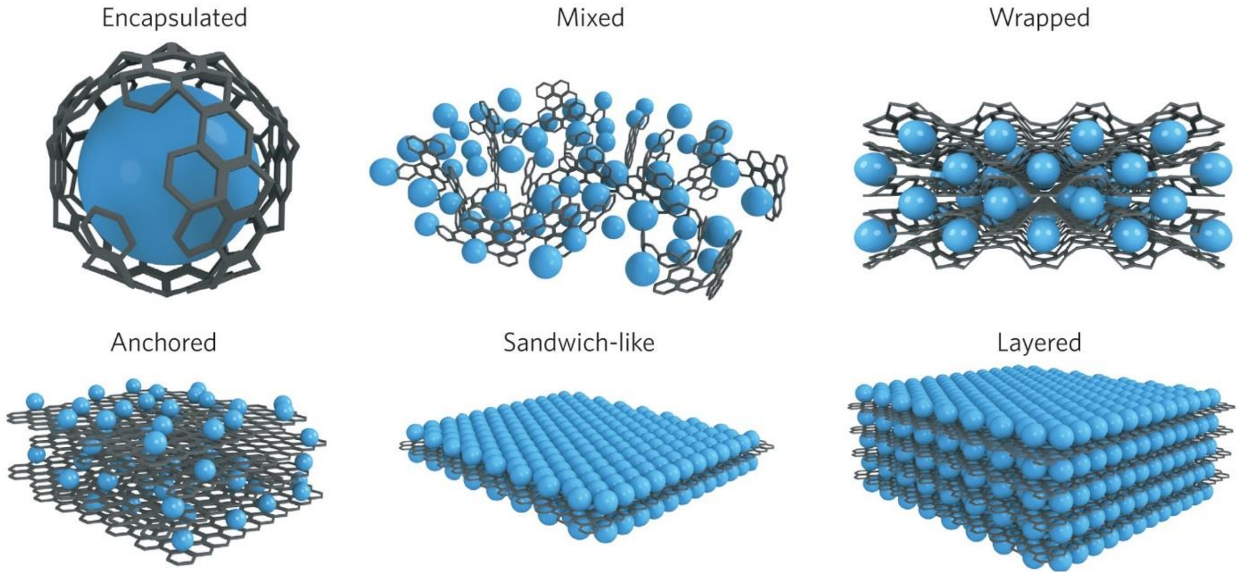

Figure 17. Schematic of graphene composite materials for electrochemical energy storage. Active materials can be encapsulated in graphene cage, mechanically mixed with graphene, wrapped by multiple graphene sheets, anchored onto graphene plane, sandwiched on both sides of graphene, or alternated with graphene layers to form a layer structure.[111]

Graphene plays an important role in next generation batteries. Its high electronic conductivity makes it a useful additive for enhancing the conductivity of the electrode when employed as a host or simply combined with other materials. The flexibility of the 2D sheet is even more intriguing; when the graphene sheets are overlapped on the sheet's edge, they create a highly stretchable network that can regulate and constrain the volume and shape changes of the materials buried beneath it.[44] This is particularly useful for alloy electrodes like silicon, sulfur, and lithium that, when frequently cycled, undergo enormous volume variations. The continuous and robust network can guarantee the electrode integrity and protect against pulverization of the active materials, increasing the utilization of the active materials.[112] Beyond being as an additive, graphene can also serve as a substrate to provide catalytic active sites. Numerous catalytic substances, such as heteroatoms (N, S, P, etc.)[113], oxides[114], sulfides[115], nitrides[116], and even polymers[117], can be accommodated on graphene. These composites excel in performance as electrodes for batteries because they have both rich active centers and good conductivity. **Figure 17** illustrates multiple ways for constructing graphene composites, which opens up a wide range of potential structures that can be used in a variety of circumstances.

1.3.2 Holey Graphene Frameworks

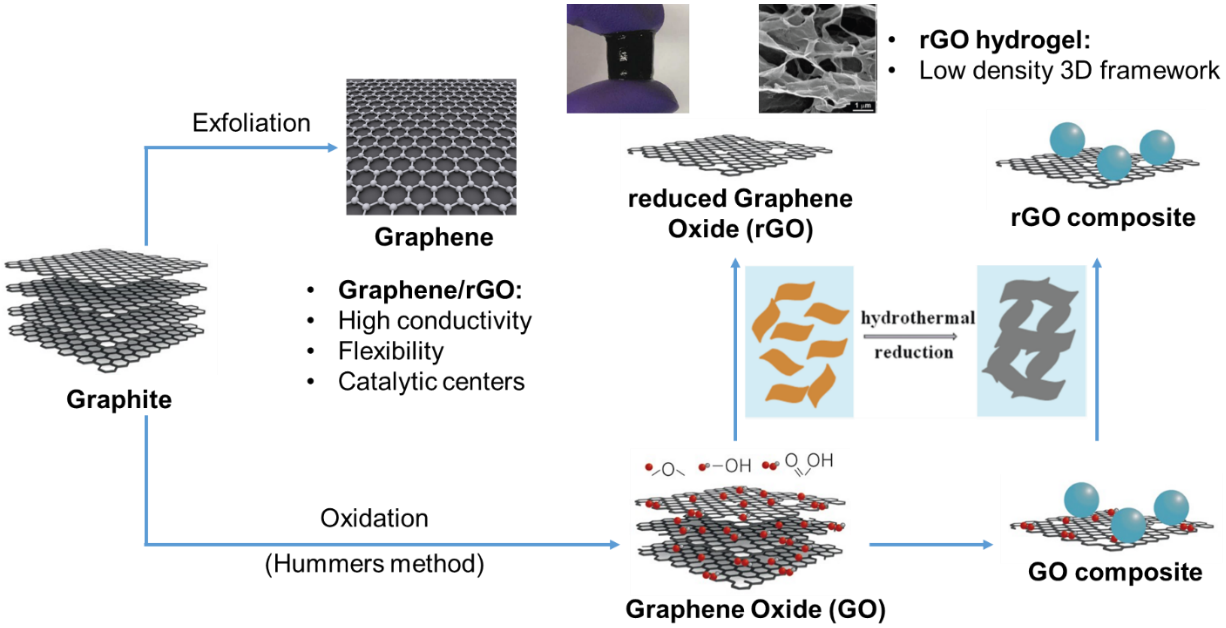

Figure 18. Synthesis and properties of commonly used graphene-based materials (GO, rGO, GO- and rGO-based compounds) for energy storage devices.[111,118,119]

Common approaches to fabricate graphene include mechanical exfoliation[120], liquid phase exfoliation[121], chemical exfoliation[122], chemical vapor deposition[123], and other bottom up approaches[124]. Graphene produced by mechanical exfoliation and chemical vapor deposition has a structure similar to ideal single layer graphite, with a honeycomb lattice made up predominantly pure carbon atoms. As shown in **Figure 18**, another method of producing graphene from graphite is through the synthesis of graphene oxides (GO). Chemical exfoliation such as Hummers' method[121] is used to produce GO, which involves heavily oxidizing the graphite with strong oxidants. GO are highly oxidized graphene sheets with a lot of oxygen-containing functional groups on the graphene plane, like carboxyl -COOH, carbonyl -C=O, hydroxyl -OH, and epoxide -O- groups.[125,126] GO are more polar and easier to manipulate than graphene (pure carbon), enhancing their adaptability in a variety of applications, including batteries. For instance, its negative charge surface because of the oxygen-containing functional groups are good choices for the modification on the separator in Li-S batteries, as the negative charges could intrinsically push the negative polysulfide intermediates back into sulfur cathodes, thus reducing the loss of sulfur in the form of polysulfides.

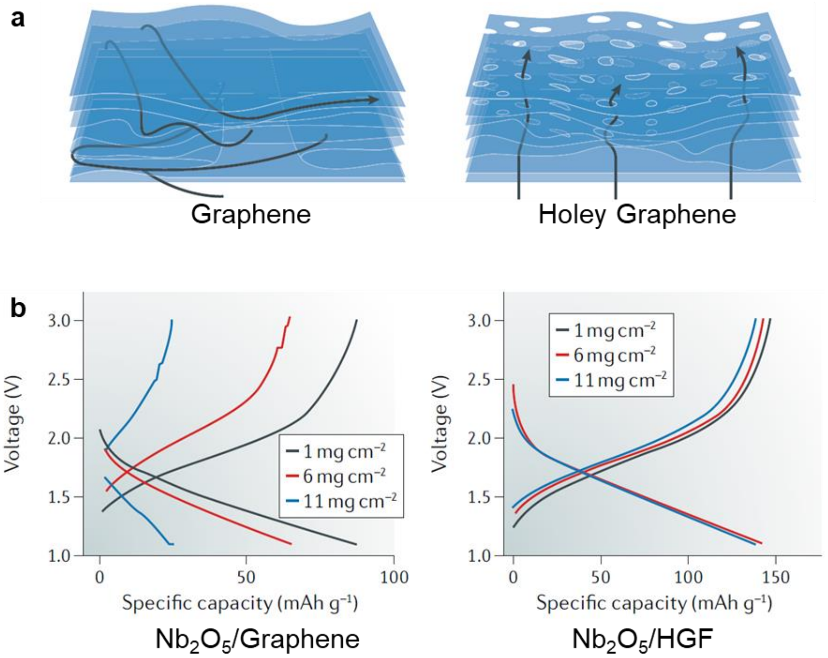

Figure 19. Holey graphene frameworks in energy storage applications. **a,** Graphene versus holey graphene sheets. Holey graphene sheets provide extra ion diffusion pathway thus lead to faster kinetics in electrode reactions.[5,118] **b,** Nb_2O_5/graphene composite versus Nb_2O_5/holey graphene composite. Holey graphene frameworks enable high capacity of Nb_2O_5 electrode even under ultrahigh mass loading.[127]

GO can be further oxidized or reduced. If further oxidized by H_2O_2, holey graphene oxides (HGO) are produced. In addition to the oxygen-containing groups on the edge, nanoholes in the graphene plane will be produced by H_2O_2 etching, which will greatly improve the material's porosity and the ion diffusivity through the sheets.[118] Both GO and HGO could be reduced, resulting in reduced graphene oxides (rGO) and reduced holey graphene oxides (rHGO), respectively. Most of the oxygen groups will be removed during the hydrothermal reduction of GO/HGO in aqueous solution, which will reduce their hydrophilicity. The resulting hydrophobic sheets will then automatically assemble into a hydrogel in aqueous solution.[128] Freeze dry, a low temperature dehydration process which involves freezing followed by drying under vacuum, is a common way for drying rGO/rHGO hydrogels. The highly porous structure can be preserved during the sublimation of ice because of the absence of capillary action.[129] Freeze-dried rHGO hydrogels, also known as holey graphene frameworks (HGFs), are fascinating supports for high-rate battery electrode applications. In contrast to non-holey graphene frameworks (GFs), the nanopores in holey graphene sheets are big enough to serve as ion diffusion bypasses between different layers of graphene, dramatically accelerating ion transport over the entire film and enabling ion access to the full surface area (**Figure 19a and b**). HGFs can attain large volumetric capacitance while maintaining high gravimetric capacitance and excellent rate capabilities, thus are extremely beneficial for high rate/high mass loading applications including fast charging batteries, thick electrodes, and supercapacitors.[127,130] **Figure 19c and d** compares two Nb_2O_5 electrode loaded onto GF and HGF, respectively. HGF could continue to support high capacity when mass loading is increased to 11 mg cm^{-2}, whereas GF electrode displays a dramatic capacity drop as mass loading is increased.[127]

In **Chapter 2-4**, N,S dual-doped HGF was chosen as a modeling system for sulfur host as it shows a high performance in Li-S batteries.[70,131] As was already noted, N,S-HGF has three benefits that render it a suitable system for sulfur cathodes, including flexible structure for sulfur volume adjustment, quick ion diffusion for high sulfur loading, and multiple active sites for modification and catalysis. **Figure 20a** depicts the synthesis procedure of N,S-HGF. In a manner similar to that of HGF, N,S-HGF can also be produced from GO. NH_4SCN and H_2O_2 are added as N,S doping sources and etching reagent, respectively. After hydrothermal reduction for 6 hours at 180 °C, 3D N,S-HGF was formed in aqueous solution. **Figure 20b** displays a macroscale photo of N,S-HGF. From the scanning electron microscopy (SEM) image in **Figure 20c**, we can observe the highly porous hierarchical structure inside N,S-HGF. For a higher resolution on the structure characterization, transmission electron microscope (TEM) can be used to verify the nanoholes on the holey graphene sheets in HGFs (**Figure 20d**). The enlarged annular dark-field scanning transmission electron microscopy (ADF-STEM) image in **Figure 20e** allows us to observe the sulfur dopant and bond structure at the atomic level. All of these morphology characterizations clarify the highly porous 3D structure and successful doping on graphene frameworks.

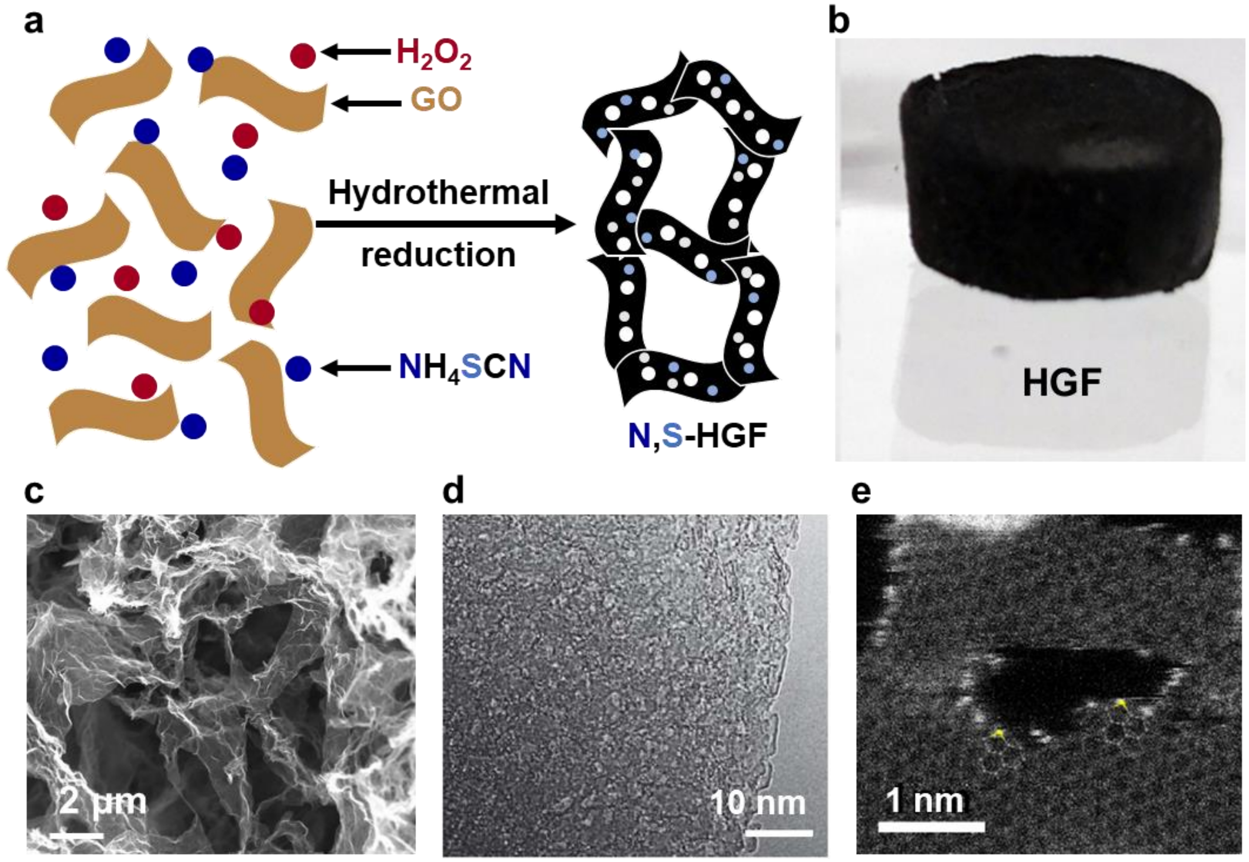

Figure 20. Heteroatom-doped holey graphene frameworks. **a,** Schematic showing the hydrothermal reduction synthesis route of N,S dual-doped holey graphene frameworks. GO solution was mixed with NH_4SCN as doping sources and H_2O_2 as etching reagent. After hydrothermal reduction for 6 hours at 180 °C, 3D N,S-HGF was formed in aqueous solution. **b,** A photograph of freestanding HGF. **c,** A scanning electron microscopy (SEM) image of the N,S-HGF showing the hierarchical porous structure. **d,** A transmission electron microscopy (TEM) image showing the nanoholes on the holey graphene sheets in HGFs. **e,** An enlarged annular dark-field scanning transmission electron microscopy (ADF-STEM) image of N,S-graphene nanosheets. Sulfur dopant was represented by the bright dots on the graphene surface, indicating a bond structure in thiophene-type (C-S-C).[70,118]

Experimental studies also confirms the high performance of N,S-HGF in Li-S coin cells.[70] The ability of N,S-HGF to speed up the polysulfide conversion, particularly at the rate-determining phase, was confirmed by activation energy measurements using temperature-dependent EIS tests at different voltages. **Figure 21a** presents the activation energy profiles for the four distinct catalyst-based cathodes at varying voltages. Generally, the activation energies for doped HGFs exhibits a stepwise profile resembling that of the standard KCB/S composite cathode (see **Figure 11a**), i.e., relatively low values at the initial reduction stage (2.7-2.5 V), which rise at the median reduction stage (2.4-2.0 V), and reach its maximum at the final reduction stage (1.9-1.7 V). This further supports the idea that the final conversion steps into insoluble Li_2S_2/Li_2S. The activation energies are significantly lowered with the addition of heteroatom dopants, particularly for the last step. For instance, the maximum activation energy for the ultimate conversion from soluble LiPSs into insoluble Li_2S_2/Li_2S falls from >0.32 eV in HGF to 0.12 eV in N,S-HGF. What's more, among the four distinct samples, N,S-HGF had the smallest polarization voltage gap (152 mV) between anodic and cathodic sweeps at the current density of 0.2 C, as shown in **Figure 21b**. Normally, a higher current density would result in more severe polarization and wider voltage gaps, however for N,S-HGF, the increase in voltage gap from 0.05 C to 2 C is only 130 mV, which is significantly less than that of non-doped HGF catalysts (541 mV) (**Figure 21c**). When compared to pristine HGF for rate capability, the N,S-HGF electrodes exhibit outstanding specific capacities at all C-rates, notably at high rates (**Figure 21d**). Furthermore, N,S-HGF electrodes display a significantly improved cycling stability, signified by an extremely low capacity decay of 0.025% per cycle at 1 C for 500 cycles, compared with that of 0.162% per cycle for HGF (**Figure 21e**). Such comparisons firmly demonstrate the significantly better performance brought on by the improved SRR catalytic activity of N,S-HGF.[70]

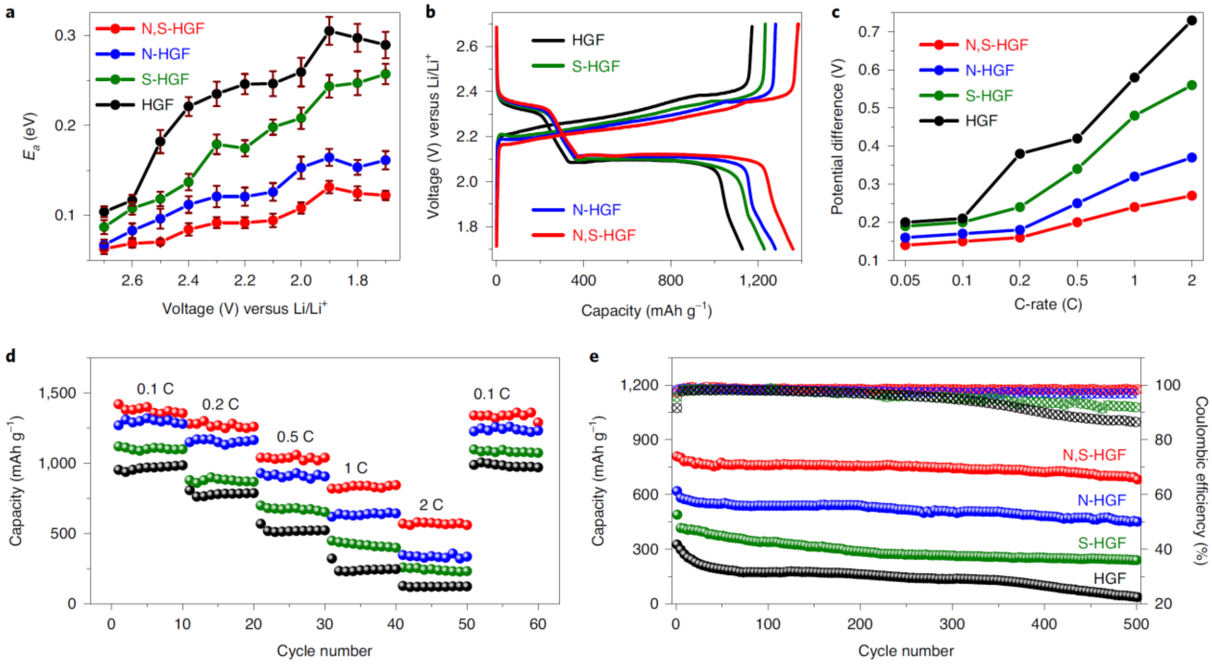

Figure 21. Performance of the heteroatom-doped HGF cathodes in Li-S coin cells. **a,** Activation energy profiles for different heteroatom-doped HGFs. Activation energies were plotted versus voltage. **b,** GCD profiles of sulfur cathodes with different heteroatom-doped HGFs at 0.1 C. **c,** Polarization voltage gaps at different C-rates in different heteroatom-doped HGFs. **d,** Rate capability tests of sulfur cathodes with different heteroatom-doped HGFs with 4 mg cm^{-2} sulfur loaded. **e,** Cycling stability tests of sulfur cathodes with different heteroatom-doped HGFs at 1 C with 4 mg cm^{-2} sulfur loaded.[70]

In addition, in **Chapter 5**, another porous carbon doped with nitrogen was chosen to investigate the atomic level catalytic ability for the SRR. In **Chapter 6**, N,S-HGF and HGO were both fabricated onto separators to reduce polysulfide shuttling in Na-S batteries. The N,S-HGF was expected to have both physically blocking and catalytic effects on shuttled polysulfides.

CHAPTER 2: PASSIVATION AND SHUTTLING MECHANISM STUDY BY CYCLIC VOLTAMMETRY IN LITHIUM SULFUR BATTERIES

2.1 Introduction

Lithium sulfur (Li-S) battery has attracted considerable interests for next generation energy storage systems based on its exceptional theoretical capacity of 1672 mAh g^{-1} and promise for ultrahigh energy density of 2600 Wh kg^{-1} [25,34]. Despite the fact that all kinds of designs have been considered for the electrode/separator/electrolyte to solve the problems in Li-S batteries such as the notorious shuttling problem as mentioned in **Chapter 1**, the fundamental reaction mechanism still maintains vague and intricate. The exploration of the mechanism in a battery not only includes the complex molecular pathway which will be thoroughly investigated in **Chapter 3** and **Chapter 4**, but also extends to the active material deposition behavior on electrode. Both aspects will offer interesting thoughts on the future design of batteries to further improve the battery performance. For instance, a close examination of the cell's shuttling behavior can be used to identify the shuttling mechanism and develop logical designs for various components to fend off active sulfur loss.

The term "solid electrolyte interphase (SEI)" describes an interfacial layer that forms on the battery electrodes as a result of the electrolyte's fragmentation during cycling. A perfect SEI should permit lithium ion conduction but prohibit electron pass-through, to protect the electrode from further reacting with the electrolyte and consuming extra active materials.[132] Conjointly, the creation of a more robust SEI on the lithium anode could be aided further by adding effective additives to the electrolyte. $LiNO_3$ is a common electrolyte additive in Li-S batteries.[133-135] It assists in the formation of a more stable SEI on the lithium anode, improving the performance of Li-S batteries.[136-138] Nevertheless, it has been discovered that $LiNO_3$ has a deleterious impact on the sulfur cathode, the other side of the Li-S battery. $LiNO_3$ exhibits an additional peak on CV under 1.7 V in the earlier findings, which is believed to be an irreversible reaction that distorts galvanostatic curves and negatively impacts the capacity and stability of Li-S batteries.[74] According to an electrochemical quartz crystal microbalance (EQCM) investigation, the electrode mass and resistance are larger in the low voltage regime, indicating that a passivation layer has formed and that some of it is actually able to dissolve and reform.[139] Density functional theory (DFT) studies suggest that $LiNO_3$ has the potential to deform the galvanostatic voltammetry curves by altering the kinetics of the last reduction step during discharge.[140] In light of this, $LiNO_3$ is thought to have a dual-edged impact on lithium-sulfur batteries, affecting both the anode and cathode. The performance of Li-S batteries will be significantly impacted by the voltage window used during electrochemical experiments because of the passivation layer on the sulfur cathode created at low voltages.[141] This study focuses on how changing the voltage window affects the performance of lithium-sulfur batteries by affecting the passivation layer created by $LiNO_3$, differentiating the roles played by $LiNO_3$ and Li_2S in the formation of passivation layers in the low voltage region, and attempting to find a window that strikes a balance between the benefits and drawbacks of $LiNO_3$.

Cyclic voltammetry (CV) is an electrochemical method that records current along with controlled voltage changes and can be used to investigate the electrochemistry taking place in the system being monitored.[82] The reaction steps that occur during the voltage scan are represented by peaks in the curve, thereby CV offers a simple way to visualize the voltage required for the reaction to occur. Moreover, the area integrated based on the CV curve provides the information on the amount of charge delivered during the reaction, which could assist us in determining the charge transfer number for each stage of the reaction.

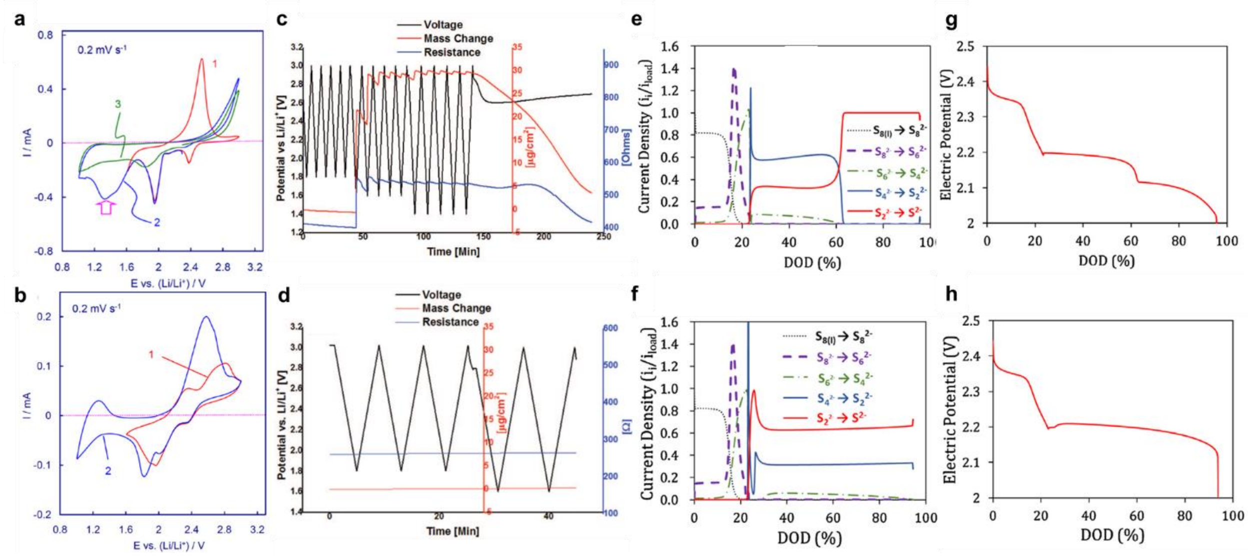

Figure 22. Studies on $LiNO_3$ effect in Li-S batteries. **a, b,** CV of Li-S coin cell with Li_2S_9 on carbon electrode as cathode, with (**a**) or without (**b**) $LiNO_3$, recorded with a scan rate of 0.2 mV s^{-1} in a voltage window of 1.6-3.0 V (curve 1) and 1.0-3.0 V (curve 2 and curve 3).[74] **c, d,** EQCM results of sulfur cathode cycled on gold electrodes on quartz crystals in a voltage window of 1.6-2.5 V, with (**c**) or without (**d**) $LiNO_3$.[139] **e, f, g, h,** Numerical simulation on exchange current densities of each step and galvanostatic charge discharge profiles of the whole cell, for sulfur reduction reaction in Li-S batteries, with (**e, g**) or without (**f, h**) $LiNO_3$.[140]

In this study, we first illustrated how the charge calculation approach based on CV may be used to probe mechanisms. Then, utilizing CV to study the passivation layer behavior and its impact on performance under various voltage windows with a small loading of active sulfur, we were able to better understand potential side reactions in Li-S batteries that could affect the charge calculation on CV. It was discovered that the creation of the passivation layer would have a substantial impact on the charge calculation during the first few cycles and would limit the capacity by either reacting with lithium polysulfides (LiPSs) or blocking the active sites for the sulfur reaction. Next, we loaded higher amount of sulfur and gradually widened the voltage window in order to scrutinize the shuttling mechanism. We identified a particular CV feature associated with the shuttling process using peak deconvolution and charge analysis, which can be utilized to evaluate the shuttling level in Li-S batteries.

2.2 Experimental

2.2.1 Synthesis of Graphene Oxide and Heteroatom-Doped Holey Graphene Frameworks

Graphene oxide was prepared according to a modified Hummers' method[128]. Briefly, 6 g natural graphite (325 mesh, Sigma-Aldrich) was added into 140 ml concentrated sulfuric acid under vigorous stirring in an ice-water bath, followed by slowly adding 3 g sodium nitrate (Sigma-Aldrich) and 18 g potassium permanganate (Sigma-Aldrich). Due to the strong acidity of sulfuric acid and highly oxidative nature of the sodium nitrate and potassium permanganate, it is necessary to keep the temperature near 0 °C to avoid too fast oxidation of the graphite that may cause safety concerns. After stirring for 30 min, the reaction system was transferred into a water bath at ~50 °C, under continued stirring till the mixture forming a thick paste. The system was next transferred back to the ice-water bath, followed by drop-wise addition of ~1 liter of iced deionized water. The mixture was then centrifuged and washed by 1:10 HCl aqueous solution for three times followed by repeated washing with deionized water. The final solution was dialyzed for one week to remove the extra H^+ ions absorbed on the graphene oxide surfaces.

Heteroatom-doped HGFs were synthesized by reacting the dopant sources and H_2O_2 with the graphene oxide (GO) aqueous dispersion through a typical hydrothermal method. N,S-HGF was synthesized by mixing 30 ml of 2 mg ml^{-1} GO aqueous dispersion solution, 45 μl of 30% H_2O_2 aqueous solution and 3.0 g NH_4SCN, followed by sonication and hydrothermal reaction at 180 °C for 6 h in an autoclave. Free-standing N,S-HGF hydrogel can be obtained. The hydrogel was then freeze-dried and annealed at 900 °C for 1 h to obtain the N,S-HGF aerogel.

2.2.2 Electrochemical Measurements

The electrolyte (with $LiNO_3$, also denoted as blank electrolyte) was made of 1 M lithium bis(trifluoromethanesulfonyl) imide (LiTFSI) (Sigma-Aldrich) and 0.2 M lithium nitrate (Sigma-

Aldrich) in the mixed dimethoxyethane (DME) (Sigma-Aldrich) and 1,3-dioxolane (DOL) (Sigma-Aldrich) solution (1:1 by volume). The electrolyte (without $LiNO_3$) was prepared in the same way without adding $LiNO_3$. The Li_2S_6 catholyte was prepared by reacting the sublimed sulfur (Sigma-Aldrich) with Li_2S (Sigma-Aldrich) in stoichiometric proportion in the blank electrolyte. The mixture was vigorously stirred at 50 °C in an argon-filled glove box overnight to produce a brownish-red Li_2S_6 catholyte solution.

The electrochemical performance of the catalyst was conducted in the CR2032 coin cells assembled in an argon-filled glovebox. The N,S-HGF electrode was prepared by directly pressing the aerogel into a freestanding thin film. Afterwards, the catholyte (Li_2S_6 in the blank electrolyte) was directly used as sulfur source to drop cast in the catalyst electrode. In our experiment, the mass loading of the sulfur in the cathodes was set in the range of 0.16 mg cm^{-2} to 1 mg cm^{-2}. The sulfur cathodes were then directly assembled into a CR2032 coin cell with lithium foil, Celgard 2500 separator and blank electrolyte. CV curves were recorded in different voltage ranges at a scanning rate of 0.05 mV s^{-1}.

2.3 Results and Discussion

2.3.1 Charge Number Calculation Based on Cyclic Voltammetry Results

We choose a specific heteroatom-doped N,S-HGF as model system for all the mechanism study considering its superior sulfur reduction reaction (SRR) kinetics, considerably low activation energy, and excellent performance in Li-S batteries[70]. It has been demonstrated in **Chapter 1** that N,S-HGF provides favorable catalytic centers that promote the rapid conversion of the LiPSs to mitigate shuttling effect[70]. The continuous sp^2 bonded carbon basal plane provides highly conductive scaffold with tunable catalytic centers. A typical hydrothermal process was used to construct the 3D HGF structure with interconnected micro and nanopores. Taking advantage of the porous structure and good adsorption for polysulfide solutions, catholyte with Li_2S_6 dissolved in LiTFSI/DOL/DME was used as the source of sulfur for N,S-HGF in this work. The amount of sulfur loading was controlled by adding different amounts of catholyte during cell assembly.

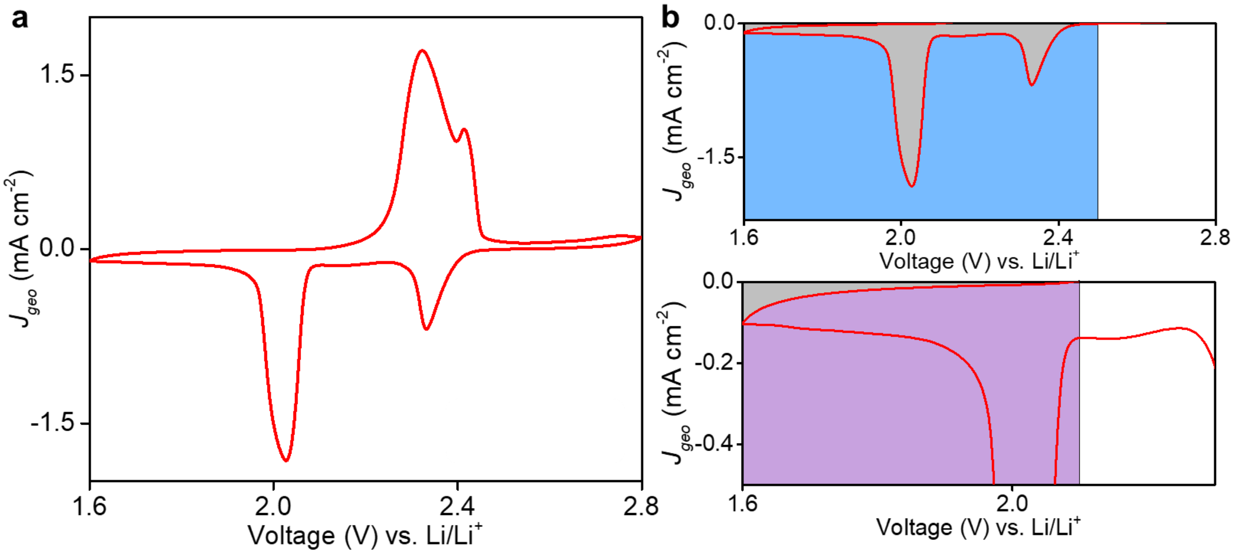

Figure 23. Charge number calculation based on CV for N,S-HGF. **a,** A typical CV curve for sulfur reactions in Li-S battery. **b,** Integration of CV for discharge process. Gray area represents the integrated area.

CV is a powerful tool for analyzing electrochemistry process. To better understand the charge transfer process in the SRR, we performed CV measurements, followed by quantitative charge analysis via integrating the peak area. The charge number transferred (Q) for the electrochemical steps can be calculated from CV curves. Q is calculated by integrating the area enclosed in CV[142,143]:

$$Q = \int_{t_1}^{t_2} i(t)dt = \frac{1}{v}\int_{V_1}^{V_2} i(V)dV = \frac{A}{v}\int_{V_1}^{V_2} j(V)dV = \frac{AS}{v}$$

$$dt = \frac{dV}{v}$$

Equation 4

Q: Charge (C)

i: Current intensity (A)

j: Current density (A cm^{-2})

A: Geometric area of the electrode (cm^2)

v: Scan rate (V s^{-1})

t: Time (s)

S: Integrated area

Figure 23a is a typical CV curve for sulfur oxidation and reduction reactions in Li-S batteries. In order to ensure all the current was attributed to a reasonable stage of reaction, for all the CV charge calculation in this work, all the negative current was considered as reducing current, including both the current below zero during discharge **(Figure 23b, top panel)** and the negative current **(Figure 23b, bottom panel)** during the initial stage of charge. Similarly, the oxidizing current includes the initial stage of the reduction scan as well.

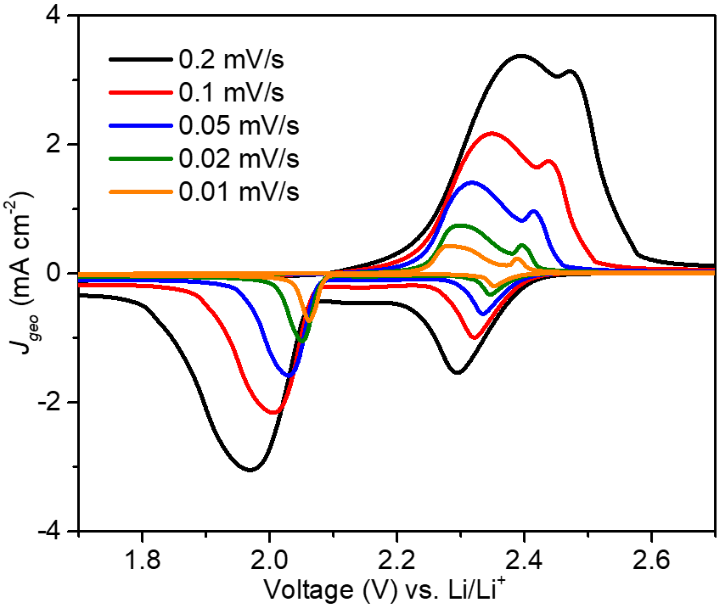

Figure 24. CV plots of sulfur reactions with multiple different scan rates.

Analyzing CV results requires consideration of a number of variables, including voltage window and scan rate. **Figure 24** illustrates how a slower scan rate results in a greater peak separation, hence a slower scan rate is preferable for this study, bearing in mind that we hope to analyze the mechanism using the separated peaks. For the following studies, we selected 0.05 mV s^{-1} as our scan rate because the peaks are reasonably spaced apart and the overall time required with this sweeping rate won't be excessive. To rule out any influence from sources other than sulfur in the cell, we exhaustively examined the CV features of sulfur reactions before moving on to detailed peak analysis and reaction network construction in **Chapter 3**. This aids in giving us a more fundamental understanding of how electrolyte and active materials are reacted and deposited on electrodes.

2.3.2 $LiNO_3$ and Li_2S Passivation Study by Cyclic Voltammetry with Different Voltage Windows

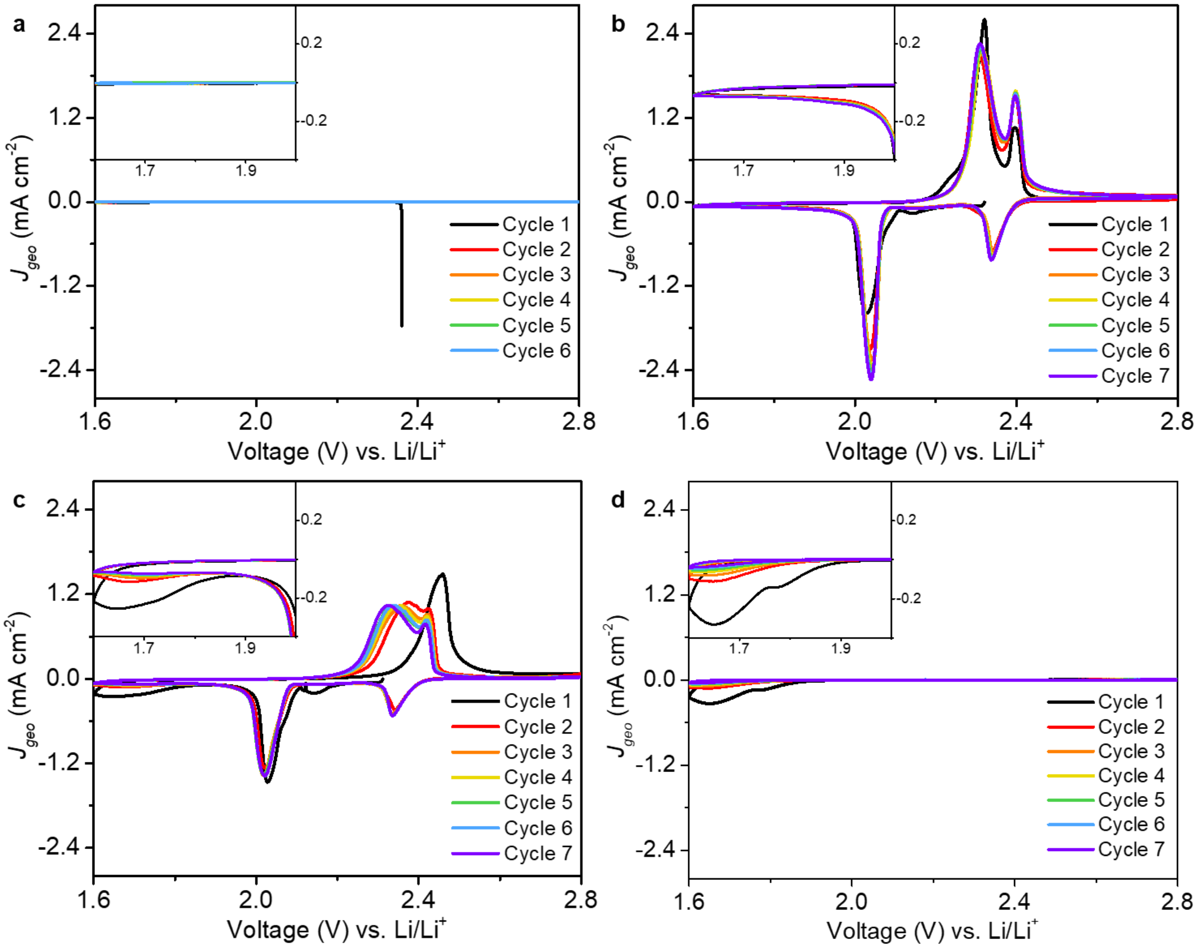

Figure 25. CV plots of four coin cells with different electrolyte composition to investigate the reaction of $LiNO_3$. Comparison were done between four cells, which are the blank cell without $LiNO_3$ (**a,** cell 1), sulfur loaded cell without $LiNO_3$ (**b,** cell 2), sulfur loaded cell with $LiNO_3$ (**c,** cell 3), and blank cell with $LiNO_3$ (**d,** cell 4).

Provided that $LiNO_3$ is a typical additive for Li-S batteries and that it has been noted to undergo some decomposition at low voltage, we first tested the CV of a Li-S cell using N,S-HGF as the cathode with an electrolyte that contained or did not contain $LiNO_3$, in order to look into the reaction of $LiNO_3$ and determine its impact on charge calculations when integrating the CV area to study mechanism. **Figure 25** compares four cells: a blank cell without $LiNO_3$ (cell 1), a sulfur loaded cell without $LiNO_3$ (cell 2), a sulfur loaded cell with $LiNO_3$ (cell 3), and a blank cell with $LiNO_3$ (cell 4). Cell 3 is a typical Li-S cell, with sulfur as active material and $LiNO_3$ as additive. Cell 1 serves as a control cell, whose current is solely from the double layer capacitance brought by the blank electrolyte (1 M LiTFSI in 1:1 v:v DOL/DME) which is negligible in comparison to the reactions of sulfur and $LiNO_3$ if comparing cell 1 with other cells. Comparing cells 1 and 4, $LiNO_3$ exhibits a reaction that begins at roughly 1.9 V and peaks at roughly 1.65 V, hence the continuously vanishing peak at 1.6-1.8 V in cell 3 is due to the reaction of $LiNO_3$. Cell 2 further confirms the $LiNO_3$ reaction below 1.8 V when compared to cell 3. It is noticeable that cell 2's current density tail below 1.9 V does not return to cell 1's level at the same voltage regime, indicating the generation of Li_2S in this low voltage regime. Therefore, all of the CV curve's area below zero current density, even below 1.9 V (after the end of the second peak), must be taken into account when calculating the charge for the sulfur reaction. According to **Figure 26,** the capacity provided by $LiNO_3$ rapidly decreases to an insignificant level after 10 cycles, hence a cycle after the first 10 cycles was chosen for **Chapter 3-4**'s mechanism charge computation in order to avoid the reaction caused by $LiNO_3$.

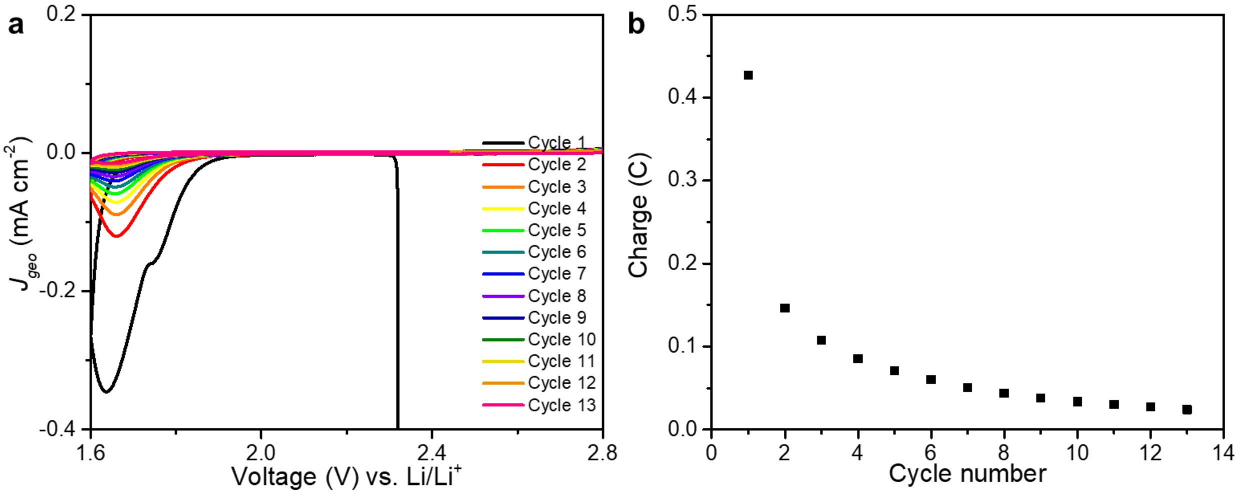

Figure 26. Capacity contributed by $LiNO_3$ reaction. **a,** The first 13 cycles of CV plots for cell 4. **b,** Charge calculation results for each cycle of $LiNO_3$ reaction.

Interestingly, the $LiNO_3$ decomposition in cell 3 differs slightly from that in cell 4, indicating that $LiNO_3$ may decompose differently depending on whether LiPSs are present or not, implying that LiPSs may participate in the $LiNO_3$ decomposition reaction. In order to specify how $LiNO_3$ decomposition passivates the electrode and consumes LiPSs, cells are assembled and cycled in different voltage windows with low sulfur loadings to focus on the passivation behavior.

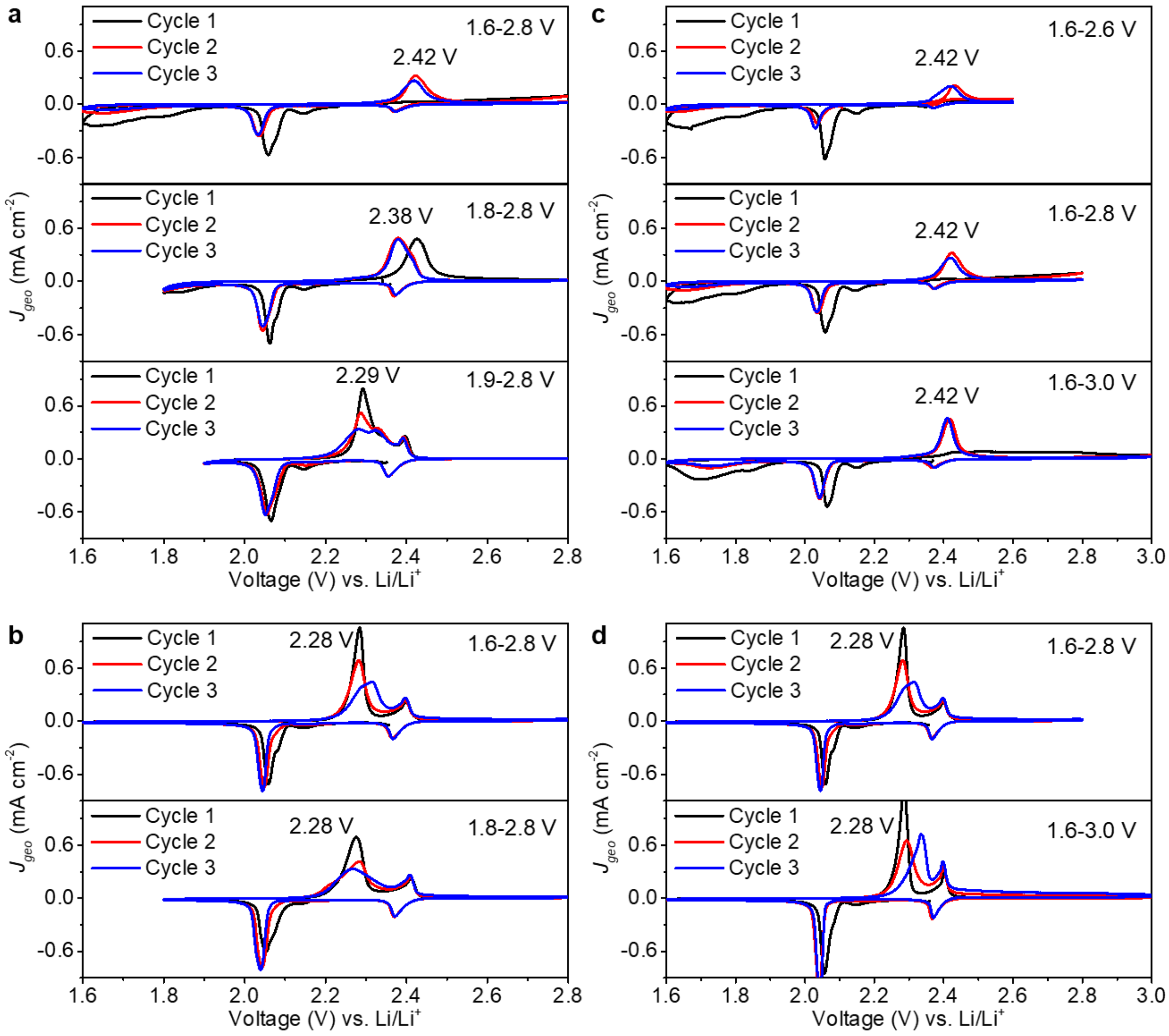

Figure 27. Li-S cells cycled in different voltage windows with low sulfur loadings. **a,** Cells with $LiNO_3$ additive cycled in voltages windows with different lower cutoff voltages, from top to bottom listing cell 5 (1.6-2.8 V), cell 6 (1.8-2.8 V), and cell 7 (1.9-2.8 V). **b,** Cells without $LiNO_3$ additive cycled in voltages windows with different lower cutoff voltages, from top to bottom listing cell 8 (1.6-2.8 V) and cell 9 (1.8-2.8 V). **c,** Cells with $LiNO_3$ additive cycled in voltages windows with different higher cutoff voltages, from top to bottom listing cell 10 (1.6-2.6 V), cell 11 (1.6-2.8 V), cell 12 (1.6-3.0 V). **d,** Cells without $LiNO_3$ additive cycled in voltages windows with different higher cutoff voltages, from top to bottom listing cell 13 (1.6-2.8 V) and cell 14 (1.6-3.0 V).

Figure 27 a and b shows CV curves of cells with or without $LiNO_3$ in voltage windows with different lower cutoff voltages. It is apparent from a comparison of cells 5, 6, and 7 that a lower cutoff voltage results in slower kinetics, as evidenced by the delayed oxidation peak positions, and a comparatively low capacity, as indicated by the relatively smaller reduction peaks following the first cycle and also smaller oxidation peaks. The slower kinetics are due to the creation of a thicker passivation layer on the catalyst active sites in the cathode, which is brought on by the breakdown of $LiNO_3$ and LiPSs. Meanwhile, the capacity has significantly decreased as a result of more active sulfur being consumed or deactivated by encapsulation. Cells 8 and 9 have comparable capacities and oxidation peak behavior, however in cell 8, the peak appears to delay in cycle 3, indicating that the Li_2S generated weakly passivates the electrode at low voltage. When compared to passivation by $LiNO_3$ in cells 5, 6, and 7, the effect of Li_2S in cells 8 and 9 is not readily apparent. This is likely due to the tiny sulfur loading, which results in minimal Li_2S production and minimal performance impact. It is noticed that cell 7 has nearly the same oxidation pattern as cells 8 and 9, with early and separated oxidation peaks. This is explicable by the 1.9 V cutoff voltage, at which $LiNO_3$ breakdown has not yet begun.

Similarly, CV curves of cells with or without $LiNO_3$ in voltage windows with different upper cutoff voltages are shown **Figure 27 c and d**. We discovered that charging to a higher potential has little effect on the position of the oxidation peak, regardless of whether $LiNO_3$ is present (Cells 10, 11, and 12) or not (Cells 13 and 14). This suggests that the upper cutoff voltage has almost no effect on the passivation layer that affects kinetics. However, comparing the regions of the oxidation or reduction peak areas, it is clear that a higher cutoff voltage boosts the capacity. Since the unchanged oxidation peak positions can rule out the possibility of partially dissolving the passivation layer to re-expose the encapsulated sulfur, this higher capacity may be the result of more thorough sulfur oxidation in the first cycle. As can be seen from the graph, the oxidation peak for the first cycle has been severely flattened and requires a high voltage to finish the oxidation. Comparing cell 10, 11, 12 versus 13, 14, distinct peak delays for oxidation peaks in cells 10, 11, and 12 again support $LiNO_3$'s potential to act as a passivator.

Since all these cells are cycled within a fixed voltage window and only the first few cycles are examined, the conclusion shows how the passivation layer is impacted by various voltage windows while the layer is still being built up. Following that, we assembled some cells with a higher sulfur loading to increase the $S/LiNO_3$ ratio, and cycled them in different voltage windows after they have finished their first 10 cycles, to better observe the sulfur reactions and differentiate how Li_2S passivates the cathode. We were able to assess how the passivation layer are affected once it has been produced and stabilized by first starting at a large voltage window and then gradually narrowing the window.

After the first 10 cycles, the passivation layer produced by $LiNO_3$ is stable and both reduction and oxidation show two primary peaks. Two oxidation peaks overlap and two reduction peaks are separated, indicating that the generation and activation of Li_2S is the rate-determining step in both reduction and oxidation. The second reduction peak is separated from the first peak by the delayed formation of Li_2S, and the first oxidation peak is overlapped by the second peak by the delayed initiation of oxidation from Li_2S.

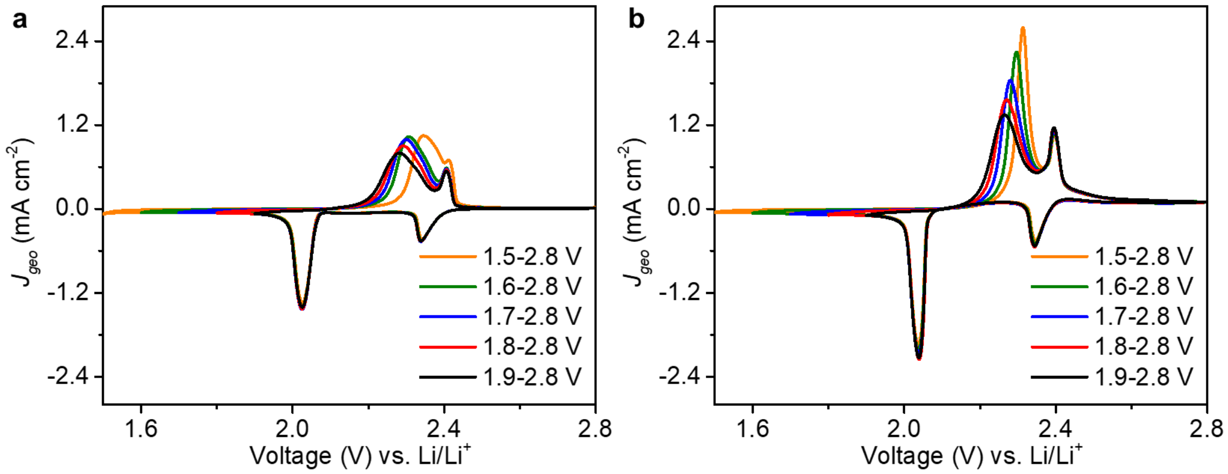

Figure 28. Li-S cells with high sulfur loadings, cycled within voltage windows with various lower cutoff voltages, after completing their first 10 cycles. **a,** Cell 15, with $LiNO_3$. **b,** Cell 16, without $LiNO_3$.

The cells with (cell 15) and without (cell 16) $LiNO_3$ exhibit a similar trend when the window is reduced by altering the lower cutoff voltage, as shown in **Figure 28**. This shows the impact of the voltage window on the oxidation kinetics and Li_2S deposition. The first oxidation peak appears earlier for both cells when the window is shrunk by raising the lower cutoff voltage, showing that Li_2S formation/deformation occurs every cycle and that Li_2S formed from the previous cycle won't prevent oxidation from occurring in the subsequent cycle if it is fully oxidized. The difference is that cell 15 changes slightly less when the lower cutoff voltage is changed, indicating that $LiNO_3$ decomposition is primarily responsible for maintaining the passivation layer in the cell.

It is interesting to note that only the first oxidation peak is affected by the passivation (**Figure 29**), which may be explained by the inertia of Li_2S and the reactivity of LiPSs. Since LiPSs are dissolved in solution, the second step from LiPSs to S_8 becomes quite likely to occur and is not affected by the passivation layer. Some reactions occurring at 1.5 V can significantly slow down the initial oxidation peak kinetics due to the presence of $LiNO_3$ (**Figure 29 a**), necessitating further research to determine the source of the reaction.

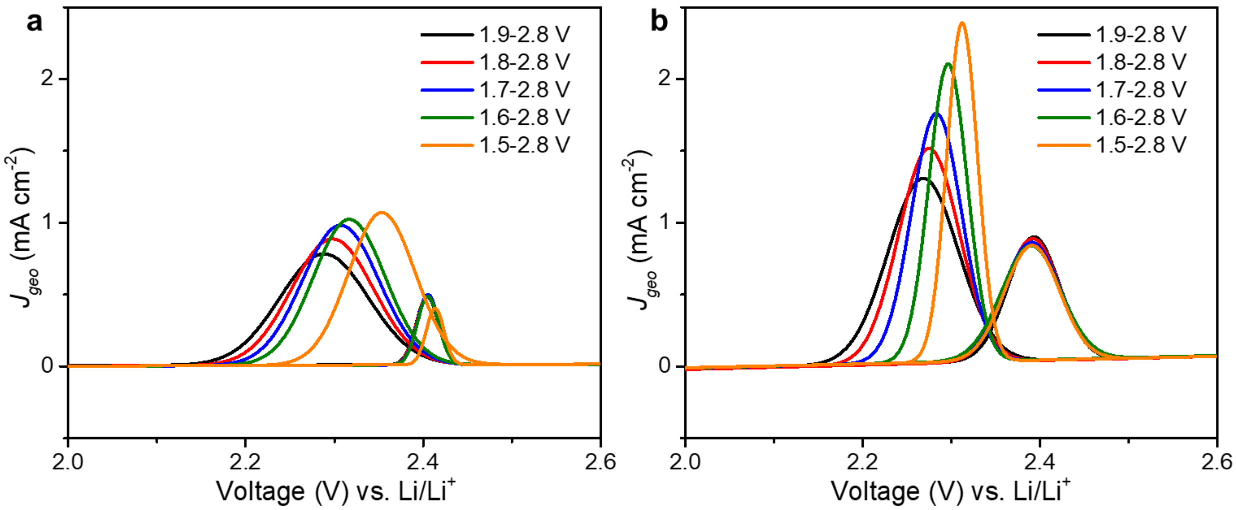

Figure 29. Peaks deconvolved in Li-S cells with high sulfur loadings, cycled within voltage windows with various lower cutoff voltages, after completing their first 10 cycles. **a,** Cell 15, with $LiNO_3$. **b,** Cell 16, without $LiNO_3$.

Figure 30 compares cells with and without $LiNO_3$ (cells 17 and 18), with a smaller voltage window achieved by adjusting the higher cutoff voltage. Similar oxidation peak positions (kinetics) are seen for both cells while charging to different potentials, proving that increasing the charging potential won't stop Li_2S from passivating the cell if the lower cutoff voltage remains the same. The same result from earlier research holds true: new Li_2S will always form at the end of discharge to passivate the electrode. More S_8 production at high voltage is responsible for the somewhat larger capacity in the larger window.

In general, the first oxidation peak's position generally serves as a reference for the oxidation kinetics, and its capacity indicates how much LiPSs was consumed during the decomposing reaction that created the passivation layer under low voltage. The first oxidation peak's position is primarily affected by passivation due to $LiNO_3$ decomposition, which will remain relatively stable after 10 cycles. The more reactive Li_2S passivation can be regulated every cycle to slightly alter where the first oxidation peak appears. The passivation and peak location are unaffected by higher cutoff voltage, however more comprehensive sulfur oxidation under high voltage results in a larger capacity. Passivation layer development and kinetics control are mostly influenced by the lower cutoff voltage.

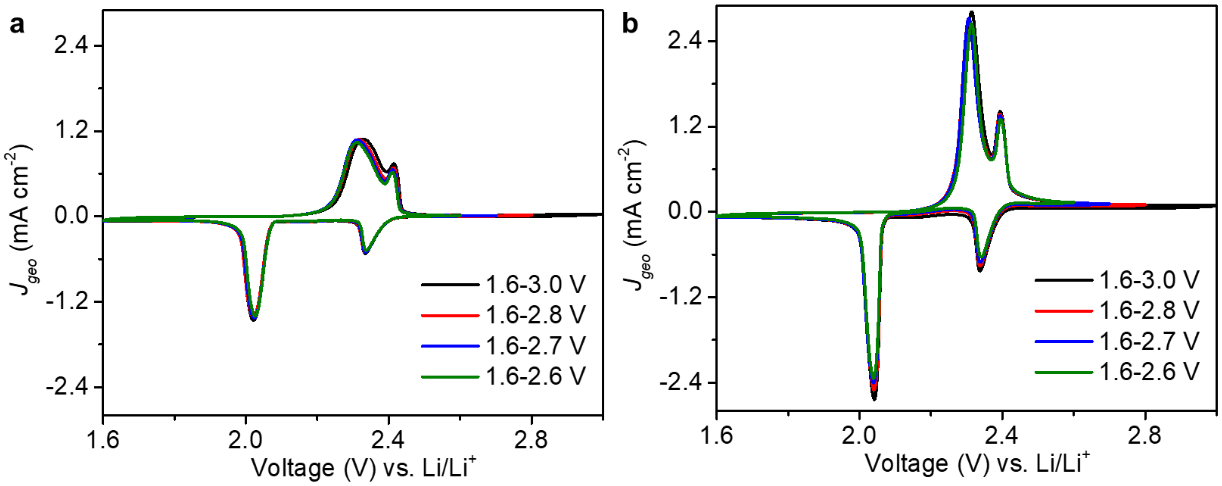

Figure 30. Li-S cells with high sulfur loadings, cycled within voltage windows with various higher cutoff voltages, after completing their first 10 cycles. **a,** Cell 17, with $LiNO_3$. **b,** Cell 18, without $LiNO_3$.

2.3.3 An Electrochemical Approach for Shuttling Evaluation and Oxidation Mechanism Study

As was previously noted, two oxidation peaks are blended. **Figure 31 a and b** show the CV graphs for the first nine cycles of Li-S cells cycled in a fixed window and with a relatively high sulfur loading. It has been reported that $LiNO_3$ is able to stabilize the lithium anode and improve the capacity by reducing the shuttling effect in the Li-S battery. In order to better understand the oxidation mechanism and $LiNO_3$'s influence on the shuttling behavior, we segmented the oxidation peaks and calculated the charges for cell 19 and 20. **Figure 32 c and d** display the peak splitting for two cells, cell 19 and cell 20, with and without $LiNO_3$. The first and second oxidation peaks are referred to as O_1 and O_2, respectively.

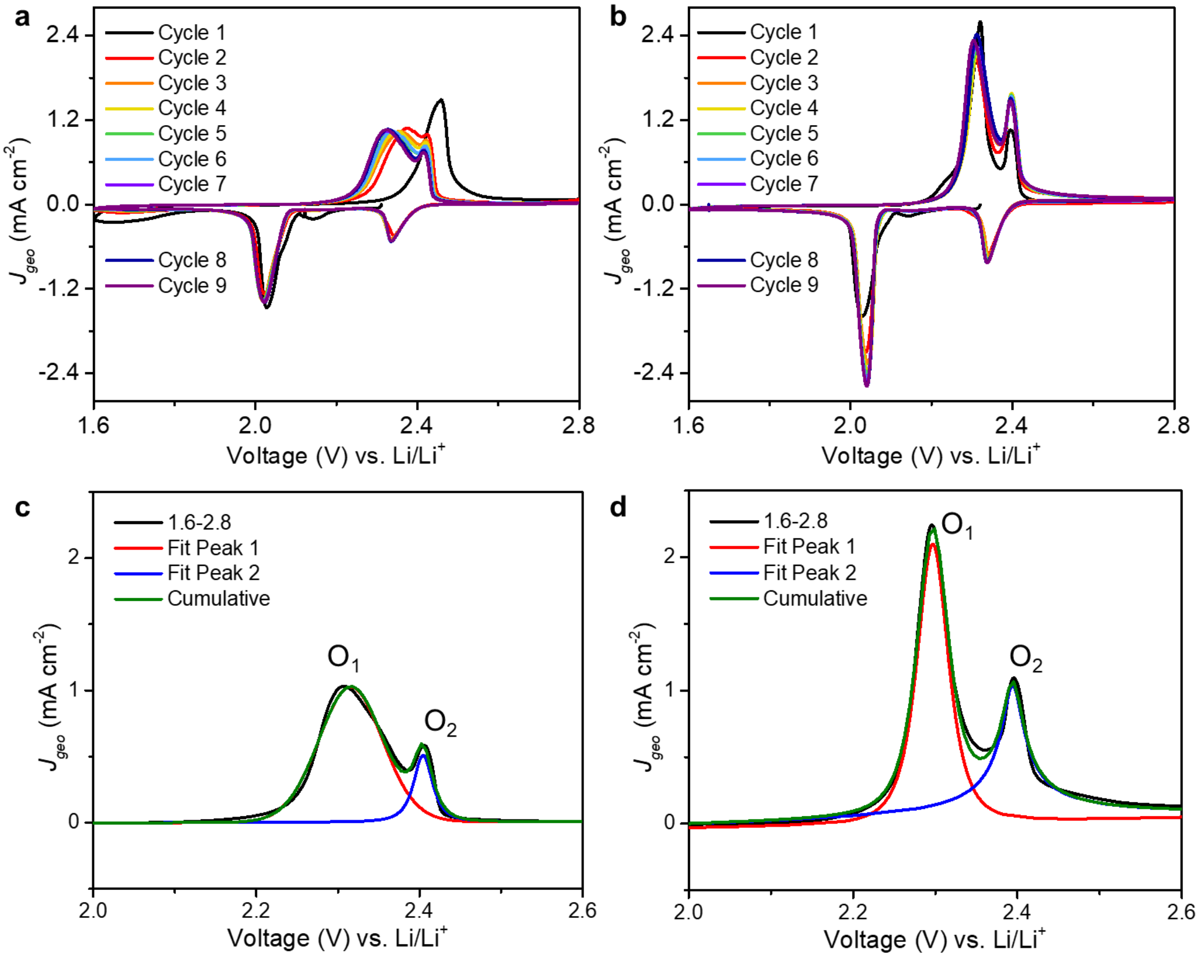

Figure 31. CV graphs and peak deconvolution results for Li-S cells cycled in a fixed window and with a relatively high sulfur loading. **a,** Cell 19, with $LiNO_3$. **b,** Cell 20, without $LiNO_3$.

Table 3. Charge number calculated from CV for cell 19. All charge numbers are in the unit of Coulombs (C).

Cycle number	O^a	R^b	(O-R)	O_1^c	O_2^d	$[O_2$-(O-R)]	$O_1/[O_2$-(O-R)]
3	1.5899	1.6439	-0.0540	1.4171	0.2266	0.2806	5.05
4	1.5975	1.6441	-0.0466	1.4202	0.2255	0.2721	5.22

5	1.5958	1.6316	-0.0358	1.4093	0.2310	0.2668	5.28
6	1.5924	1.6251	-0.0327	1.4142	0.2191	0.2518	5.62
7	1.5879	1.6121	-0.0242	1.4000	0.2264	0.2506	5.59
8	1.5805	1.6052	-0.0247	1.3879	0.2300	0.2547	5.45
9	1.5707	1.5885	-0.0178	1.3733	0.2328	0.2506	5.48

[a] O: capacity of oxidation process

[b] R: capacity of oxidation process

[c] O_1: capacity of first oxidation peak by peak deconvolution

[d] O_2: capacity of second oxidation peak by peak deconvolution

Table 4. Charge number calculated from CV for cell 20. All charge numbers are in the unit of Coulombs (C).

Cycle number	O[a]	R[b]	(O-R)	O_1[c]	O_2[d]	[O_2-(O-R)]	O_1/[O_2-(O-R)]
3	2.7784	1.8988	0.8796	1.7656	1.2410	0.3614	4.89
4	2.7730	1.9830	0.7900	1.7546	1.2046	0.4146	4.23
5	2.8068	2.0323	0.7745	1.7302	1.2429	0.4684	3.69
6	2.8788	2.0646	0.8142	1.7283	1.3038	0.4896	3.53
7	2.9367	2.0732	0.8635	1.7476	1.3433	0.4798	3.64
8	2.9852	2.0757	0.9095	1.8960	1.3727	0.4632	4.09
9	3.0276	2.0560	0.9716	1.7756	1.4140	0.4424	4.01

[a] O: capacity of oxidation process

[b] R: capacity of oxidation process

[c] O_1: capacity of first oxidation peak by peak deconvolution

[d] O_2: capacity of second oxidation peak by peak deconvolution

We see that cell 20 exhibits a serious overcharge issue when comparing cells 19 and 20 cycling within the same voltage window for a number of cycles. Additionally, cell 20 has a similar capacity for O_1 but a significantly larger value for O_2, and the difference between cells 19 and 20 for (O-R) (the overcharge component) is roughly the same as their difference for O_2. This demonstrates that O_2 includes this shuttling component and contributes to the overcharge, which is consistent with our assumptions that the cell without $LiNO_3$ will experience a more severe shuttling that results in a significant overcharge event. After eliminating the overcharge part from O_2, the ratio between O_1 and $[O_2\text{-(O-R)}]$ reflects the charge ratio between two phases for oxidation, which is 4~5 in our situation indicating a stable intermediate of Li_2S_5 or Li_2S_6. Therefore, the sulfur oxidation process can be divided into two stages including the first one from Li_2S to Li_2S_5/Li_2S_6 and the second one from Li_2S_5/Li_2S_6 to S_8, while shuttling occurs primarily in the second half as a result of Li_2S_5/Li_2S_6 loss, which is signaled by an overcharge phenomenon during cycling. One thing to note is that even though we claim to be employing relatively high sulfur loading, the loading is still very low compared to a commercial level, and the $LiNO_3$ decomposition will consume some of the catholyte's LiPSs, hence resulting in cell 19's lower capacity than cell 20's.

This overcharge and shuttling can be explained by the polysulfide equilibrium in the cell. Li_2S_6 may diffuse to the lithium anode and get reduced there regardless of discharge or charge, either being reduced to Li_2S and permanently lost on the anode, or being partially reduced to lower order polysulfides. Lower order polysulfides are not completely in a solid form hence can diffuse back to the sulfur cathode to perform either oxidation or reduction depending on the working status of the cell (charge or discharge). Electrons from lithium are offered during discharge for both the external circuit and the shuttled higher order polysulfides, but only the external circuit portion is taken into account when calculating capacity, hence the electrons provided from lithium metal to these shuttled higher order polysulfides equal to the capacity lost due to shuttling. Likewise, higher order polysulfides formed during charge will diffuse to the lithium anode for reduction and, if partially reduced, will diffuse back to the cathode for oxidation. Once they have been oxidized, they can once more diffuse to the anode, forming a continuous back-and-forth movement between the cathode and anode that may even reach equilibrium and continue indefinitely. The equilibrium could only be disturbed if the oxidation on the sulfur cathode is quick enough or the LiPSs are halted on their way diffusing. Therefore, if there was excessive polysulfide shuttling, a significant overcharge would be observed. By stabilizing the SEI on lithium surface and preventing the reaction between fresh lithium and shuttled LiPSs, $LiNO_3$ is able to reduce the overcharge and improve the Coulombic efficiency.

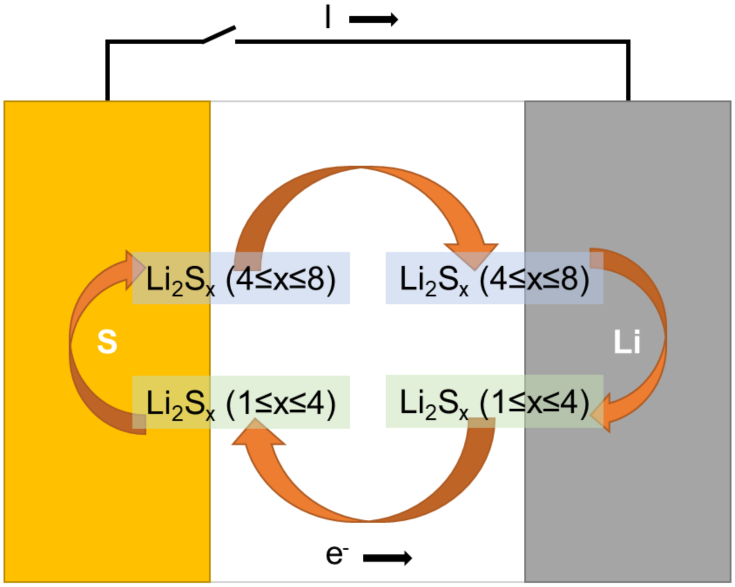

Figure 32. Schematic showing the polysulfide equilibrium causing shuttling in Li-S battery.

2.4 Conclusion

CV is an important electrochemical evaluation approach to study the mechanism underlying the functioning of Li-S batteries. This work investigated the sulfur electrode passivation situation using CV within various voltage windows and explored the oxidation and shuttling mechanism based on charge number calculations. Prior to conducting the subsequent assessment, we first went over the charge calculation process on CV plots and established some key parameters. Then, by designing cells with various $LiNO_3$/LiPSs ratios to distinguish the impacts between $LiNO_3$ and Li_2S, we looked into how they passivate the sulfur cathode. In low voltage regimes, $LiNO_3$ severely passivates the electrode, and once stabilized, its degradation provides a stable passivation layer that is difficult to modify. Relatively speaking, Li_2S likewise exhibits the passivation effect in the low voltage domain, but goes through cycles of deformation and reformation. When the lower cutoff voltage is raised, the passivation can be alleviated even in cells that have already been deeply discharged and passivated. To further investigate the oxidation and shuttling mechanism, the two oxidation peaks were deconvolved. There are two main stages during oxidation, with Li_2S_5/Li_2S_6 serving as an intermediate between Li_2S and S_8. Since the second step's starting reagent is quite soluble, it can build an equilibrium known as "shutting" by continuously moving back and forth between the anode and the cathode. Only in the second stage does the shuttling process take place, which results in an insanely high second peak of CV and an overcharge phenomenon in the cell. Along with passivating the sulfur cathode, $LiNO_3$ is also capable of stabilizing the lithium anode and preventing reactions between lithium and LiPSs to address the shutting issue.

CHAPTER 3: FUNDAMENTAL REACTION NETWORK CONSTRUCTION FOR SULFUR REDUCTION REACTION IN LITHIUM SULFUR BATTERIES

3.1 Introduction

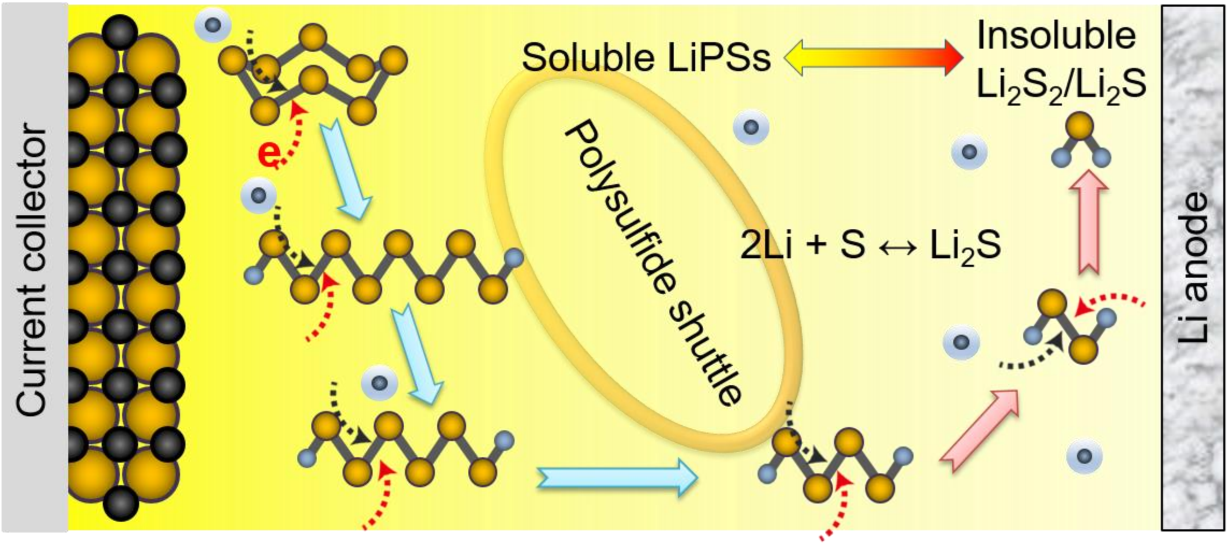

Figure 33. Schematic illustration of the sulfur reduction reaction process involving the lithium polysulfide evolution.

The conversion of the S_8 cathode to the Li_2S solid during the discharge process in lithium sulfur (Li-S) batteries constitutes the sulfur reduction reaction (SRR), a multistep 16-electron process involving a series of lithium polysulfide (LiPS) intermediates with complex and sluggish kinetics. The accumulation of soluble LiPSs in the electrolyte induces serious shuttling problem between cathode and anode, which further leads to severe active material loss and fast capacity fading[38,134,144]. Catalysis has been proven to be an efficient approach to reduce the accumulation of the soluble LiPS species and eventually mitigate the shuttling problem[60,61,64,65,70,131,145,146]. Despite extensive efforts devoted to improving the practical performance of Li-S batteries[134,147-152], the fundamental reaction mechanism remains unsettled. The 16-electron conversion process involves a complex reaction with numerous possible interwoven branches among different LiPSs. The main branch in this reaction network for SRR remains a topic of considerable debate[83,84,87,88,153-155]. Deciphering such reaction network and understanding the relevant mechanism is essential for the rational design of the catalysts that can accelerate the polysulfide conversion process and combat LiPS shuttling effect. As demonstrated in **Chapter 1 and 2**, heteroatom-doped holey graphene frameworks can function as a conductive scaffold and exhibit tunable catalytic properties in SRR[70,131] and hence serve as a good model system for investigating the fundamental reaction mechanism.

Various approaches have been considered to elucidate the mechanism of SRR[83,84,86,87,90,153,154]. Galvanostatic voltammetry has been conducted to provide information on the capacity ratio of different stages in SRR, but suffers from the ambiguous separation between different steps[81,87]. By comparison, cyclic voltammetry (CV) provides clearer boundaries for differentiating reaction steps[82], but an extremely slow sweep is needed for a complete reaction; thus, CV is rarely used in the quantification of charge transfer numbers in batteries. Previously, we have developed the key parameters for charge analysis in CV in **Chapter 2**. By carefully removing the side effect on the main reaction steps and selecting reasonable regions for charge number calculation, we aim to establish a preliminary network using the results from CV measurements.

Furthermore, detailed mechanistic studies based on solely electrochemistry are generally challenging, due to the complex convolution of multiple electrochemical reactions as well as nonelectrochemical side reactions (e.g., disproportionation/comproportionation reactions between different LiPSs[83,87,156]) at the same potential. It is generally difficult to separate/delineate these different reactions within the complex SRR network based only on CV characteristics. To this end, advanced *in situ* characterization to identify and track different LiPS species, generated electrochemically or non-electrochemically, is essential for interpreting and corroborating CV characteristics. *In situ* Raman has been used to explore the SRR mechanism in Li-S batteries since a long time ago. However, the interpretation is very challenging due to the incredibly complicated and moderate polysulfide signal. By carefully choosing focus points that would enhance the Raman signal and systematically deconvolving the overlapping peaks to optimize peak assignments, we hope to create a library of polysulfide Raman spectra and learn polysulfide evolution behavior based on Raman analysis.

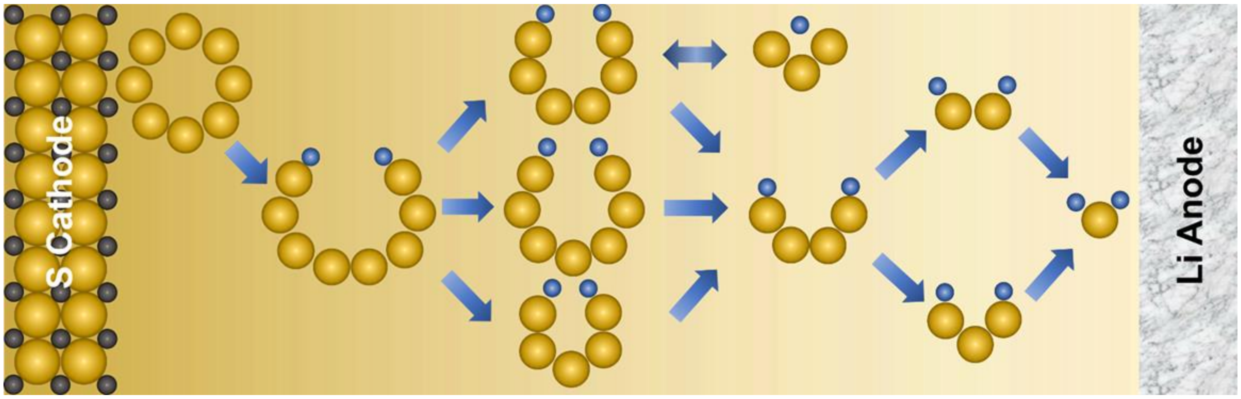

Figure 34. Schematic illustration of the sulfur reduction reaction network involved in the Li-S battery.

In this chapter, combining CV, *in situ* Raman spectroscopy and density functional theory (DFT) energetics, we elucidated the dominant reaction pathway before and after the central Li_2S_4 intermediate, identify the key species as S_8, Li_2S_8, Li_2S_6, Li_2S_4, and Li_2S, and determined that the non-electrochemical disproportionation/comproportionation reaction between Li_2S_8 and Li_2S_4 is the main path for forming or removing Li_2S_6.

3.2 Experimental

3.2.1 Electrochemical Measurements

The synthesis N,S-HGF electrode was done as described in **Chapter 2**. The electrochemical performance of the catalyst was conducted in the CR2032 coin cells assembled in an argon-filled glovebox. The catalyst electrode was prepared by directly pressing the aerogel into a freestanding thin film. Afterwards, the 0.1 M Li_2S_6 catholyte (prepared according to the procedure in **Chapter 2**) was directly used as sulfur source to drop cast in the catalyst electrode. In our experiment, we set the mass ratio of the sulfur in the cathodes as 33% to ensure a complete conversion from S_8 to Li_2S for mechanistic understanding. The sulfur cathodes were then directly assembled into a CR2032 coin cell with lithium foil, Celgard 2500 separator and blank electrolyte. CV curves were recorded in the voltage range of 1.6 V-2.8 V at a scanning rate of 0.05 mV s^{-1}.

3.2.2 *In situ* Raman Spectroscopy Measurements and Data Analysis

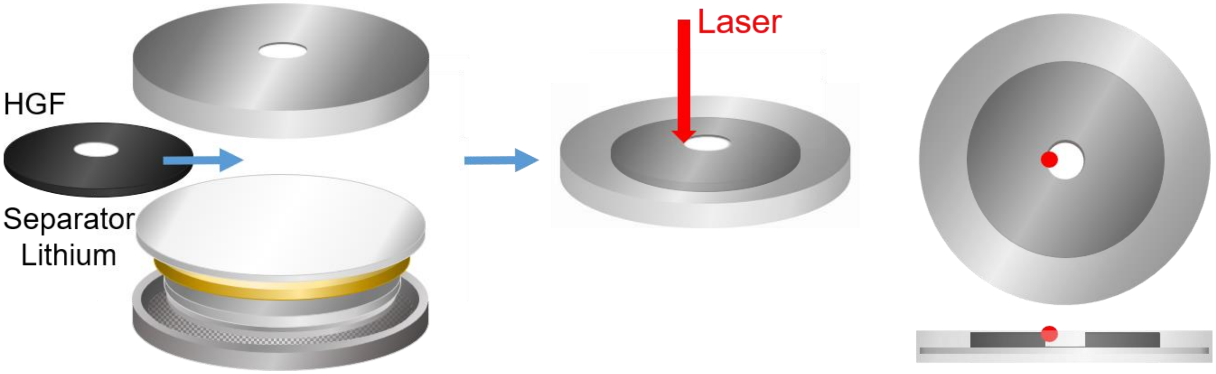

Figure 35. Schematic illustration of the *in situ* Raman cell and laser focus point during Raman spectra collection. N,S-HGF/HGF electrode with a small hole punched at the center was used for *in situ* Raman cell. The laser was focused on the electrolyte at the boundary between the electrode and electrolyte.

In situ Raman spectroscopy measurements were collected by LN2 cooled CCD array detector, using a Horiba Jobin Yvon T64000 open-frame confocal microscope using 10X objective follow by a triple monochromator leading to high spectral resolution (down to 0.15 cm^{-1}). The sample was subject to 514 nm laser for a 5 sec and averaged 70 times. The data were collected with a 1800 cm^{-1} grating, and 500 μm slit. For the *in situ* Raman, a regular coin cell is modified with a transparent window on the cathode side to allow the laser in. A same procedure as that in the electrochemical measurements was used to assemble the homemade Raman cell. The laser was focused on the electrolyte near the boundary between HGF and electrolyte (**Figure 35**). The Raman cell was running with a discharge CV scan at 0.05 mV s^{-1} when Raman data were collected.

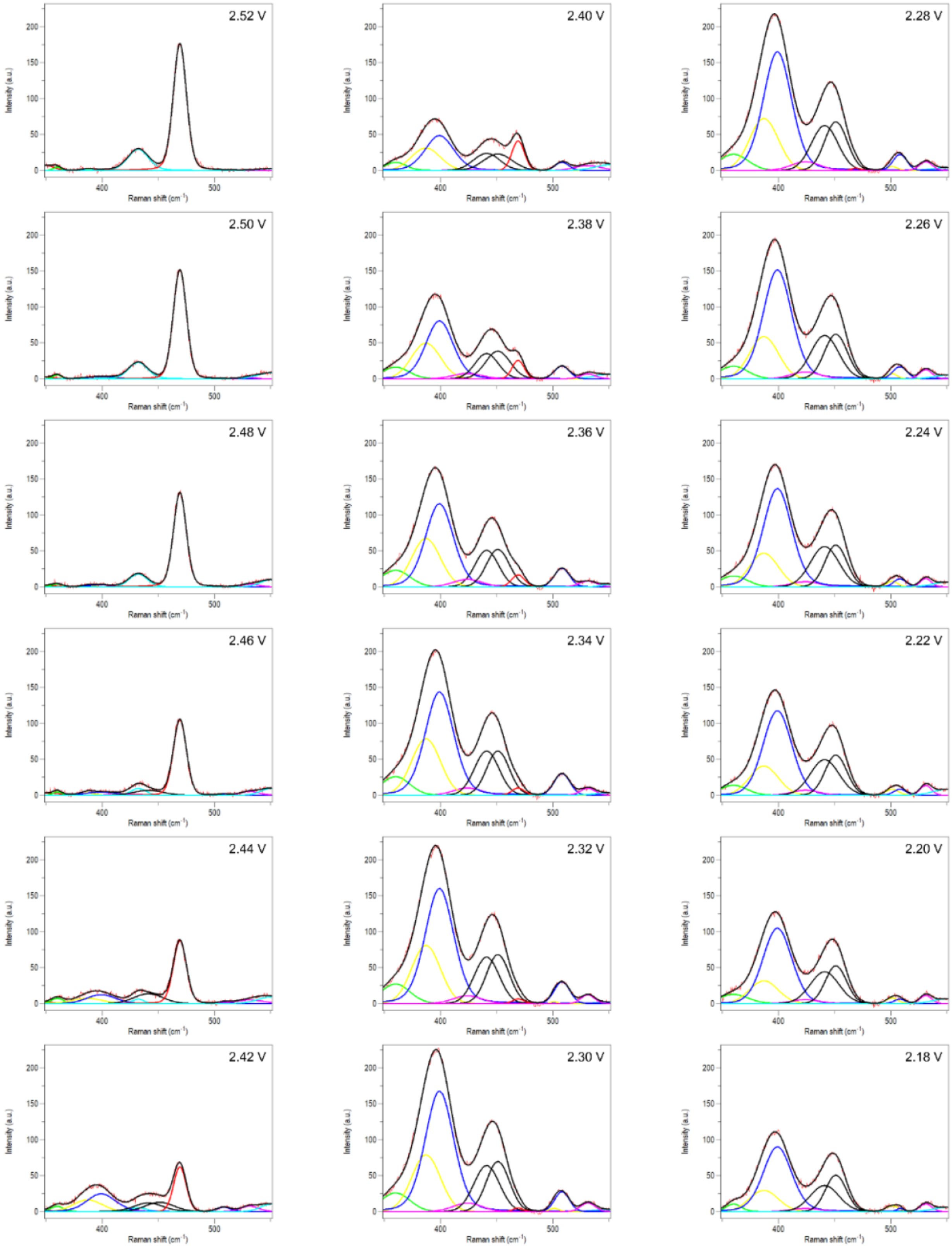
2.52 V
2.50 V
2.48 V
2.46 V
2.44 V
2.42 V
2.40 V
2.38 V
2.36 V
2.34 V
2.32 V
2.30 V
2.28 V
2.26 V
2.24 V
2.22 V
2.20 V
2.18 V
Intensity (a.u.)
Raman shift (cm⁻¹)
0
50
100
150
200
400
500

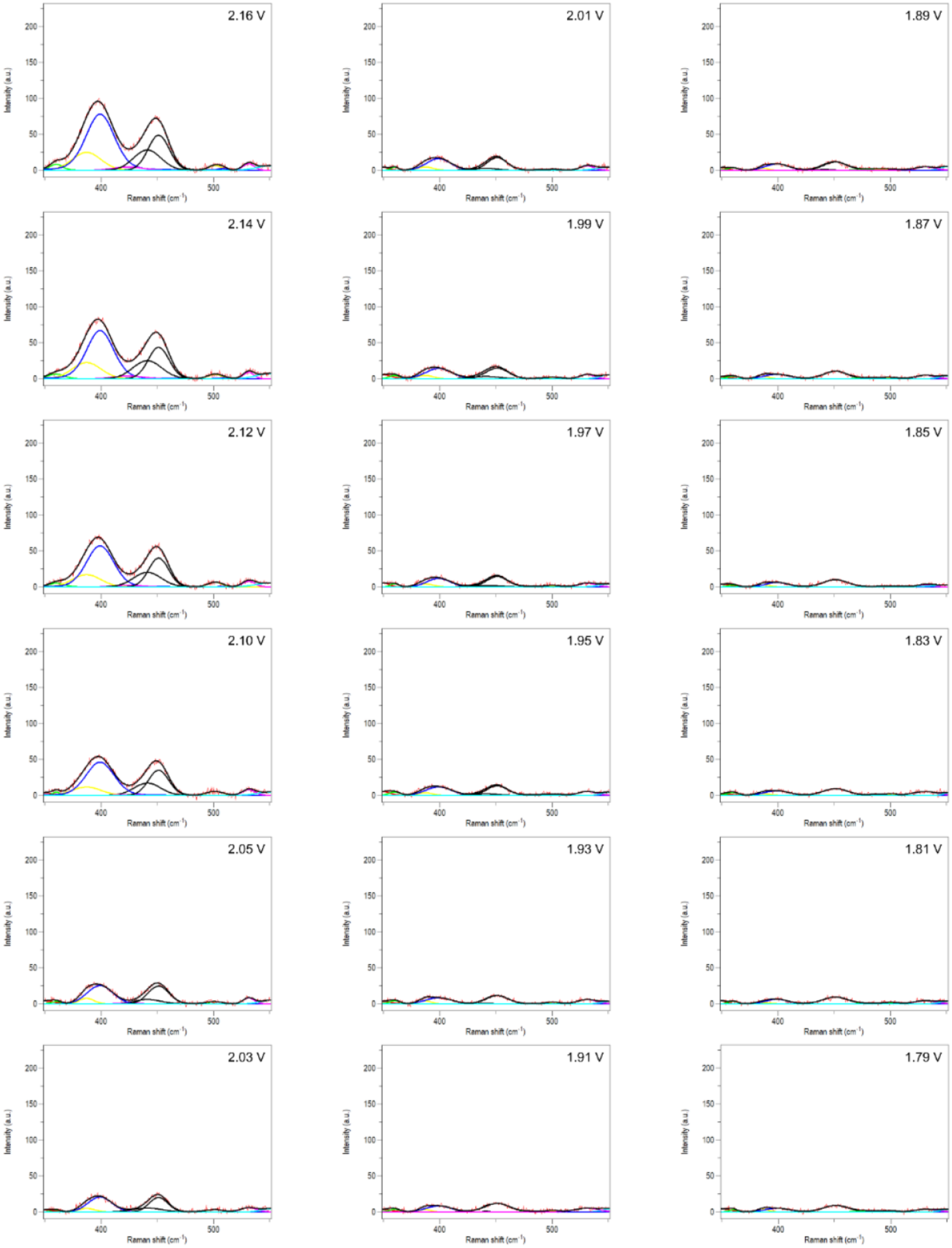
2.16 V
2.01 V
1.89 V
2.14 V
1.99 V
1.87 V
2.12 V
1.97 V
1.85 V
2.10 V
1.95 V
1.83 V
2.05 V
1.93 V
1.81 V
2.03 V
1.91 V
1.79 V
Intensity (a.u.)
0
50
100
150
200
400
500
Raman shift (cm⁻¹)

Figure 36. Peak deconvolution for different polysulfide species in N,S-HGF Raman spectra under different voltages during discharge.

Peak deconvolution and assignments for different polysulfide species in N,S-HGF Raman spectra under different voltages during discharge was done systematically using a homemade program for baseline subtraction and LabSpec for peak splitting. The *in situ* data were first corrected by “blank” subtraction: as the blank electrolyte shows multiple peaks in the interested wavelength range, a “blank” spectrum was collected using the same cell setup without active sulfur added and subtracted from the *in situ* data to eliminate the influence from electrolyte peaks. Subsequently, the *in situ* data were corrected by subtracting the baseline. The preprocessed data were then opened in LacSpec software to conduct the peak deconvolution and assignment for different LiPSs.

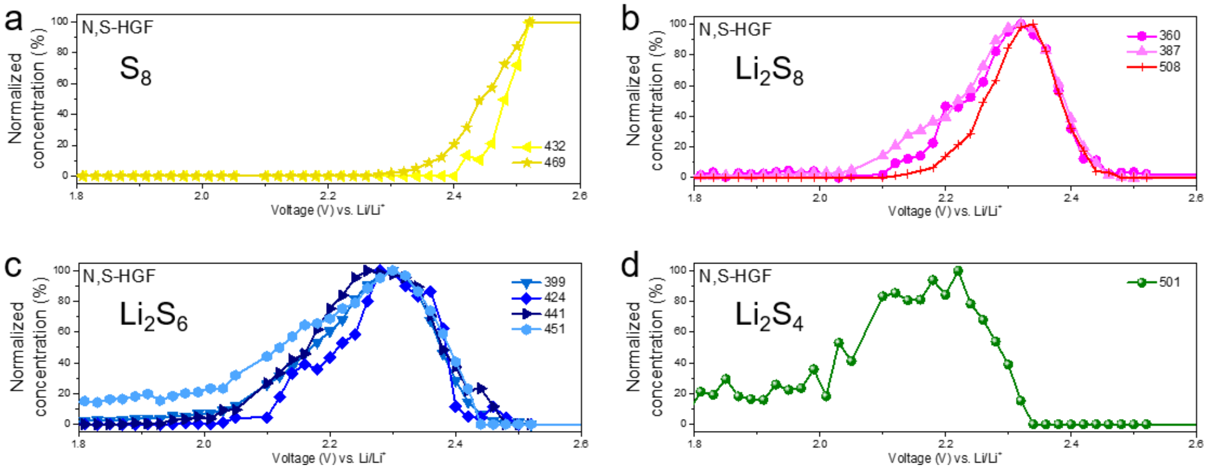

Figure 37. Raman peak assignments of S_8 and Li_2S_x (x=4, 6, 8). Voltage dependent concentration curves for S_8 (**a**), Li_2S_8 (**b**), Li_2S_6 (**c**), Li_2S_4 (**d**) in N,S-HGF are derived from experimental *in situ* Raman spectra. Multiple peaks due to different vibrational modes are observed for each polysulfide species during peak fitting. Numbers shown in the legends are peak positions in the unit of cm^{-1}. Each curve is normalized with respective to its highest peak area.

Characteristic peaks for S_8 at 432 cm^{-1} and 469 cm^{-1} confirm the presence of solid S_8 in the beginning of discharge and exhaust soon after SRR begins. Peaks at 360 cm^{-1}, 387 cm^{-1}, and 508 cm^{-1} show the same trends and provide evidence for Li_2S_8 in high voltage region. These peaks disappear in the middle voltage region of SRR. 508 cm^{-1} is the most distinguishable peak on the spectrum even without fitting, thus was selected as the characteristic peak of Li_2S_8 for quantification. Four peaks at 399 cm^{-1}, 424 cm^{-1}, 441 cm^{-1}, and 451 cm^{-1} show similar trends and are assigned as Li_2S_6 peaks. 399 cm^{-1} peak was selected for quantification because it shows a general trend for all Li_2S_6 peaks. Li_2S_4 features strong peak at 501 cm^{-1}, which gradually appears as Li_2S_8 peak at 508 cm^{-1} starts to disappear. This peak exists until low voltage region. These peak assignments match well with previous reports[91,92,96,157] and our simulated results.

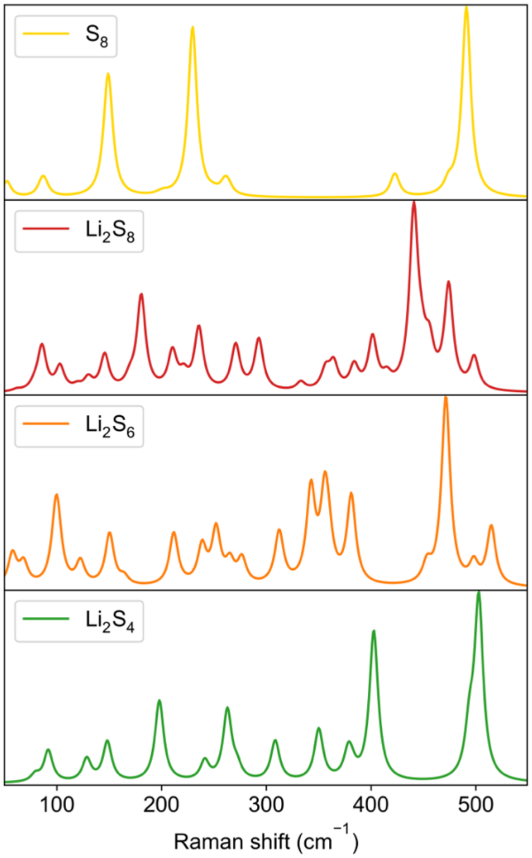

Figure 38. Simulated Raman spectra using the SCAN functional.

Table 5. Peak positions of LiPSs in experimental and simulated Raman spectra compared with literature results. All peak positions are in the unit of cm^{-1}.

	S_8	Li_2S_8	Li_2S_6	Li_2S_4

ref[158]		110, 282	176, 322, 399, 456	
ref[93]		155, 219, 478	324, 416	470
ref[96]	150, 219, 474		398, 509	202, 445
ref[159]	218	282	176, 322, 399, 456	
ref[91]		150, 219, 478	398	413
ref[157]		398		201, 453, 490
ref[160]	151, 216, 435, 470		200, 410, 460	
ref[161]	152, 221, 474		400, 450	
ref[162]		119, 279, 396	178, 397, 458	
ref[163]		279	178, 397	
ref[96] (simulated)	141, 209, 474	435, 440, **454**[*], 462	193, 378, **397**, **461**	355, 389, **444**, **476**
ref[91] (simulated)		**371, 402**, 420, 430, **453,** 470, 480, 492, 508	380, 412, 458, 491	385, 430, 488
Simulated in this work	150, 230, 491	364, 383, **401**, 415, **440**, 448, 455, **474**, 498	**355**, 359, **381**, 453, **471**, 498, **514**	378, **402**, 494, **502**
Experimental in this work	469	508	399	501

[*] Peaks in bold show stronger intensities than other vibration modes.

3.2.3 DFT Calculations

DFT calculations were performed using the Vienna ab initio simulation package[164]. The strongly constrained and appropriately normed (SCAN) functional[165] was used. Solvation effects were described using a micro-solvation model: the first solvation shell was described using explicit DOL molecules, and the rest was described by an implicit dielectric model as implemented in the VaspSol[166] addon package. The Raman cross section was calculated within the double harmonic approximation. All calculations were performed with a cutoff energy as at least 500 eV.

3.3 Results and Discussion

3.3.1 Reaction Network in Sulfur Reduction Reaction and Cyclic Voltammetry Results

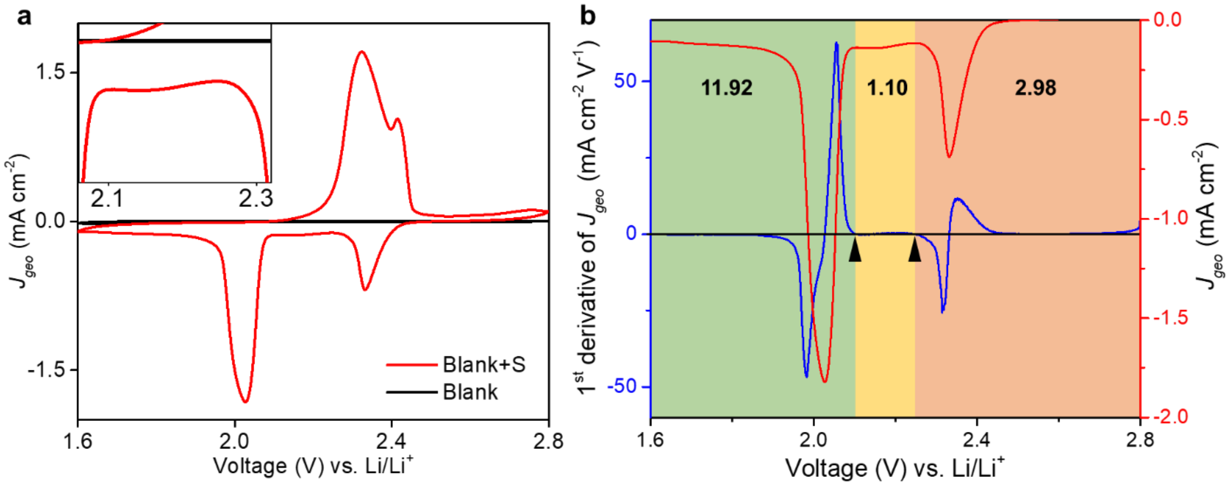

Figure 39. CV analysis of the sulfur reduction reaction in Li-S battery with N,S-HGF catalysts. **a,** The black baseline is obtained using the same N,S-HGF in the blank electrolyte without sulfur, indicating the negligible double layer capacity contribution to the overall capacity. **b,** CV and first derivative of current density versus voltage.

To better understand the different stages in the SRR, we performed CV measurements, followed by quantitative charge analysis by integrating the peak area in different potential regions. The black baseline in **Figure 39a** was obtained using N,S-HGF without sulfur in the blank electrolyte, indicating the negligible double layer capacity contribution to the overall capacity. Learning from **Chapter 2** about the charge calculations on CV curve for sulfur reactions, charge number calculation was done as shown in **Figure 39b**. Voltage ranges for integration on CV were determined by the first derivative of current density.

The CV curve of SRR with N,S-HGF (red curve in **Figure 39a**) exhibits two main peaks during the discharge process, with the first one appearing in the voltage range of ~2.2-2.5 V and the second one in the range of ~1.9-2.1 V. The charge number calculated from the integrated area in CV is compared with the total charge number and converted to the formally electron transfer number in a full 16 e^- process. By separating the overall process at the onset of the second peak, 2.11 V, a charge transfer ratio of 4.08:11.92 (≈1:3) was obtained. This charge transfer ratio (1:3) suggests Li_2S_4 to be the primary intermediate species separating these two reduction peaks, as the reaction $S_8+4Li^++4e^- \rightarrow 2Li_2S_4$ involves 4 electrons out of the formally overall 16 electrons transferred, and the subsequent conversion $2Li_2S_4+12Li^++12e^- \rightarrow 8Li_2S_4$ involves 12 electrons.

Interestingly, a non-zero plateau was observed in the voltage range of ~2.11-2.25 V between the two peaks, as highlighted in the inset of **Figure 39a**. To determine the origin of such a non-zero plateau, we have more carefully integrated and compared the charge in different potential range. The charge integration results, as shown in **Figure 40a** with colored regions, illustrate the non-negligible contribution of the plateau region between two major redox peaks: ~1 out of 16 electrons per S_8 molecule in SRR. The double layer capacity contribution to this plateau has been eliminated by comparison with the CV results of control group without sulfur, shown as the black baseline in **Figure 39a**. Considering the instability and complexity of polysulfides[83,87,156], several potential disproportionation/comproportionation reactions involving Li_2S_8 and Li_2S_4 in this potential range are further explored. Although the disproportionation reactions are not directly detectable *via* CV measurements, the potential ranges of electrochemical reactions are affected and further reflected in the CV results (e.g., contributing to the formation of non-zero plateau between two main redox peaks). To investigate the chemical origin of such a plateau and decipher the detailed mechanism connecting the two main redox peaks, we have used *in situ* Raman spectroscopy to probe the specific reaction intermediates and first principles calculations to explore the fundamental energetics among different polysulfide intermediates.

The computational modeling of the SRR network starts with the conversion from the S_8 molecule to the Li_2S_8 molecule, giving the highest calculated output potential among all the steps, 2.34 V (**Figure 40d**). The further conversion of the Li_2S_8 molecule involves multiple possible branches: in a 2 e^- process, it can be converted into (1) one Li_2S molecule paired with one Li_2S_7 molecule, (2) one Li_2S_2 molecule paired with one Li_2S_6 molecule, (3) one Li_2S_3 molecule paired with one Li_2S_5 molecule, or (4) two Li_2S_4 molecules. The calculated energetics shows that the Li_2S_4 pathway is the most exergonic and hence the favored one, yielding an output potential of 2.16 V.

As the experimentally observed plateau might be originated from the delayed electrochemical conversion of disproportionation or comproportionation products, we checked the possibilities starting with one Li_2S_8 molecule and one Li_2S_4 molecule, or two Li_2S_4 molecules, and found that the reaction $Li_2S_8+Li_2S_4 \rightarrow 2Li_2S_6$ is the only exergonic one, with a reaction Gibbs free energy of -0.16 eV. We further checked the disproportionation reaction with either Li_2S_8 and Li_2S_6 molecules, or Li_2S_4 and Li_2S_6 molecules, but in both cases the reactions were found to be endergonic. These results suggest that Li_2S_6 formation by comproportionation of Li_2S_4 and Li_2S_8 is the only chemical elementary step that competes with the electrochemical reaction network, and that other disproportionation/comproportionation reactions are not significant.

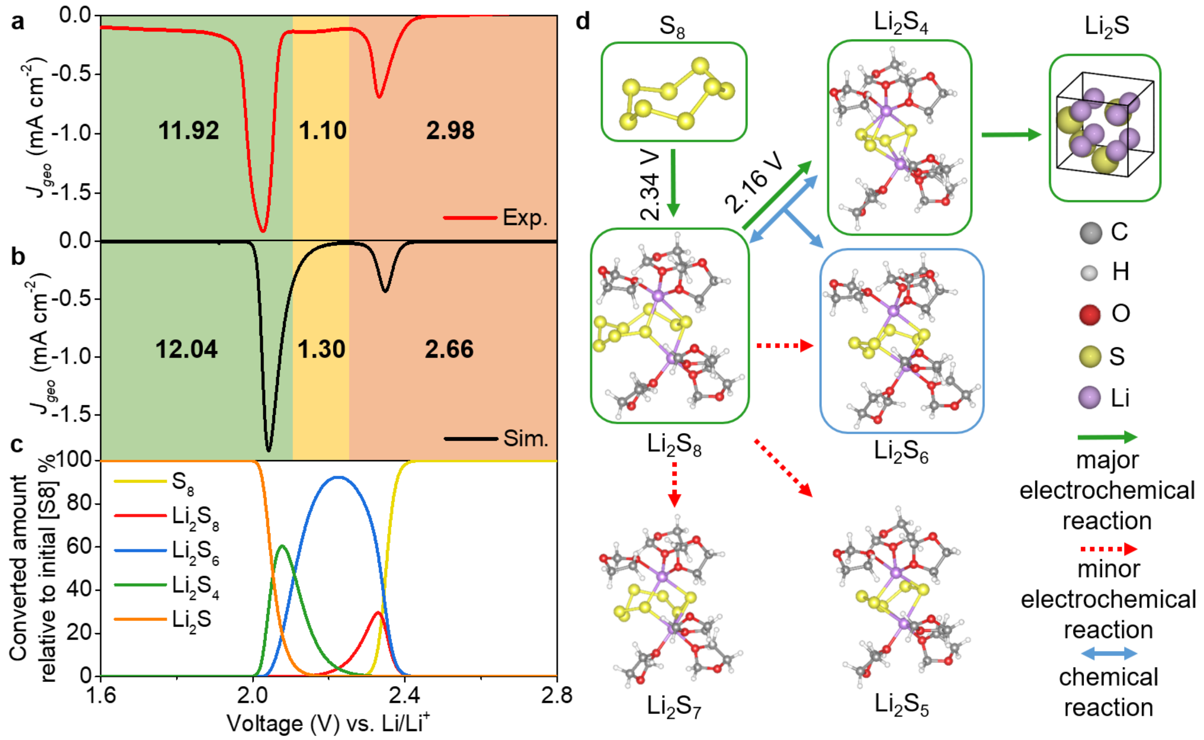

Figure 40. Charge analysis and reaction network for the sulfur reduction reaction. **a,** Experimental CV curve with the charge integration results, separated into three potential regions with a charge ratio as 2.98:1.10:11.92 from high potential to low potential. **b,** Simulated CV curve from first principles with the charge integration results, separated into the same three regions as in (a) with a charge ratio as 2.66:1.30:12.04. **c,** Simulated voltage dependent concentrations of the major species considered: S_8, Li_2S_8, Li_2S_6, Li_2S_4 and Li_2S. The concentrations are normalized according to the sulfur amount. **d,** The dominant reaction mechanism suggested by DFT energetics: $S_8 \rightarrow Li_2S_8 \rightarrow 2Li_2S_4 \rightarrow 8Li_2S$ ($Li_2S_8 + Li_2S_4 \rightleftarrows 2Li_2S_6$) where the chemical disproportionation part is in parentheses. Solid green and dotted red lines indicate major and minor electrochemical reactions, respectively. Blue lines indicate chemical reactions. Major products are labelled with green and blue boxes, corresponding to electrochemical and chemical origin. Thermodynamic output potentials are denoted for major electrochemical reactions.

Combining the aforementioned balances from DFT (**Figure 40d**), with the effects of voltage, the potential dependent concentrations of different polysulfides were simulated, giving a sequence of dominant LiPS species as S_8, Li_2S_8, Li_2S_6, Li_2S_4, and Li_2S with reducing potential (**Figure 40c**). The simulated CV curve was further derived from the simulated concentrations, giving the charge ratio as 12.04:1.30:2.66, in the green, yellow and orange zones of **Figure 40b**, respectively, which matches well with the experimental ratio in **Figure 40a** obtained with the same potential zones.

Although Li_2S_6 appears right after Li_2S_8, it is not formed by electrochemical reduction of Li_2S_8. Instead, a fraction of Li_2S_8 (~1/3) is electrochemically transformed into Li_2S_4, providing a fractional amount of charge in the orange region of **Figure 40 a and b** (~2/3 e), while the rest is involved in the comproportionation with the produced Li_2S_4 to yield a large concentration of Li_2S_6 at ~2.25 V. Note that the exergonic nature of the $Li_2S_8+Li_2S_4 \rightarrow 2Li_2S_6$ comproportionation provides additional driving force to initiate the electrochemical reduction of Li_2S_8 to Li_2S_4 at a potential higher (~2.35 V) than its equilibrium (2.16 V). At lower potential, in the yellow zone, where electrochemical reduction of Li_2S_8 to Li_2S_4 becomes exergonic, the comproportionation reaction operates backwards to produce Li_2S_4 and Li_2S_8 ($2Li_2S_6 \rightarrow Li_2S_8+Li_2S_4$), in which Li_2S_8 is electrochemically reduced to Li_2S_4 to result in the charge plateau seen in the yellow region. We have considered the direct reduction of Li_2S_6 to Li_2S_4, Li_2S_3 or other lower order polysulfides, and found these reactions cannot occur at a potential higher than 1.89 V, and therefore the disproportionation reaction is the only viable path in this potential regime. At even lower potential in the green zone, Li_2S_4 is eventually reduced to Li_2S, involving the extra 12 electrons of the electrochemical reduction reaction. This multi-electron step will be further discussed below.

3.3.2 *In situ* Raman Study on Sulfur Reduction Reaction

With distinct Raman activity of elemental sulfur and polysulfides, *in situ* Raman spectroscopy offers an attractive technique for identifying and tracking polysulfide conversion process[91-94,96,158,167]. However, the peak assignment for different LiPSs are complicated and divergent in different studies, due to the instability of various LiPSs and lack of pure polysulfide standard samples. Peaks used for quantification in our analysis are selected based on their behavior during SRR process, previous reports[91,92,96,157], and our DFT simulated results: 501 cm^{-1}, 399 cm^{-1}, 508 cm^{-1} and 469 cm^{-1} for Li_2S_4, Li_2S_6, Li_2S_8, and S_8, respectively **(Figure 37)**.

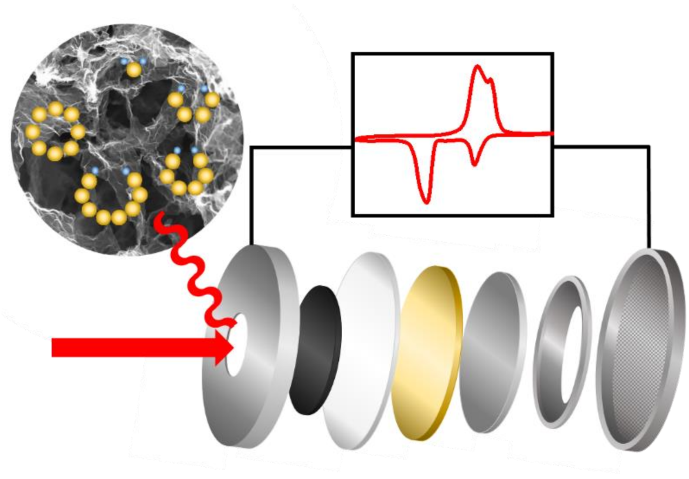

Figure 41. Schematic illustration of *in situ* Raman technique used in this study.

The *in situ* Raman spectra were taken along with a discharge CV scan. The CV curve, along with the voltage dependent *in situ* Raman spectra are shown in **Figure 42a and b**, respectively. In the beginning of the SRR process, the existence of elemental sulfur is confirmed by the typical S_8 peak at 469 cm^{-1}.[92] With reducing potential, S_8 signal gradually decreases and mostly disappears at ~2.36 V, accompanied by the emergence of the Li_2S_8 signal at 508 cm^{-1} starting at ~2.44 V. Nearly concurrently with the emergence of Li_2S_8, the Li_2S_6 peak at 399 cm^{-1} also emerged at ~2.44 V. As we discussed in the computation section, this occurs by electrochemical transformation of Li_2S_8 to Li_2S_4 and the rapid comproportionation between the formed Li_2S_4 and the remaining Li_2S_8 to form Li_2S_6. The Li_2S_8 peak at 508 cm^{-1} reaches its maximum at ~2.32 V, where a deconvoluted peak at 501 cm^{-1} emerges, indicating gradual depletion of Li_2S_8 and accumulation of Li_2S_4 in the system. The 508 cm^{-1} Li_2S_8 peak largely disappears at 2.18 V, while the Li_2S_4 peak at 501 cm^{-1} reaches its maximum. With decreasing potential, Li_2S_4 becomes the main polysulfides species. At the same time, Li_2S_6 resulted from the comproportionation reaction ($Li_2S_8+Li_2S_4 \rightleftarrows 2Li_2S_6$) is also present as a significant species. The Li_2S_6 peak at 399 cm^{-1} starts to decrease at ~2.30 V and almost disappears at 2.02 V. Similarly, most Li_2S_4 disappears at ca 2.00 V, indicating the conversion from

Li_2S_4 to Li_2S_x(x=1,2,3). It is noted that there is a small amount of Li_2S_4 remains at the low voltage region below 1.90 V, which might be due to incomplete conversion.

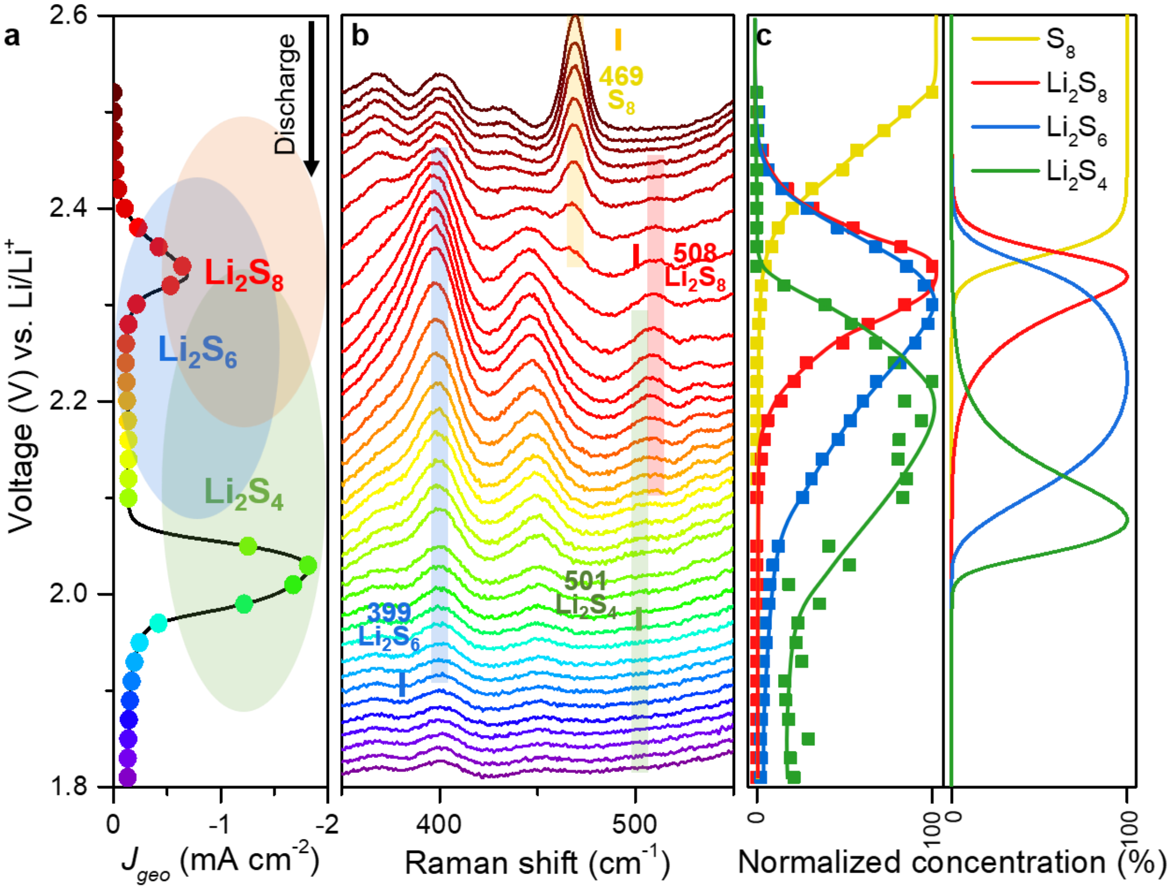

Figure 42. *In situ* Raman results during discharge with the N,S-HGF catalytic electrode. **a, b,** The CV profile (**a**) and the experimental *in situ* Raman spectra (**b**), where the same color indicates the same voltage. Characteristic peaks used to quantify the intermediates are marked with correspondingly colored shades. Small labels with darker color indicate the computed frequency values. **c,** The comparison between voltage dependent experimental concentrations (left panel) derived from *in situ* Raman spectra (**b**) and simulated concentrations from DFT (right panel). Each species is normalized with respect to its highest concentration.

The voltage dependent concentration profile of each LiPS was derived from the peak area and the results are shown in **Figure 42c** (left panel), with a comparison to the computational results shown in **Figure 42c** (right panel). The concentration is normalized with respect to the highest concentration of each species. The experimental and computational results give the same apparent concentration evolution sequence of S_8, Li_2S_8, Li_2S_6, Li_2S_4 with decreasing potential with comparable peak positions. It is interesting to note that Li_2S_6 appears at a similar potential as Li_2S_8 and roughly depleted at a similar potential as Li_2S_4, suggesting the dynamic balance between these three species through the back-and-forth disproportionation reactions discussed above.

We also note that the experimental peak for Li_2S_4 appeared at a slightly higher potential value (by 0.09 V) than the theory prediction. Only thermodynamics was considered in the simulated voltage dependent equilibrium concentration, while the formation of Li_2S_6 could be slow due to kinetics and diffusion barriers, and thus Li_2S_4 accumulation may start at a slightly higher voltage. The earlier accumulation of Li_2S_4 in experiment compared to purely thermodynamically predicted value further validates that the Li_2S_6 is originated from the comproportionation reaction. In summary, *in situ* Raman spectroscopy provides a semi quantitative polysulfide tracking, with an excellent agreement between spectroscopic feature evolution and DFT computed values, thus robustly validating the SRR molecular pathway obtained by theory: $S_8 \rightarrow Li_2S_8 \rightarrow 2Li_2S_4$ $(Li_2S_8+Li_2S_4 \rightleftarrows 2Li_2S_6) \rightarrow 8Li_2S$.

3.4 Conclusion

In conclusion, we were able to decipher the complex reaction network for 16-electron SRR by combining CV, *in situ* Raman, and DFT calculations. The CV curve of SRR shows two main reduction peaks in the voltage range of ~2.2-2.5 V and ~1.9-2.1 V, separated by a non-zero plateau, suggesting a non-trivial reaction network likely due to complex disproportionation/comproportionation reaction among different LiPS species. An exhaustive computational energetics survey of all possible reaction network predicts a most probable SRR molecular pathway: $S_8 \rightarrow Li_2S_8 \rightarrow 2Li_2S_4$ $(Li_2S_8+Li_2S_4 \rightleftarrows 2Li_2S_6) \rightarrow 8Li_2S$, in which Li_2S_4 represents the primary electrochemical intermediates, while Li_2S_6 is an electrochemical passive intermediate produced and consumed by the disproportionation/comproportionation reaction (Li_2S_8+Li_2S_4 ⇄ $2Li_2S_6$), related to the non-zero plateau in the CV. *In situ* Raman spectroscopy provides a semi quantitative tracking of the polysulfide concentration profile, showing an excellent agreement between spectroscopic feature evolution and DFT computed values, thus corroborating theory-predicted molecular pathway. In addition, *in situ* Raman further confirms that Li_2S_4 and Li_2S_6 represent the dominant intermediates, in which Li_2S_6 is generated by the comproportionation reaction between Li_2S_8 and Li_2S_4 and doesn’t directly participate in electrochemical reactions, but contributes to the shuttling problem due to its high solubility and energetically favorable accumulation in the electrolyte. This study for the first time resolves the fundamental reaction network in SRR by combined experimental and theory investigation, and the approach established here can be further applied in other catalytic systems to explore and compare sulfur reaction mechanisms. In the next chapter, we will discuss the influence of different catalysts on constructing the reaction pathway and regulating the reaction kinetics.

CHAPTER 4: THE ROLE OF CATALYSIS IN MODIFYING THE SULFUR REDUCTION REACTION NETWORK AND IMPROVING REACTION KINETICS

4.1 Introduction

With a theoretical capacity of 1,672 mAh g^{-1}, the 16-electron sulfur reduction reaction (SRR) process is very desirable for high-density energy storage, however the chemistry is hampered by slow sulfur reduction kinetics and the polysulfide (PS) shuttling effect.[34,134] These effects restrict the rate capability and cycle life in actual lithium sulfur (Li-S) cells. Fundamentally, these restrictions are related to the tedious and slow reduction reaction involving S_8 molecules. In general, incomplete conversion of S8 molecules into soluble lithium polysulfides (LiPSs) results from the insulating properties of elemental sulfur and its reduced derivatives as well as the slow charge transfer kinetics. Rapid capacity fading could ensue from these polysulfides moving through the separator to react with and deposit on the lithium anode.[144] A lot of work has gone into preventing the PS shuttling effect, usually by using a passive methodology in which different sulfur host materials are used to electrostatically or physically confine the LiPSs in the cathode structure.[35,40,168,169] These passive confinement/entrapping techniques have somewhat reduced the PS shuttling effect and increased performance, but they are inherently unable to stop LiPSs from dissolving into the electrolyte permanently.

The production, dissolution, and buildup of LiPS intermediates in the electrolyte are the causes of the PS shuttling effect. As a result, the soluble LiPSs continue to accumulate in the electrolyte, aggravating the PS shuttling effect due to the sluggish conversion kinetics of the soluble LiPSs into the insoluble end products.[25] In order to stop the buildup and shuttling of LiPSs, a catalytic method to speed up the conversion of soluble LiPS intermediates into insoluble Li_2S_2/Li_2S appears to be a natural course of action. The PS shuttling effect will be addressed while the rate capability was also improved by using catalysis. Although the idea of a catalytic approach has been proposed in a few recent studies,[64,146] the fundamental catalytic kinetics and mechanism of the SRR are largely unexplored, and the rationale for using such a catalytic effect to resolve the PS shuttling issues has not been adequately addressed.

Here we report a systematic investigation of the catalytic SRR mechanism. In the previous discussion in **Chapter 3**, we have comprehensively investigated the SRR pathway on nitrogen, sulfur dual-doped holey graphene framework (N,S-HGF) by combining cyclic voltammetry (CV), *in situ* Raman, and density functional theory (DFT) calculations. The similar approaches were applied in different catalysts in this chapter to study how catalysts affect the SRR mechanism. We have chosen the previously developed catalysts N,S-HGF and non-doped HGF as model systems to explore the impact of different catalysts in modifying the reaction network and kinetics. Comparison between HGF and N,S-HGF confirmed the same key species in the reaction network, whilst the N,S-HGF catalyst accelerates LiPS conversion, leading to a faster depletion of LiPSs at higher potential to mitigate polysulfide shuttling effect and produce a larger output potential. These results highlight the catalytic approach as a promising strategy to tackle the fundamental challenges in Li-S batteries.

4.2 Experimental

4.2.1 Electrochemical Measurements

The synthesis N,S-HGF electrode was done as described in **Chapter 2**. The control sample HGF was synthesized by substituting the dopant sources with ascorbic acid, following the same procedures. The electrochemical performance of the catalysts including N,S-HGF and HGF was conducted in the CR2032 coin cells assembled in an argon-filled glovebox as demonstrated in

Chapter 3. CV curves were recorded in the voltage range of 1.6 V-2.8 V at a scanning rate of 0.05 mV s^{-1}.

4.2.2 *In situ* Raman Spectroscopy Measurements and Data Analysis

In situ Raman spectroscopy measurements were collected using a same setup as described in **Chapter 3**. The Raman cell was running with a discharge CV scan at 0.05 mV s^{-1} when Raman data were collected. Peak deconvolution and assignments for different polysulfide species in N,S-HGF and HGF Raman spectra under different voltages during discharge was done systematically using a homemade program for baseline subtraction and LabSpec for peak splitting.

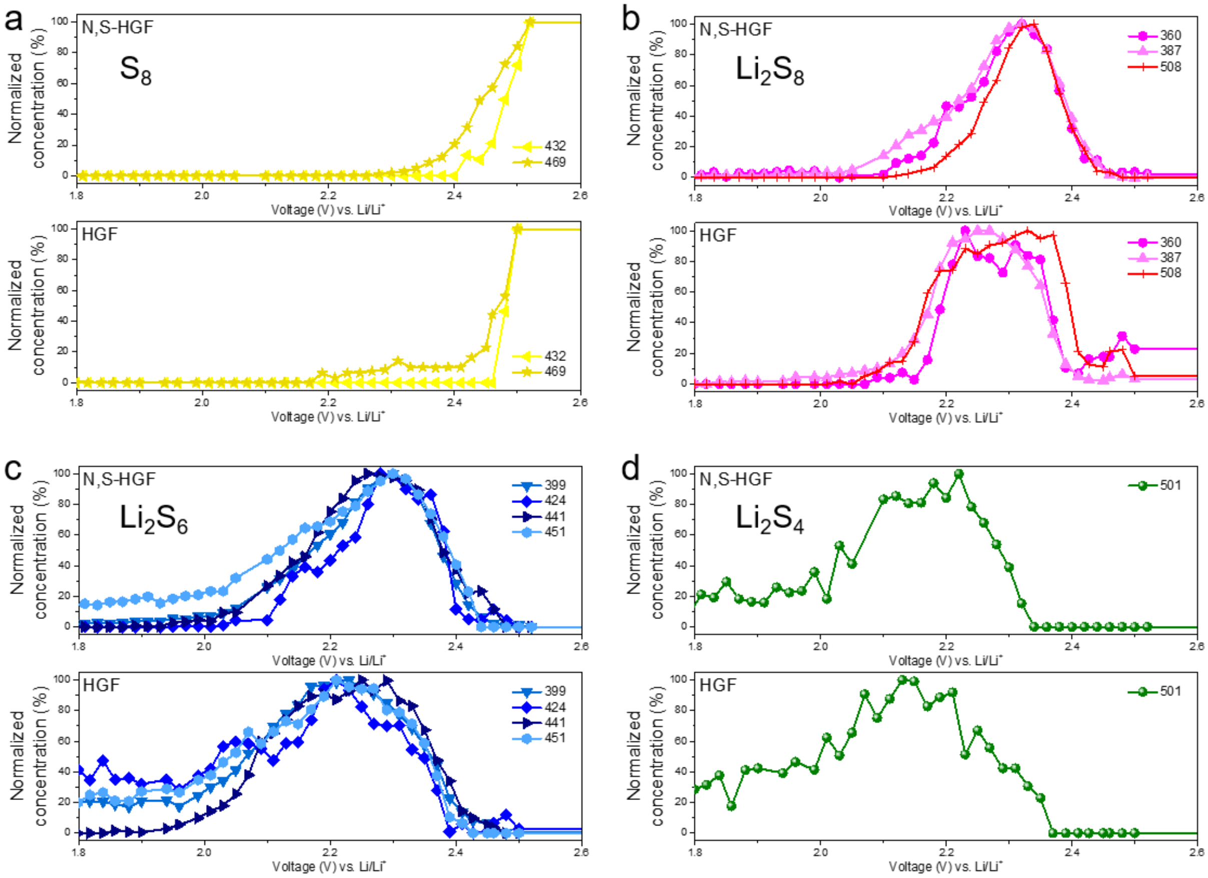

Figure 43. Raman peak assignments of S_8 and Li_2S_x (x=4, 6, 8) with different catalysts. Voltage dependent concentration curves for S_8 (**a**), Li_2S_8 (**b**), Li_2S_6 (**c**), Li_2S_4 (**d**) in N,S-HGF (top panel) and HGF (bottom panel) are derived from experimental *in situ* Raman spectra. Multiple peaks due to different vibrational modes are observed for each polysulfide species during peak fitting.

Numbers shown in the legends are peak positions in the unit of cm^{-1}. Each curve is normalized with respective to its highest peak area.

4.2.3 DFT Calculations

DFT calculations were performed using the Vienna ab initio simulation package[164]. The strongly constrained and appropriately normed (SCAN) functional[165] was used, as mentioned in **Chapter 3**.

4.3 Results and Discussion

4.3.1 Cyclic Voltammetry Results of Different Catalyst Systems for Sulfur Reduction Reaction

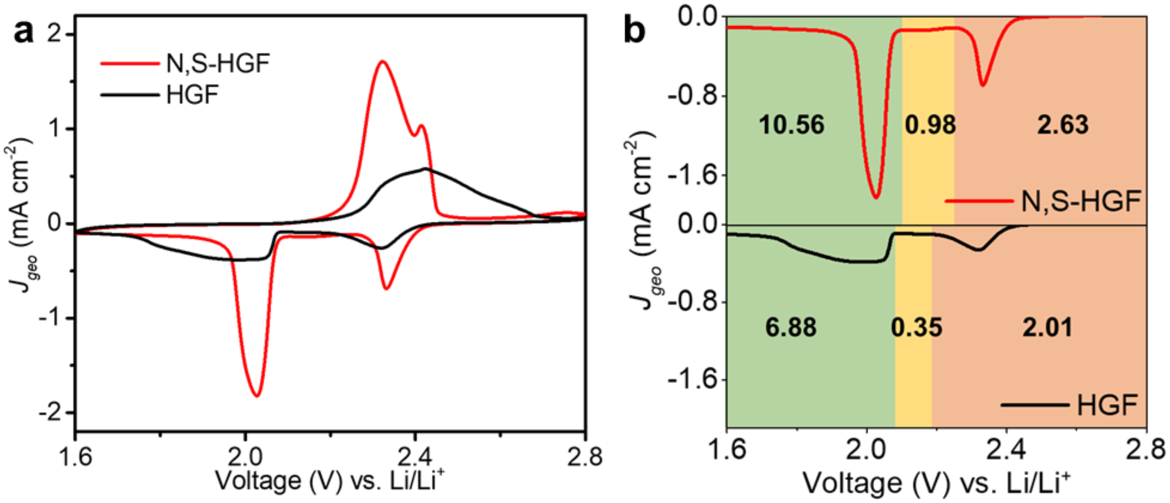

Figure 44. CV comparison between N,S-HGF and HGF. N,S-HGF shows better performance with higher capacity and smaller overpotential in Li-S battery.

Table 6. Charge number calculation results based on CV for N,S-HGF and HGF.

Voltage range (V) vs Li/Li$^+$	1.60~2.11	2.11~2.25	2.25~2.80	Total
Integrated area (N,S-HGF)	0.1979	0.0183	0.0494	0.2656
Charge number (C) (N,S-HGF)	1.979	0.183	0.494	2.656
Electron transfer number (N,S-HGF)	10.56	0.98	2.63	14.17

Formally electron transfer number in a full 16 e^- process (N,S-HGF)	11.92	1.10	2.98	16.00

Voltage range (V) vs Li/Li^+	1.60~2.09	2.09~2.16	2.16~2.80	Total
Integrated area (HGF)	0.1290	0.0065	0.0377	0.1732
Charge number (C) (HGF)	1.290	0.065	0.377	1.732
Electron transfer number (HGF)	6.88	0.35	2.01	9.24
Formally electron transfer number in a full 16 e^- process (HGF)	11.92	0.60	3.48	16.00

To better understand the influence of catalysts on the complex SRR network, we performed experiments by same approaches in **Chapter 3** with the non-doped HGF, as a less active catalytic system to compare with the N,S-HGF.

CV plot of HGF shows a similar shape as N,S-HGF (**Figure 44a**), with two main peaks separated by a non-zero plateau. Thus a similar reaction pathway can be expected for HGF system, $S_8 \rightarrow Li_2S_8 \rightarrow 2Li_2S_4\ (Li_2S_8 + Li_2S_4 \rightleftarrows 2Li_2S_6) \rightarrow 8Li_2S$, including the Li_2S_4 intermediate between two main steps and the nonelectrochemically generated Li_2S_6 resulting in the plateau region. Comparison of charge number calculation results based on CV between two samples (**Figure 44b** and **Table 6**) reveals that N,S-HGF exhibits superior performance, with higher capacity in all of the selected voltage ranges and smaller overpotential for SRR, especially when comparing the onset potentials for the second reduction peak on CV.

4.3.2 Raman Study for Polysulfide Evolution Behaviors with Different Catalysts

Similar to the N,S-HGF system, a systematic analysis of the peak area of the *in situ* Raman spectra at different discharge potentials (**Figure 45**) give the voltage dependent concentration profile for each polysulfide species in the HGF electrode. Overall, the HGF electrode shows a similar polysulfide evolution sequence Li_2S_8→Li_2S_6→Li_2S_4, but with different voltage range for each species.

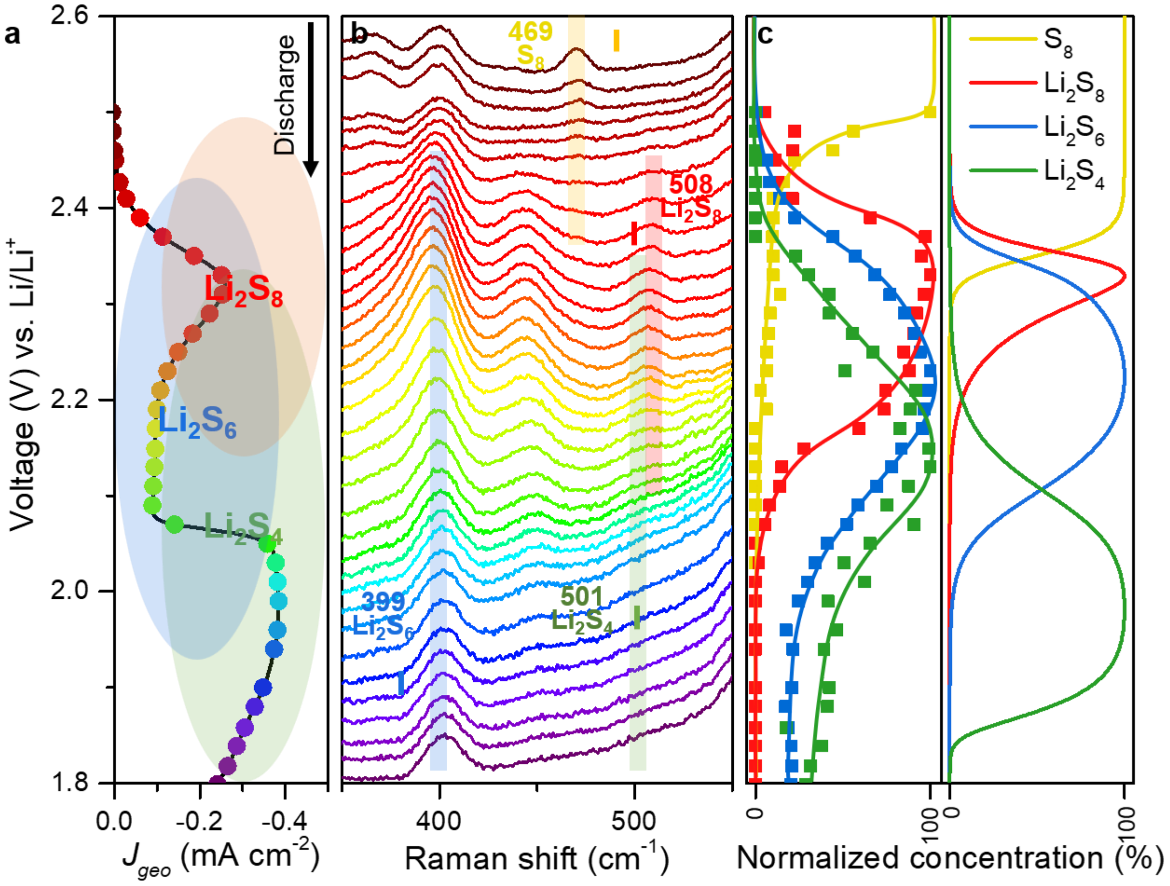

Figure 45. *In situ* Raman results during discharge with the non-doped holey graphene framework. **a, b,** The experimental *in situ* Raman spectra (**b**) of the non-doped holey graphene framework during discharge along with the CV results (**a**) where the same color indicates the same voltage. Characteristic peaks used to quantify the intermediates are marked with colored shades. Small labels with darker color indicate the computed frequency values. **c,** The comparison between potential dependent experimental concentrations (left panel) derived from *in situ* Raman spectra (**b**) and simulated concentrations from DFT (right panel). Each species is normalized with respective to its highest concentration.

The first step of discharge at high potential is weakly affected by the two different catalysts, the peak center for Li_2S_8 being slightly delayed in HGF (2.29 V) compared to N,S-HGF (2.32 V). Transformation of Li_2S_6 is more sensitive to different catalysts and seriously delayed in HGF, with an average peak value at 2.19 V (compared to 2.27 V in N,S-HGF), and with about 20% (relative to the peak concentration of Li_2S_6) remaining at 1.80 V in HGF (compared to less than 5% remaining at 1.80 V in N,S-HGF). A similar delay is seen for Li_2S_4, from higher overpotential in the later steps, with an average peak value at 2.12 V (compared to 2.14 V in N,S-HGF), and with more than 30% remaining at 1.80 V in HGF (compared to 17% remaining in N,S-HGF). The delayed depletion of Li_2S_4 and Li_2S_6 until a much lower potential with non-doped HGF electrodes implies a more sluggish conversion kinetics to lower order polysulfide, which could also lead to a more severe shuttling problem in the Li-S batteries.

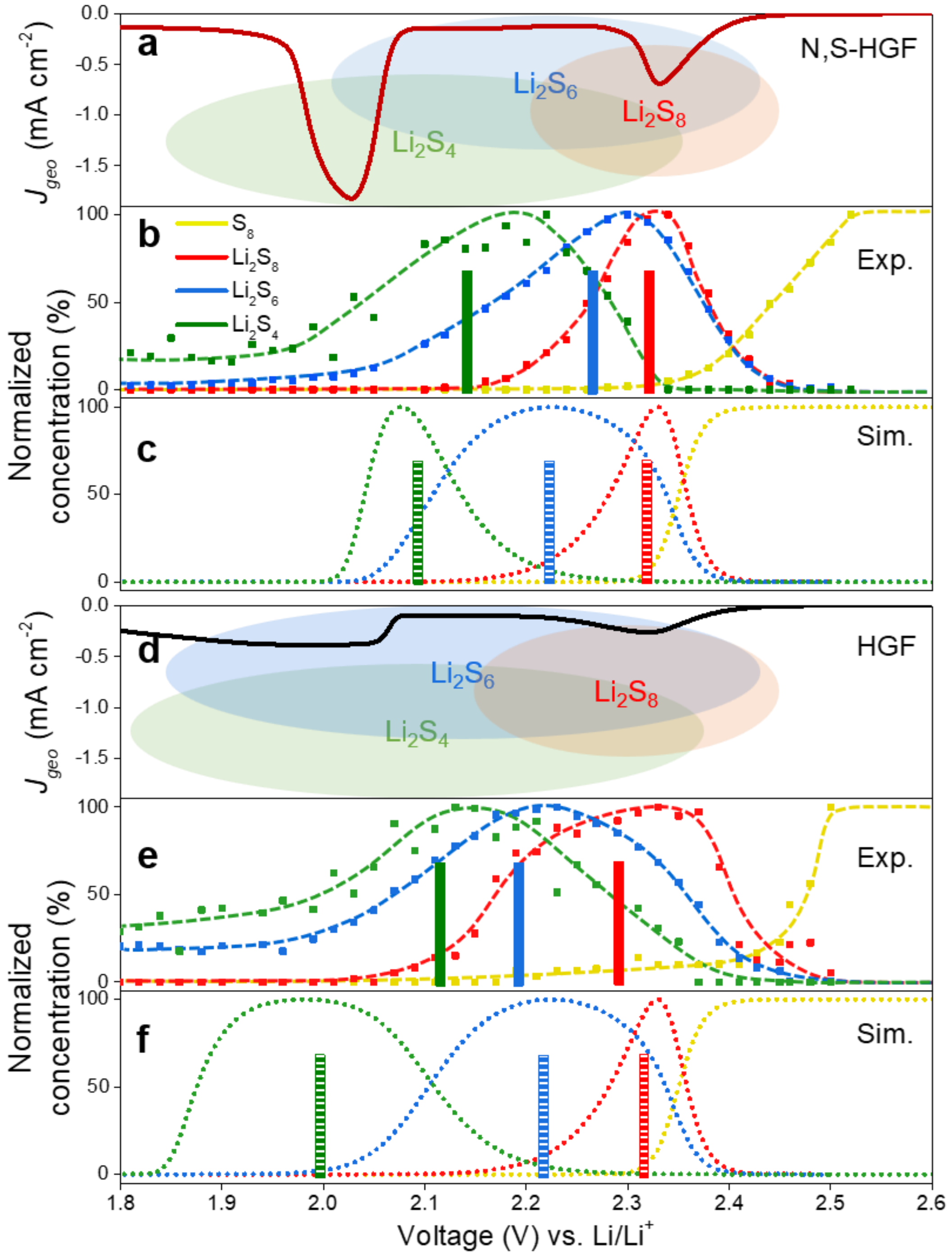

Figure 46. Comparison of different catalysts in sulfur reduction reaction. **a, d,** Experimental CV curves for N,S-HGF (**a**) and HGF (**d**). **b, e,** Voltage dependent concentration for each polysulfide species in N,S-HGF (**b**) and HGF (**e**) derived from experimental *in situ* Raman spectra. **c, f,** Simulated voltage dependent concentration for each polysulfide species in N,S-HGF (**c**) and HGF (**f**). Each species is normalized with respect to its highest concentration.

Table 7. Peak centers* for Li_2S_8, Li_2S_6, and Li_2S_4 on voltage dependent concentration curves for N,S-HGF and HGF.

Voltage (V) vs Li/Li^+	Li_2S_8	Li_2S_6	Li_2S_4
N,S-HGF (experimental)	2.32	2.27	2.14
N,S-HGF (simulated)	2.32	2.22	2.09
HGF (experimental)	2.29	2.19	2.12
HGF (simulated)	2.32	2.22	2.00

*Peak centers are determined by calculating the voltage where half of the whole peak area is obtained by integrating the voltage dependent concentration curve.

Our calculations described above indicate that there is no favorable path for direct electrochemical reduction of Li_2S_6 to lower order LiPSs in the potential regime above 1.89 V. Instead, it relies on the disproportionation reaction to convert Li_2S_6 to Li_2S_8 and Li_2S_4 for further reduction. However, the disproportionation reaction ($2Li_2S_6 \rightarrow Li_2S_8 + Li_2S_4$) is thermodynamically unfavorable and relies on the rapid depletion of Li_2S_4 to drive this reaction forward. In this case, a slower conversion kinetics of Li_2S_4 could seriously delay the conversion and reduction of Li_2S_6 until a much lower potential regime (<1.89 V), where a direct electrochemical reduction of Li_2S_6 may also start to occur. Overall, such slower conversion kinetics results in an accumulation of Li_2S_6 in a wider potential range, which could exacerbate the PS shuttling problem. This is also reflected by the reduced number of charge at high potential and within the overall SRR process: 2.36 and 9.24 electrons per S_8 molecule in HGF system, compared to 3.61 and 14.17 electrons in the N,S-HGF system (**Table 6**). These CV and *in situ* Raman studies revealed distinct SRR kinetics between HGF and N,S-HGF, which clearly highlights fundamental benefits brought by the efficient catalysts in Li-S batteries.

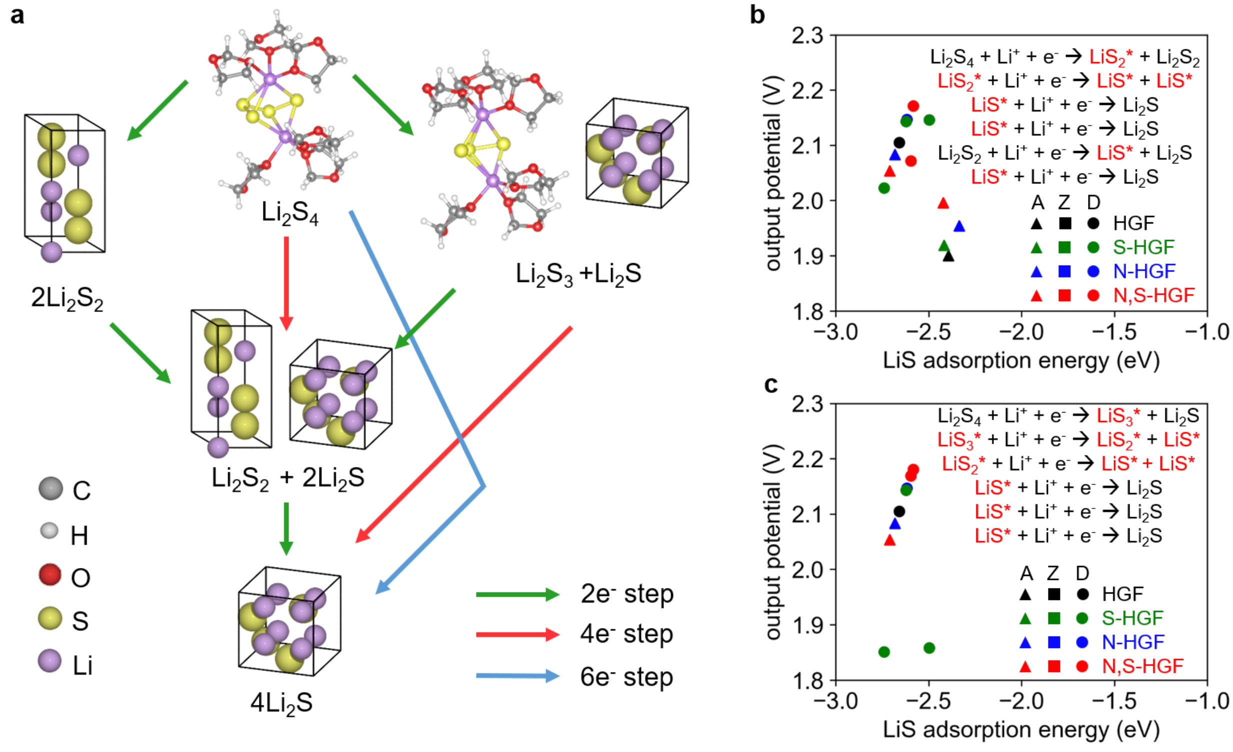

Figure 47. Simulated site-specific output potential of the Li_2S_4 to Li_2S conversion. **a,** Different possible combinations of $2e^-$, $4e^-$, and $6e^-$ steps considered for the second stage of sulfur reduction reaction, the conversion of Li_2S_4 to Li_2S**.** Green, red, and blue lines indicate $2e^-$, $4e^-$, and $6e^-$ steps, respectively. **b, c,** Simulated multistep output potential from Li_2S_4 to Li_2S for the two pathways with largest output potentials considering various active sites on different catalytic electrode models: armchair edge (A, triangles), zigzag edge models (Z, squares), and inner defect models (D, filled circles). Four types of dopants are considered: non-doped (black), S (green), N (blue) and N,S (red).

To understand the distinct potential range of these two systems, the conversion from Li_2S_4 to Li_2S is further investigated. Considering all the possible $2e^-$, $4e^-$, and $6e^-$ steps starting from Li_2S_4 (**Figure 47**), two pathways were found to give the largest output potential among the different catalytic sites: (1) one $4e^-$ step: $Li_2S_4+4Li^++4e^- \rightarrow Li_2S_2+2Li_2S$, followed by one $2e^-$ step: $Li_2S_2+2Li^++2e^- \rightarrow 2Li_2S$ (**Figure 47c**); (2) a pathway consisting of one $6e^-$ step, i.e., at least one radical species is adsorbed on the surface during the reduction process: $Li_2S_4+6Li^++6e^- \rightarrow 4Li_2S$ (**Figure 47d**). In both pathways, the largest output potential obtained by N,S-codoped sites, 2.18V, is larger than the largest output potential given by non-doped sites: 2.10 V, in line with the experimental results showing superior performance of N,S-HGF catalyst[70]. A smaller output potential in the second stage has far-reaching effects: the sluggish conversion of Li_2S_4 to lower order polysulfides could considerably retard the already thermodynamically unfavorable disproportionation reaction ($2Li_2S_6 \rightarrow Li_2S_8+Li_2S_4$) that is necessary for further reduction of Li_2S_6, thus leading to an undesirable accumulation of higher order LiPS species that can worsen the PS shuttling problem.

In line with the experimental results, the simulated potential dependent concentrations for the HGF electrode show more sluggish conversion, i.e., lower depletion potentials for Li_2S_4 and Li_2S_6 species, 1.85 V and 2.00 V in HGF vs. 2.00 V and 2.05 V in N,S-HGF system (**Figure 46**). The simulation of HGF and N,S-HGF effective output potential only differs significantly in the second stage, largely comparable to the experimental results. Such a close correlation between the experiments and theory further validates the catalytic strategy to tackle the PS shuttling in Li-S batteries. A better catalyst that can accelerate the polysulfide conversion can not only produce a larger output potential, but also significantly reduce the potential range in which the LiPSs could appear and effectively mitigate the PS shuttling effect.

4.4 Conclusion

Comparison between HGF and N,S-HGF confirms the same key species in the reaction network, whilst the optimized N,S-HGF catalytic electrode considerably accelerates the conversion of higher order LiPSs, leading to faster depletion of soluble LiPSs (Li_2S_6, Li_2S_4) at higher potential regime, hence mitigating the PS shuttling effect and boosting the output potential. It is interesting to note that our studies indicate that there is no favorable path for direct electrochemical reduction of Li_2S_6 to lower order LiPSs in the potential regime above 1.89 V. Instead, it relies on the disproportionation reaction ($2Li_2S_6 \rightarrow Li_2S_8+Li_2S_4$) to convert Li_2S_6 to Li_2S_8

and Li_2S_4 for further reduction, which is thermodynamically unfavorable and relies on the rapid depletion of Li_2S_4 to drive this reaction forward. In this case, a slower conversion kinetics of Li_2S_4 could seriously delay the conversion and reduction of Li_2S_6 until a much lower potential regime (<1.89 V). Overall, such slower conversion kinetics results in an accumulation of highly soluble Li_2S_6 in a wider potential range, which exacerbate the polysulfide shuttling problem.

These results unveil the critical role of catalysis in modifying the SRR kinetics and highlight the catalytic approach as a promising strategy to tackle the fundamental challenges in Li-S batteries. Insights achieved here can be applied to other systems beyond the heteroatom-doped HGF model system described in current study, including other potential SRR catalysts, such as single transition metal atom catalysts, metal oxides or metal sulfides. A central strategy is to search for the catalyst that reduces the overpotential, especially in the second stage.

CHAPTER 5: SULFUR REDUCTION ACTIVITIES OF DIFFERENT HETEROATOMS IN POROUS CARBON CATALYSTS

5.1 Introduction

Carbon materials containing nitrogen (N) heteroatoms have received significant attention as inexpensive and environmentally-benign materials for energy conversion and storage applications, such as electrodes[118], electrocatalysts[170,171], and catalyst supports[172]. These materials have recently been shown to exhibit high catalytic sulfur reduction activities in lithium sulfur (Li-S) batteries.[91] Achieving high-performing N-carbon catalysts requires a combination of material properties that include high electrical conductivities, low molecular diffusion resistances, and accessible and catalytically active surface moieties.[173] Mesoporous N-carbons with both high electrical conductivities (2.0 S cm) and high N contents (up to 28 wt%) have been reported,[174] however little is known about the atomic-level origins of their electrochemical properties. This has been due to their non-stoichiometric compositions, lack of long-range order, electrical conductivities, and complicated distributions of surface species,[175] which have made them challenging to characterize. Unraveling how the diverse nitrogen-containing moieties (e.g., pyrrolic,[176] pyridinic,[177] or graphitic[178]) account for the sulfur reduction reaction (SRR) activities is of great importance for future catalyst design in Li-S batteries.

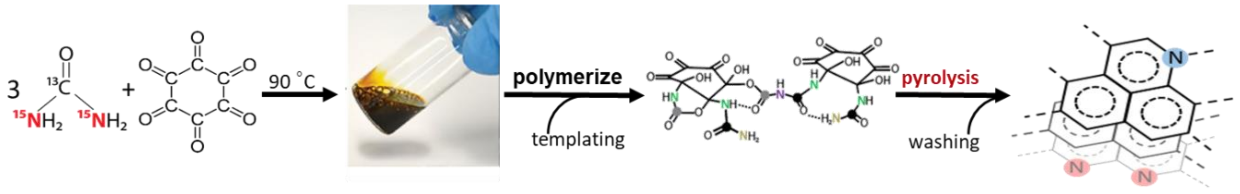

Figure 48. Synthesis of nitrogen-containing mesoporous carbon catalyst materials. The reactant mixture (cyclohexanehexone and urea) is combined at room temperature and heated to 363 K under air to form a eutectic melt. The mesoporous templating agent (SBA-15 mesoporous silica or $ZnCl_2$-NaCl salt mixture) is then combined with the eutectic melt and subsequently pyrolyzed in a nitrogen atmosphere at 1073 K to form the mesoporous N-containing carbon materials.

Mesoporous N-carbons can be prepared through high-temperature (1073 K) pyrolysis in the presence of a mesopore templating agent, such as $ZnCl_2$-NaCl salts or SBA-15 silica. These two templating agents yield N-carbon materials with similar mesopore dimensions (3-4 nm diameter) but different surface areas (1100 $m^2\ g^{-1}$ for silica-templated N-carbon, and 1800 $m^2\ g^{-1}$ for salt-templated N-carbon). X-ray photoelectron spectroscopy (XPS) established that the salt- or silica-templated mesoporous N-carbons have near-surface N contents of 16 mol% and 22 mol%, respectively.

Here, we evaluated and analyzed the macroscopic sulfur reduction properties of these two high N-content mesoporous carbon catalysts by cyclic voltammetry (CV). In combination with the distributions of surface compositions and structures obtained from solid-state 2D nuclear magnetic resonance (NMR) spectroscopy and density functional theory (DFT) calculations, distinct types of N moieties were distinguished and correlated to the SRR activities, among which surface pyridinic species are determined to be the most important active sites for sulfur reduction.

5.2 Experimental

The electrolyte (referred to as "blank electrolyte") was made by combining 1 M lithium bis(trifluoromethane-sulfonyl) imide (Sigma-Aldrich) and 0.2 M lithium nitrate (Sigma-Aldrich) in a mixed dimethoxyethane (Sigma-Aldrich) and 1,3-dioxolane (Sigma-Aldrich) solution (1:1 by volume). The Li_2S_6 catholyte (0.1 M) was prepared by reacting sublimed sulfur (Sigma-Aldrich) with Li_2S (Sigma-Aldrich) in stoichiometric proportions in the blank electrolyte. The mixture was vigorously stirred at 50 °C in an argon-filled glove box overnight to produce a brownish-red Li_2S_6 catholyte solution. Sulfur-reduction performance was evaluated by conducting CV measurements of the mesoporous nitrogen-containing carbon materials in CR2032 coin cells that were assembled in an argon-filled glovebox. The cathode slurry was prepared by mixing nitrogen-carbon or graphite, carbon black, and polyvinylidene fluoride binder at a mass ratio of 8:1:1 in N-methyl-2-pyrrolidone. The slurry mixture was drop cast onto a carbon-coated aluminum foil with a diameter of 1.3 cm. The loading of the nitrogen-carbon material was 1 mg cm^{-2}. Afterwards, the Li_2S_6 catholyte was used as a sulfur source and drop-cast on the cathode. The mass loading of the sulfur was 0.15 mg cm^{-2} to ensure maximum utilization of sulfur. The sulfur cathodes were then directly assembled into a CR2032 coin cell with lithium foil, a Celgard 2500 separator, and blank electrolyte. CV curves were recorded over the voltage range of 1.7 V-2.7 V at a scanning rate of 0.1 mV s^{-1}.

5.3 Results and Discussion

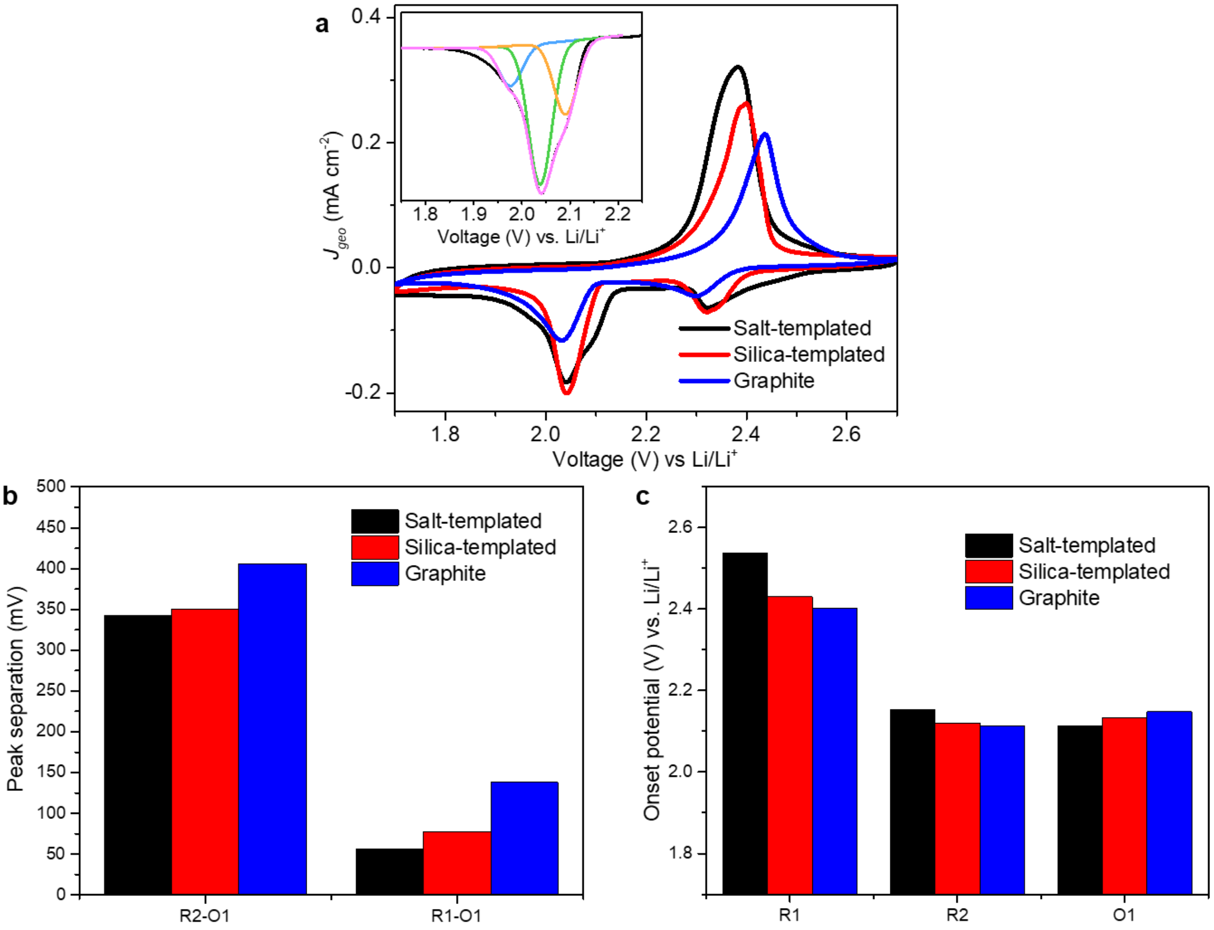

Figure 49. Catalytic sulfur reduction activities of mesoporous N-carbons by using silica (red) or $ZnCl_2$-NaCl salt (black) as templating agents. **a,** The sulfur reduction reaction CVs are compared to a standard graphitic carbon (blue), with the various oxidation (O_1) and reduction (R_1, R_2) peaks; deconvoluted R_2 peak(s) observed for the salt-templated N-carbon are shown in the upper left inset. Currents were normalized by the geometric electrode area. **b,** Peak separations between R_2-O_1 and R_1-O_1. **c,** Onset potentials for O_1, R_1, and R_2 peaks

Two mesoporous N-carbon materials prepared through high-temperature pyrolysis were assembled into coin cell to evaluate their sulfur reduction activities for Li-S batteries. **Figure 49a** shows CV curves in coin cells for these salt- (black) and silica-templated (red) N-carbons, compared to a standard graphitic carbon (blue). The peak separation between oxidation and reduction pairs and onset potentials for each peak were calculated and compared in **Figure 49b and c**.

For oxidation process, a smaller onset potential indicates an earlier beginning of oxidation, i.e., smaller overpotential. The oxidation peak of the salt-templated N-carbon is at 2.38 V, a lower potential than either the silica-templated N-carbon (2.40 V) or the graphitic carbon (2.44 V), indicating an earlier oxidation. Similarly, for the reduction peaks, higher onset potentials indicate lower overpotential, and the two reduction peaks R_1 and R_2 are correlated with the reduction of S_8 into polysulfide intermediates and of polysulfides into Li_2S_2/Li_2S, respectively. The salt-templated N-carbons exhibits a higher R_1 onset potential (2.54 V) than either the silica-templated N-carbon (2.42 V) or the graphitic carbon (2.40 V). The salt-templated N-carbon displays the highest potential, with a first partially resolved R_2 reduction peak at 2.09 V, followed by additional partially resolved reductive peaks at 2.04 V and 1.98 V (**Figure 49a, inset**), suggesting the presence of multiple reduction sites or mechanisms. The silica-templated N-carbon and the graphitic carbon both exhibit a single R_2 peak at 2.04 V and 2.03 V, respectively, suggesting that there may be only one major active site or reduction mechanism responsible for these signals in both types of templated materials. Overall, a smaller peak separation between oxidation and reduction peaks signifies a lower barrier for kinetics, and is expected in good catalysts. The salt-templated N-carbon exhibits the smallest peak separation distances between R_1-O_1 and R_2-O_1 (**Figure 49b**), which manifests faster sulfur reduction kinetics, and higher peak intensities that indicate more efficient utilization of sulfur species in the electrodes. The superior reduction activity of the salt-templated N-carbon suggests that it has a different and more catalytically effective distribution of surface N-carbon moieties, compared to the silica-templated material.

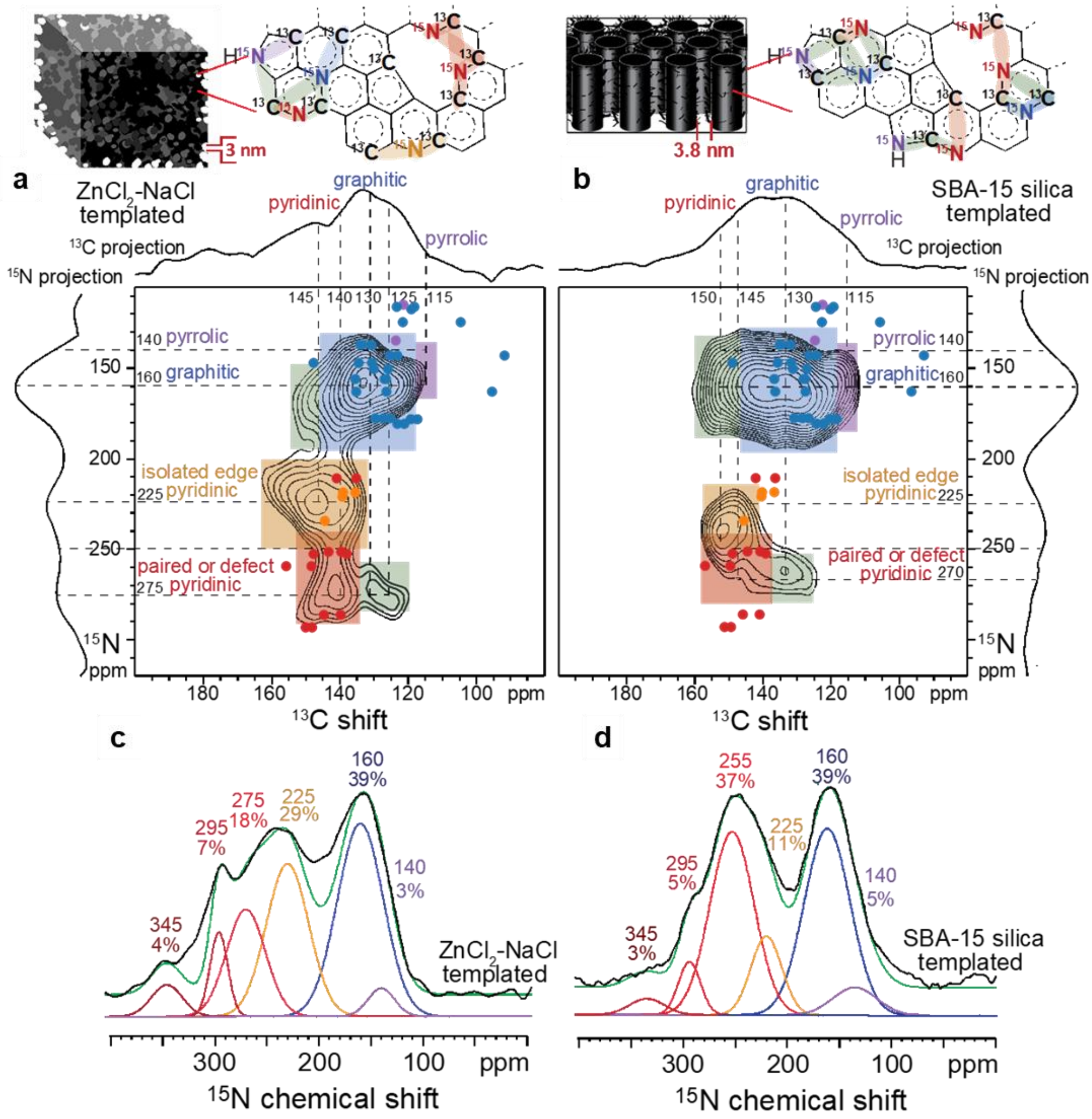

Figure 50. Resolving and quantifying ^{15}N species in high-N-content mesoporous carbons. Solid-state 2D ^{13}C-^{15}N HMQC NMR correlation spectra acquired at 9.4 T, 95 K, and 8 kHz MAS of **(a)** ZnCl$_2$-NaCl salt-templated and **(b)** SBA-15 silica-templated mesoporous N-carbons, showing their significantly different distributions of N-carbon moieties. The 2D spectra were acquired with recoupling times of 0.6 ms, which probes dipole-dipole-coupled ^{13}C-^{15}N moieties within distances of approximately 0.4 nm. The colored points represent calculated ^{13}C and ^{15}N shieldings from DFT for nuclei in N-carbon moieties and their local environments up to three bond distances, as described in the text. 1D ^{13}C and ^{15}N projections are shown along the horizontal and vertical axes, respectively. The purple, blue, yellow, and red shaded regions indicate correlated signals arising, respectively, from pyrrolic, graphitic, isolated edge pyridinic, and paired or defect pyridinic moieties present in the high-N-content mesoporous carbons, as depicted in the schematic diagrams above the 2D spectra. The green shaded regions indicate correlated signals arising from nearby or commingled N-containing moieties. Quantitative 1D single-pulse ^{15}N MAS NMR spectra of the

same **(c)** salt- and **(d)** silica-templated materials as in **(a)** and **(b)** and acquired under the same conditions. Signal positions and linewidths determined by the 2D spectra were used to deconvolve, fit, and quantify the integrated signal intensities of the 1D spectra.

The atomic sulfur reduction properties of different surface N-carbon moieties are further correlated to 2D NMR characterization and analysis results. The distributions and fractions of at least four different types of ^{15}N-^{13}C environments were deciphered from 2D NMR: graphitic, pyrrolic, isolated edge pyridinic and paired or defect pyridinic. The quantitative 1D direct-excitation ^{15}N MAS NMR spectra (**Figure 50 c,d**) can be deconvolved to establish the relative populations of the different N moieties. Whereas the two N-carbons have similar relative fractions of graphitic (39%), pyridinic (56%), and pyrrolic (5%) environments, they exhibit significantly different relative quantities of isolated edge and paired/defect pyridinic moieties. Notably, the salt-templated N-carbon exhibits significantly stronger correlated signal intensity associated with isolated edge pyridinic moieties (**Figure 50a**, yellow) than the silica-templated N-carbon (**Figure 50b**) (29% vs. 11%), indicating that they are more prevalent in the salt-templated N-carbon. In addition, the silica-templated N-carbon shows strong resolved ^{15}N intensity (**Figure 50a**, red) that corresponds to paired or defect pyridinic species, which are unresolved in the salt-templated N-carbon.

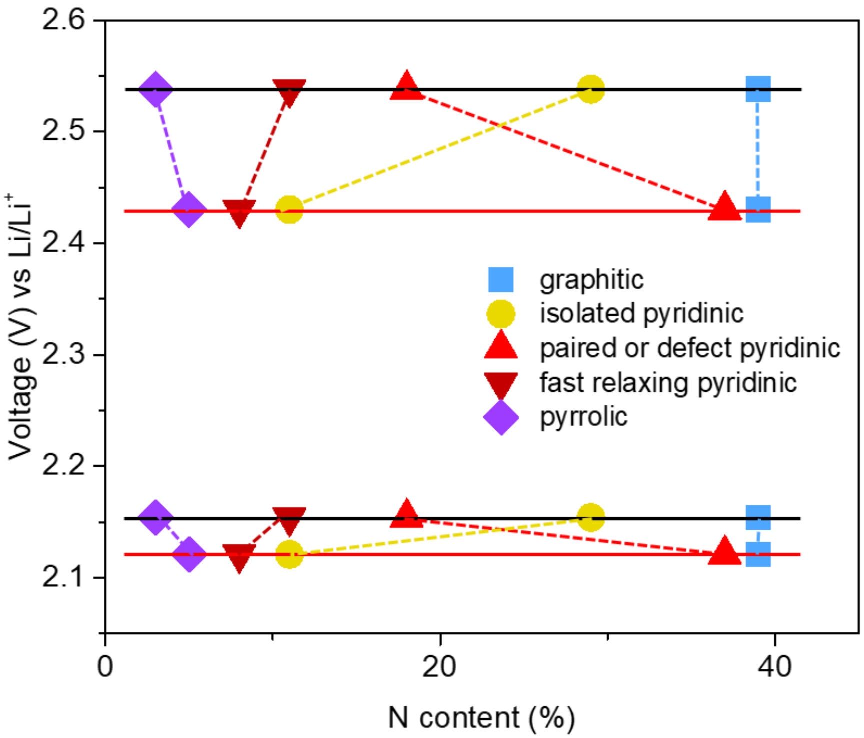

Figure 51. Onset potentials of R_1 and R_2 for the mesoporous salt- and silica-templated N-carbon materials (black and red lines, respectively) plotted versus fractional N contents of each type of N-carbon moiety determined from the quantitative 1D ^{15}N NMR spectra.

Figure 51 shows the correlation of the sulfur reduction activities represented by the onset potentials with nitrogen contents of each type of N-carbon moiety. The pyrrolic N contents (purple), the graphitic N contents (blue), and the fast-relaxing pyridinic ^{15}N moieties (dark red) are approximately the same in the differently templated materials and therefore cannot account for the higher onset reduction potentials of the salt-templated N-carbon material. By comparison, much higher percentages of isolated pyridinic N moieties (yellow) and significantly lower percentage of paired or defect pyridinic N moieties (red) in the salt-templated N-carbon manifest the importance of these pyridinic N moieties on SRR properties. The isolated pyridinic N moieties could be particularly crucial for certain kind of catalytic activities for sulfur reduction. The different surface compositions arise from interactions of nitrogenous carbon moieties as they form during pyrolysis with the different template surfaces. This atomic level analysis for the catalytic activities of different N environments provides thoughtful perspectives for next generation catalyst design.

5.4 Conclusion

Two mesoporous carbon materials synthesized by different templates during pyrolysis were validated to exhibit different sulfur reduction activities. Differences in the macroscopic sulfur reduction properties of the salt- and silica-templated N-carbons are accounted for by clear differences in the distributions of N heteroatoms among different moieties, especially surface pyridinic sites. Specifically, isolated edge pyridinic N moieties are shown to be present in higher fractional quantities and at accessible mesopore surface sites in the salt-templated mesoporous N-carbon, compared to the silica-templated analog, and likely account for the differences in their macroscopic reduction activities. This manifests the important role of the mesoscale porosity of N-carbon catalysts, which presents opportunities for optimizing macroscopic sulfur reduction properties. The new atomic-level insights into the types of N-carbon moieties that are important in sulfur reduction catalysts are expected to aid the development of non-precious-metal catalysts and provide criteria for the rational design of novel heteroatom-containing carbon materials.

CHAPTER 6: 2D MATERIAL FUNCTIONALIZED SEPARATOR FOR ROOM TEMPERATURE SODIUM SULFUR BATTERIES

6.1 Introduction

The limitation of lithium resources and high cost impedes the large-scale applications of lithium sulfur (Li-S) batteries, albeit given their high capacity, environmental benignity, and low cost of sulfur. The abundant and cheaper sodium (Na), with analogous chemical properties, offers an attractive alternative with sodium sulfur (Na-S) batteries, with a theoretical capacity of 1672 mAh g_s^{-1}.[102] Na-S batteries have been realized at high temperature (>300 °C) and commercialized in utility scale stationary power applications, but only achieved partial reduction of S into Na_2S_n ($n \geq 3$) and a theoretical energy density <557 mAh g_s^{-1}. In addition, the high temperature operation is costly, consumes additional power and causes safety concerns.[100] Thus, there is considerable motivation to develop room-temperature (RT) Na-S batteries.

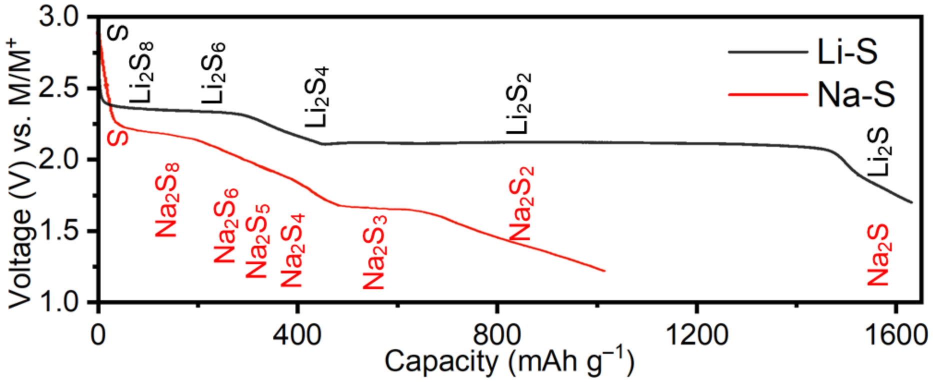

Figure 52. Comparison of galvanostatic discharge curves of typical Li-S and Na-S batteries.[179]

However, the slower ion transport process and more sluggish sulfur reduction reaction (SRR) kinetics associated with larger Na^+ has been the key hurdle to realizing RT Na-S batteries (**Fig. 52**). For example, Na-S discharging curve display a much higher overpotential than Li-S system. Additionally, liquid-solid transition in Na-S begins earlier from soluble Na_2S_4 to insoluble

Na_2S_3 (compared to the Li_2S_4 to Li_2S_2 in Li-S), resulting in a slower kinetics and less complete conversion from polysulfides to sulfides. In another aspect, sodium is more reactive to the electrolyte than lithium in Li-S battery, and similar to lithium polysulfides, sodium polysulfides exhibit high solubility in ether electrolyte, hence it is easier for sodium polysulfides to be reduced and deposited on sodium metal.[179] Overall, the more complex and less efficient SRR leads to faster accumulation of polysulfides in the cell during sulfur reduction and further causes polysulfides loss in sodium anode in the cell, which represents one of the most critical challenges for RT Na-S batteries.

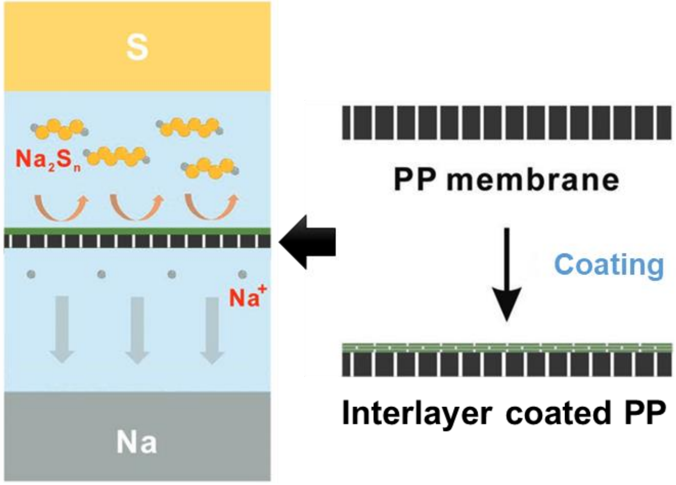

Figure 53. Separator coating design for Na-S battery in this work.

Physical intercepts between cathode and anode offer an effective strategy to combat the shuttling problem in Na-S batteries. Various materials have been reported to exhibit excellent ability to block polysulfides and compromise shuttling in Na-S batteries.[180-182] In view of the fact that graphene oxides have a lot of oxygen-containing functional groups on the edge of the carbon plane, which can provide a massive, negative-charged electron cloud to repulse the polysulfides' negative charges and trap them in the sulfur cathode side. Therefore, it is supposed to be capable of reducing the amount of active sulfur lost and increase the cell's capacity and Coulombic efficiency.

In this work, by methodically developing various coating processes and efficient 2D materials, we investigated how decorated separator may assist solve the sulfur loss in Na-S batteries to raise the Coulombic efficiency and improve the capacity. N,S-HGF was selected again as an modeling sulfur host in cathode. The greatest increase in CE and capacity was shown in a coated separator made by vacuum filtration from a mixture of holey graphene oxide (HGO) and MXene. The composition and thickness of the coating could be further adjusted and the design will be tremendously insightful for the separator design to help Na-S batteries become a competitive energy storage technology.

6.2 Experimental

6.2.1 Separator Coating

Two methods were explored to coat the selected 2D materials on the polypropylene (PP) separator.

Vacuum filtration: the active material was exfoliated and dispersed in an appropriate solvent and sonicated to form a uniform suspension, and then filtered through a commercial Celgard 2500 PP separator by vacuum filtration. After drying at 70 °C overnight in an air oven, the dried coated separator was cut into circular disks with a diameter of 19 mm. The mass loading of the active material can be controlled to 0.002~0.09 mg cm^{-2}.

Slurry coating: the active material and PVDF was mixed by a ratio of 9:1 in an NMP solution to form a well-mixed active material slurry, and then cast onto a commercial Celgard 2500 PP separator, and a doctor’s blade was used to coat the surface evenly. The coated separator was then dried in an air oven at 50 °C overnight. The dried coated separator was then cut into circular disks with a diameter of 19 mm. The mass loading of the active material is about 0.07~0.28 mg cm^{-2}.

6.2.2 Electrochemical Measurements

The N,S-HGF was synthesized as described in **Chapter 2** and used as the host for sulfur. The electrochemical performance was conducted in the CR2032 coin cells assembled in an argon-filled glovebox. The electrode was prepared by directly pressing the aerogel into a freestanding thin film. Afterwards, the 0.1 M Na_2S_6 catholyte (prepared in a similar way as Li_2S_6 catholyte described in **Chapter 2**) was directly used as sulfur source to drop cast in the electrode. The mass ratio of the sulfur in the cathodes was set as 33%. The sulfur cathodes were then directly assembled into a CR2032 coin cell with sodium foil, coated PP separator and blank electrolyte. Galvanostatic charge discharge cycling were recorded in the voltage range of 1.2 V-2.8 V at 0.05 C for the first 30 cycles and 0.1 C in the following cycles.

6.3 Results and Discussion

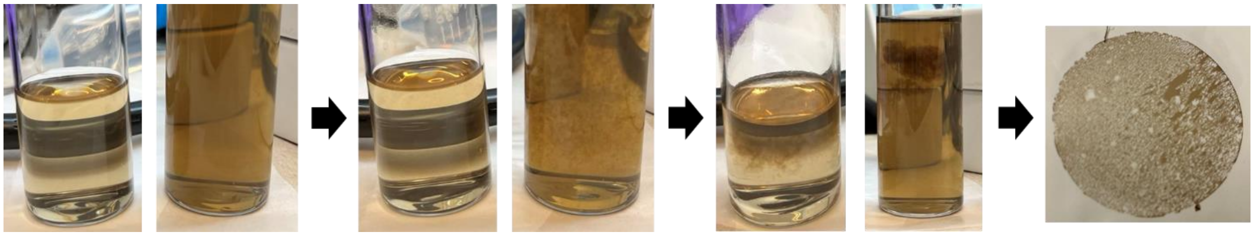

Figure 54. Photos show bad dispersion of HGO in pure acetone. A uniform dispersion was obtained after sonication. However, flocculation happens immediately after shaking, leading to an ununiformed covering on separator after filtering.

Vacuum filtration is a common way for separator modification.[183] Since the PP separator is extremely hydrophobic, the appropriate solvent for filtration was first investigated. An ideal solvent for a successful filtration must be able to easily pass through the separator as well as effectively disperse the 2D nanosheets. An effective dispersion ought to last long enough to finish the filtration. We have thoroughly examined multiple common solvents include water, ethanol, acetone, isopropyl alcohol, dimethylformamide, acetonitrile, etc. Each solvent exhibits either good dispersion but slow filtering or quick filtering but poor dispersion. Acetone/water mixture (v:v 3:1) was finally discovered to possess both advantages, additionally it is clean and easy to evaporate, and was therefore chosen as the solvent for the subsequent filtration.

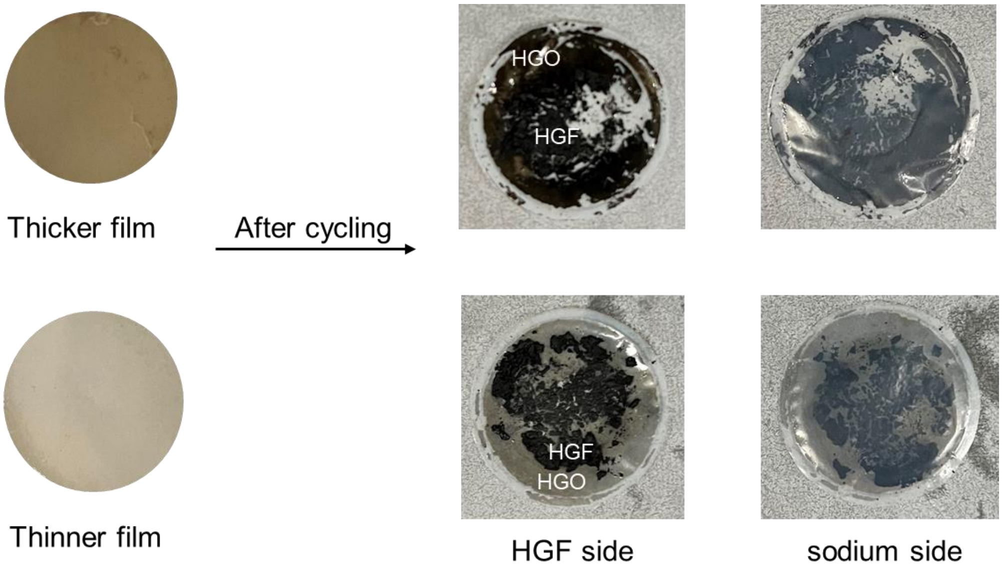

Figure 55. Thickness study of the coating. Thicker film (0.088 mg cm^{-2}) exhibits severe cracks after cycling, while the thinner one (0.035 mg cm^{-2}) is still in a complete manner after cycling.

The film's thickness is crucial to the coating's elasticity. According to **Figure 55**, the thinner film (0.035 mg cm^{-2}) is still in a complete state after cycling while the thicker one (0.088 mg cm^{-2}) displays serious cracks. This could be explained by the poor mechanical property that results from overlapping too many layers of 2D sheets, therefore a suitable thickness is required to increase the coating's durability. The best loading was chosen after testing various loadings for each 2D material in the following results displayed in **Figure 56**.

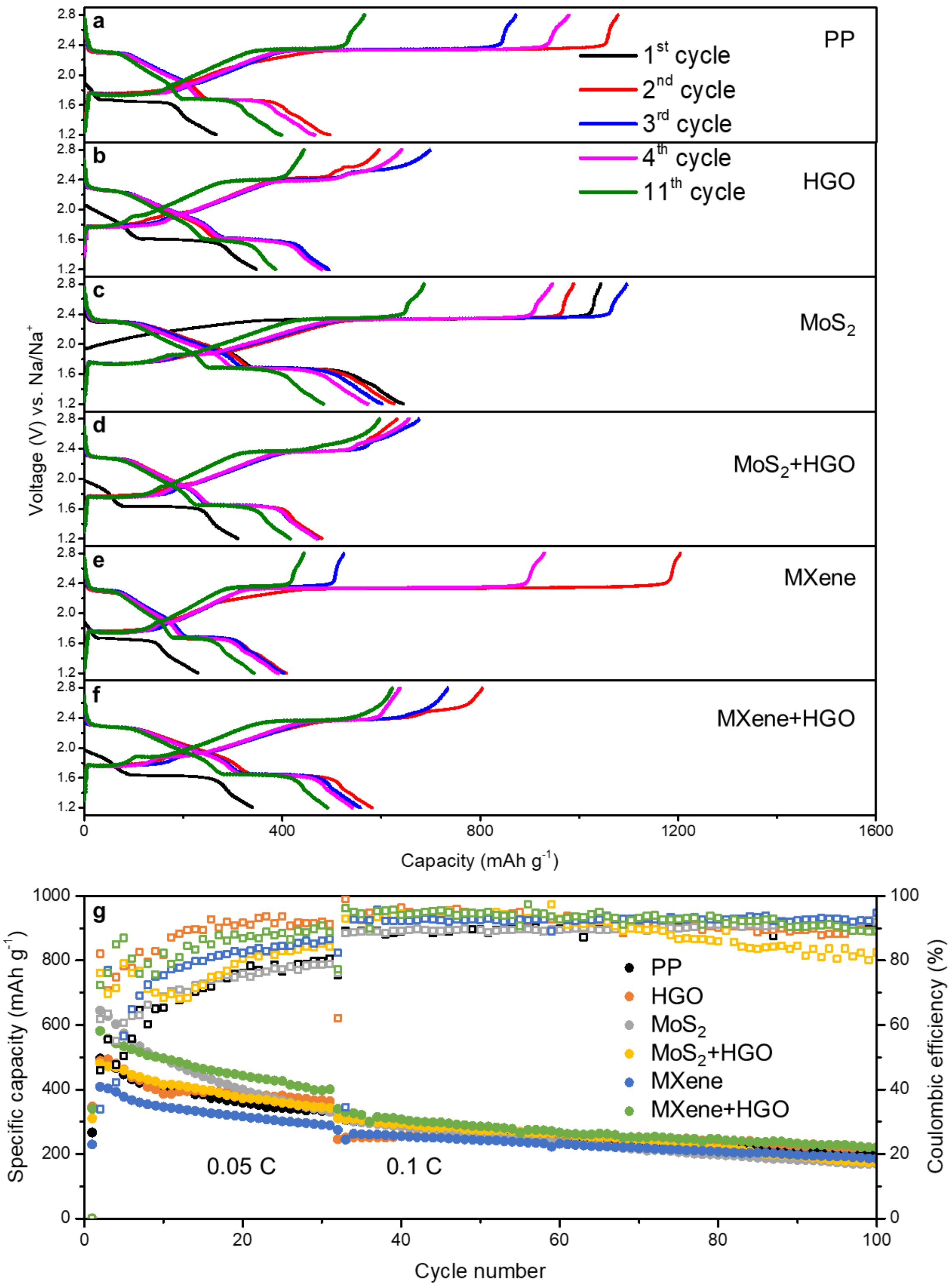

Figure 56. Cell performance with separators coated with different 2D materials made by vacuum filtration. **(a-f)** show the galvanostatic charge discharge profiles of 1-4 and 11th cycles for each

material. **(g)** shows the stability tests of 100 cycles with 0.05 C in the first 30 cycles and 0.1 C in the following cycles.

Figure 56 compares the performance of cells with separators coated in various 2D materials. Blank PP causes severe shuttling, a noticeable overcharge, and rapid capacity depletion. The CE has been dramatically raised (from 50% to 85% with HGO/MXene mixture, for example) after the addition of several 2D materials or their mixtures into the coating layer. HGO exhibits the strongest influence and highest CE among all the 2D materials. It also benefits other materials when combined with them, and that may be a result of its abundant oxygen-containing functional groups on the surface, which provide negative charge to repel negatively charged polysulfides back to the sulfur cathodes and thus reduce shuttling between two electrodes.

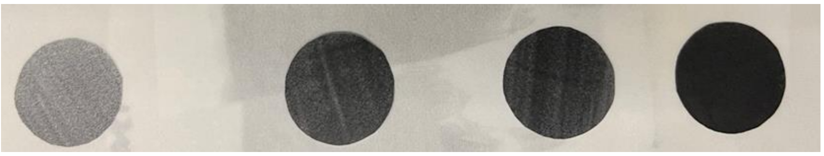

Figure 57. Photos of coated N,S-HGF layer on separator via slurry coating, with thickness of 30 μm, 60 μm, 90 μm and 120 μm, from left to right.

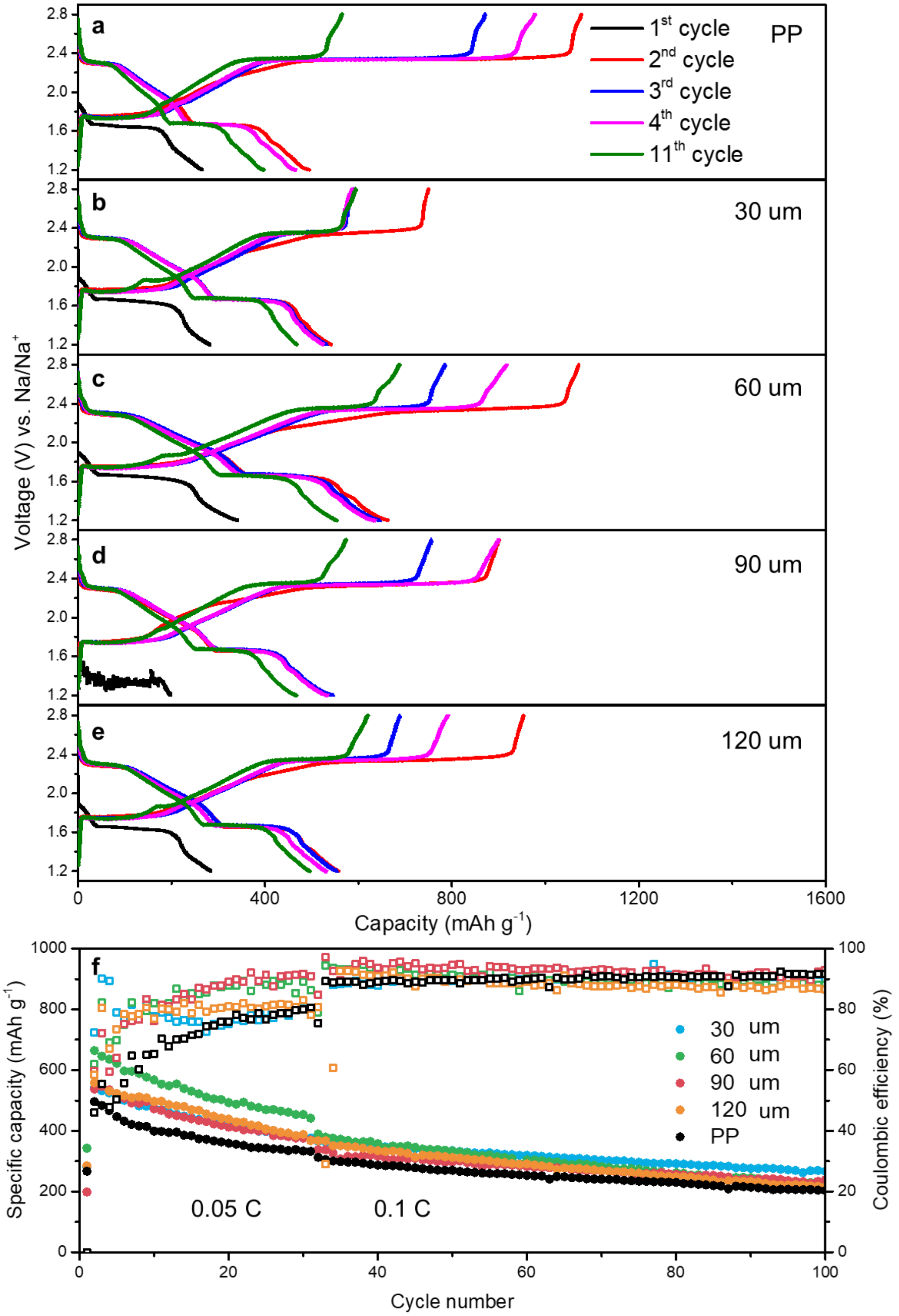

Figure 58. Cell performance with separators with N,S-HGF coating in different thicknesses made by slurry coating. **(a-e)** show the galvanostatic charge discharge profiles of 1-4 and 11th cycles for

each material. **(f)** shows the stability tests of 100 cycles with 0.05 C in the first 30 cycles and 0.1 C in the following cycles.

The most typical method for battery electrode preparation is slurry coating. Using the same method, the active ingredients were coated onto the PP separator. Slurry coating was developed for a wider range of materials since substances like HGF cannot form a stable suspension in acetone/water to perform the filtration. N,S-HGF was selected and coated onto the separator, serving as both a physical barrier and a potential catalyst. Numerous active catalytic sites, such as N, S doped sites, are present in N, S-HGF and may have a catalytic impact when in contact with polysulfides, further jeopardizing the shuttling process. The N,S-HGF film darkens and more completely covers the separator as the coating layer thickness increases (**Figure 57**). The Na-S cell performance with N,S-HGF in different thicknesses was compared with the blank PP by galvanostatic charge discharge measurements and shown in **Figure 58**. PP coated with 60 μm N,S-HGF shows a higher capacity up to 650 mAh g^{-1} under 0.05 C, and excellent stability under 0.1 C. This further demonstrates the superior cycling durability of a thinner, more flexible film, which may be due to their capability to suppress sulfur volume change. Although it appears to have the most effective covering in **Figure 57**, 120 μm turns out to be too thick for a flexible film.

Figure 59 compares the two coating techniques, and the slurry coating exhibits superior performance in terms of capacity and stability (if comparing the degradation from 4th to 11th cycle). This can be attributed to the slurry coating's improved film quality, something that might also be correlated to the PVDF addition, which can aid to strengthen the coating's integrity when it is squeezed by sulfur/lithium electrodes in the coin cell. In general, slurry coating is confirmed to be a better technique for creating coated separators to address the shuttling issue in Na-S batteries due to its wide range of material options and higher film quality. Thereupon, abundant 2D materials can be tested using this coating technique to determine the best interlayer composition for obstructing sodium polysulfides.

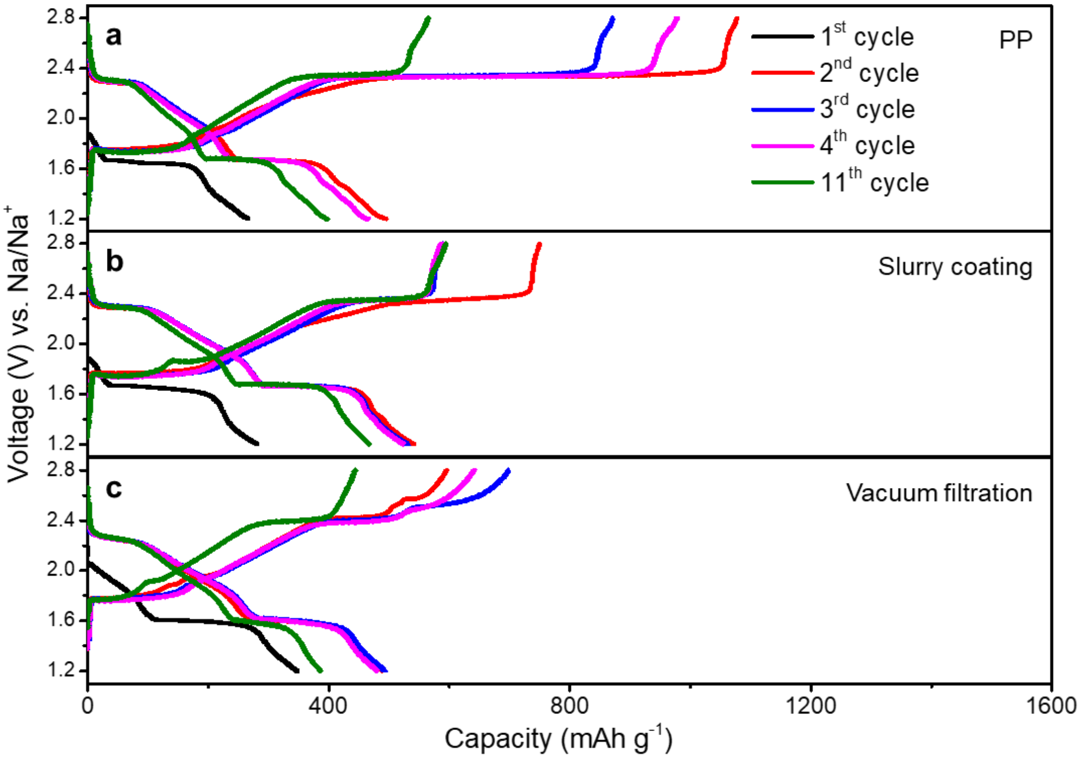

Figure 59. Comparison of modified separators with the same loading of HGO on PP by two coating methods. **a,** Blank control PP sample. **b,** Coated PP by slurry coating. **c,** Coated PP by vacuum filtration.

6.4 Conclusion

The serious shuttling issue with Na-S batteries, which has not yet been satisfactorily overcome, has recently drawn increasing attention from the battery technology. The shuttling threat in Na-S batteries operating at room temperature was addressed here by designing some 2D material coated separator to capture polysulfides in the cathode side. We first screened various 2D materials that could be used in separator modification. Due to its surface's negative charges, which have a substantial repulsion to polysulfides, HGO outperforms all other 2D materials examined here in terms of locking down polysulfides. A potentially effective combination for the interlayer on separator of Na-S batteries is HGO and MXene. Along with that, two distinct coating techniques were developed. Slurry coating creates coated films more effectively than vacuum filtration, with flexible 2D nanosheets overlapped sufficiently to block the polysulfides, resulting in increased capacity and longer stability. Slurry coating is also appropriate for a broad range of materials, such as catalyst-modified nanosheets that, when used in Na-S cells, have the additional effect of accelerating polysulfide conversion. These preliminary findings will be useful in the future as we create more effective interlayers for Na-S battery designs to confront the shuttling challenges.

CHAPTER 7: CONCLUSION

For energy storage applications to be employed in high performance portable devices and electric vehicles, it is essential to develop advanced next generation high energy density batteries. Due to their high energy density and inexpensive price, metal sulfur batteries are a direction that shows incredible promise. In order to attain higher productivity while performing rational design in the future study, we first carried out some basic mechanism investigation on Li-S batteries to thoroughly grasp the reaction pathway and electrode behavior during cycling. In **Chapter 2**, we focused on exploring how passivation layers is generated Li-S batteries and how the voltage window affects this process. The mechanism of sulfur oxidation reaction and shuttling was investigated using charge number analysis on CV plots. It has been established that $LiNO_3$ is an essential additive for Li-S batteries, however it serves as a double edged sword on the cathode and the anode. Then, in **Chapter 3**, we applied CV analysis to the sulfur reduction reaction after learning the basic concepts and empirical critical testing parameters from the previous chapter. We constructed and validated a proposed molecular reaction network for the sulfur reduction reaction, which was further validated by *in situ* Raman and DFT calculations. As an effective additive for preventing polysulfide shuttling, catalysts are crucial research directions in Li-S batteries. In **Chapter 4**, we compared two different catalysts using the methodology we established in the earlier chapter to examine the role of catalysts in enhancing reaction kinetics and customizing reaction pathways. N,S-HGF shows superior catalytic effects on polysulfide conversion thus results in faster polysulfide depletion under higher voltages and smaller overpotentials, corroborated by interpretations from both CV and *in situ* Raman. Following that, a different class of materials, porous N-doped carbons, were examined as catalysts by CV analysis in Li-S batteries in **Chapter 5**. Utilizing information from both NMR and DFT, it was possible to study and categorize the actions of various N moieties on catalytic sulfur reduction. On the atomic level, we discovered that a particular type of pyridinic N might provide a far stronger catalytic effect on sulfur conversion. In **Chapter 6**, take a step forward, we progress from lithium to sodium, which has a lower price and is a promising replacement in metal sulfur batteries. However, because research on sodium-sulfur batteries is still in its early stages, we decided to address the primary issue, shuttling, first by regulating cell components such as the separator. Here, we primarily focused on various 2D materials and two technical approaches for separator engineering in order to physically or catalytically capture polysulfides in cathodes and consequently increase the capacity and stability of the cell. By combining all of these investigations, we acquired a more comprehensive understanding of the fundamentals of metal sulfur batteries, and these findings could be extremely insightful for the rational design of high energy density metal sulfur batteries in the future to improve their performance as next generation energy storage devices.

REFERENCES

1 Nalley, S. & LaRose, A. Annual Energy Outlook 2022. (U.S. Energy Information Administration, Bipartisan Policy Center, 2022).

2 Roy, P. & Srivastava, S. K. Nanostructured anode materials for lithium ion batteries. *Journal of Materials Chemistry A* **3**, 2454-2484 (2015).

3 Nitta, N., Wu, F., Lee, J. T. & Yushin, G. Li-ion battery materials: present and future. *Materials Today* **18**, 252-264 (2015).

4 Goodenough, J. B. & Kim, Y. Challenges for Rechargeable Li Batteries. *Chemistry of Materials* **22**, 587-603 (2009).

5 Sun, H. *et al.* Hierarchical 3D electrodes for electrochemical energy storage. *Nature Reviews Materials* **4**, 45-60 (2018).

6 Simon, P. & Gogotsi, Y. Materials for electrochemical capacitors. *Nature Materials* **7**, 845-854 (2008).

7 Zhong, C. *et al.* A review of electrolyte materials and compositions for electrochemical supercapacitors. *Chemical Society Reviews* **44**, 7484-7539 (2015).

8 Armand, M. & Tarascon, J. M. Building better batteries. *Nature* **451**, 652-657 (2008).

9 Global EV Outlook 2022. (International Energy Agency, 2022).

10 Nayak, P. K., Yang, L., Brehm, W. & Adelhelm, P. From Lithium-Ion to Sodium-Ion Batteries: Advantages, Challenges, and Surprises. *Angewandte Chemie International Edition* **57**, 102-120 (2018).

11 Liu, C., Neale, Z. G. & Cao, G. Understanding electrochemical potentials of cathode materials in rechargeable batteries. *Materials Today* **19**, 109-123 (2016).

12 Ji, L., Lin, Z., Alcoutlabi, M. & Zhang, X. Recent developments in nanostructured anode materials for rechargeable lithium-ion batteries. *Energy & Environmental Science* **4**, 2682-2699 (2011).

13 Team, M. E. V. A Guide to Understanding Battery Specifications. (2008).

14 Duffner, F. *et al.* Post-lithium-ion battery cell production and its compatibility with lithium-ion cell production infrastructure. *Nature Energy* **6**, 123-134 (2021).

15 Gao, B. *et al.* Electrochemical intercalation of single-walled carbon nanotubes with lithium. *Chemical physics letters* **307**, 153-157 (1999).

16 Wu, C. *et al.* Boosting performance of Co-free Li-rich cathode material through regulating the anionic activity by means of the strong TaO bonding. *Journal of Colloid and Interface Science* **628**, 1031-1040 (2022).

17 Wu, H. & Cui, Y. Designing nanostructured Si anodes for high energy lithium ion batteries. *Nano Today* **7**, 414-429 (2012).

18 Martin, C. Driving change in the battery industry. *Nature nanotechnology* **9**, 327-328 (2014).

19 Chan, C. K. *et al.* High-performance lithium battery anodes using silicon nanowires. *Nature nanotechnology* **3**, 31-35 (2008).

20 Wu, H. *et al.* Stable cycling of double-walled silicon nanotube battery anodes through solid–electrolyte interphase control. *Nature nanotechnology* **7**, 310-315 (2012).

21 Houache, M. S., Yim, C.-H., Karkar, Z. & Abu-Lebdeh, Y. On the Current and Future Outlook of Battery Chemistries for Electric Vehicles—Mini Review. *Batteries* **8**, 70 (2022).

22 Cheng, X.-B., Zhang, R., Zhao, C.-Z. & Zhang, Q. Toward safe lithium metal anode in rechargeable batteries: a review. *Chemical reviews* **117**, 10403-10473 (2017).

23 Qian, J. *et al.* High rate and stable cycling of lithium metal anode. *Nature communications* **6**, 1-9 (2015).

24 Lin, D., Liu, Y. & Cui, Y. Reviving the lithium metal anode for high-energy batteries. *Nature Nanotechnology* **12**, 194-206 (2017).

25 Bruce, P. G., Freunberger, S. A., Hardwick, L. J. & Tarascon, J.-M. Li–O2 and Li–S batteries with high energy storage. *Nature Materials* **11**, 19-29 (2012).

26 Aurbach, D., McCloskey, B. D., Nazar, L. F. & Bruce, P. G. Advances in understanding mechanisms underpinning lithium–air batteries. *Nature Energy* **1**, 16128 (2016).

27 Girishkumar, G., McCloskey, B., Luntz, A. C., Swanson, S. & Wilcke, W. Lithium−Air Battery: Promise and Challenges. *The Journal of Physical Chemistry Letters* **1**, 2193-2203 (2010).

28 Chen, K., Yang, D.-Y., Huang, G. & Zhang, X.-B. Lithium–Air Batteries: Air-Electrochemistry and Anode Stabilization. *Accounts of Chemical Research* **54**, 632-641 (2021).

29 Zhu, Y.-F., Xiao, Y., Dou, S.-X., Kang, Y.-M. & Chou, S.-L. Spinel/post-spinel engineering on layered oxide cathodes for sodium-ion batteries. *eScience* (2021).

30 Yabuuchi, N., Kubota, K., Dahbi, M. & Komaba, S. Research development on sodium-ion batteries. *Chemical reviews* **114**, 11636-11682 (2014).

31 Vaalma, C., Buchholz, D., Weil, M. & Passerini, S. A cost and resource analysis of sodium-ion batteries. *Nature Reviews Materials* **3**, 18013 (2018).

32 Hwang, J.-Y., Myung, S.-T. & Sun, Y.-K. Sodium-ion batteries: present and future. *Chemical Society Reviews* **46**, 3529-3614 (2017).

33 Herbert, D. & Ulam, J. Electric dry cells and storage batteries. *US Patent A* **3043896** (1962).

34 Manthiram, A., Fu, Y., Chung, S. H., Zu, C. & Su, Y. S. Rechargeable lithium-sulfur batteries. *Chem Rev* **114**, 11751-11787 (2014).

35 Seh, Z. W., Sun, Y., Zhang, Q. & Cui, Y. Designing high-energy lithium–sulfur batteries. *Chemical Society Reviews* **45**, 5605-5634 (2016).

36 Chung, S. H. & Manthiram, A. Current Status and Future Prospects of Metal-Sulfur Batteries. *Adv Mater* **31**, e1901125 (2019).

37 Bhargav, A., He, J., Gupta, A. & Manthiram, A. Lithium-sulfur batteries: attaining the critical metrics. *Joule* **4**, 285-291 (2020).

38 Yin, Y. X., Xin, S., Guo, Y. G. & Wan, L. J. Lithium-sulfur batteries: electrochemistry, materials, and prospects. *Angew Chem Int Ed Engl* **52**, 13186-13200 (2013).

39 Li, Z., Zhou, Y., Wang, Y. & Lu, Y. C. Solvent-mediated Li2S electrodeposition: a critical manipulator in lithium–sulfur batteries. *Advanced Energy Materials* **9**, 1802207 (2019).

40 Ma, L., Hendrickson, K. E., Wei, S. & Archer, L. A. Nanomaterials: Science and applications in the lithium–sulfur battery. *Nano Today* **10**, 315-338 (2015).

41 Li, G. *et al.* Revisiting the role of polysulfides in lithium–sulfur batteries. *Advanced Materials* **30**, 1705590 (2018).

42 Huang, L. *et al.* Electrode design for lithium–sulfur batteries: problems and solutions. *Advanced Functional Materials* **30**, 1910375 (2020).

43 Rosenman, A. *et al.* Review on Li-sulfur battery systems: An integral perspective. *Advanced Energy Materials* **5**, 1500212 (2015).

44 Wang, H. *et al.* Graphene-wrapped sulfur particles as a rechargeable lithium–sulfur battery cathode material with high capacity and cycling stability. *Nano letters* **11**, 2644-2647 (2011).

45 Kannan, S. K., Hareendrakrishnakumar, H., Joseph, J. & Joseph, M. G. Synergistic Restriction to Polysulfides by a Carbon Nanotube/Manganese Sulfide-Decorated Separator for Advanced Lithium–Sulfur Batteries. *Energy & Fuels* **36**, 8460-8470 (2022).

46 Ding, F. *et al.* Dendrite-free lithium deposition via self-healing electrostatic shield mechanism. *Journal of the American Chemical Society* **135**, 4450-4456 (2013).

47 Li, G., Hu, J., Li, G., Ye, S. & Gao, X. Sulfur/activated-conductive carbon black composites as cathode materials for lithium/sulfur battery. *Journal of power sources* **240**, 598-605 (2013).

48 Fu, Y., Zu, C. & Manthiram, A. In situ-formed Li2S in lithiated graphite electrodes for lithium–sulfur batteries. *Journal of the American Chemical Society* **135**, 18044-18047 (2013).

49 Yu, M., Li, R., Wu, M. & Shi, G. Graphene materials for lithium–sulfur batteries. *Energy Storage Materials* **1**, 51-73 (2015).

50 Fang, R. *et al.* The regulating role of carbon nanotubes and graphene in lithium-ion and lithium–sulfur batteries. *Advanced materials* **31**, 1800863 (2019).

51 Yuan, Z. *et al.* Hierarchical free-standing carbon-nanotube paper electrodes with ultrahigh sulfur-loading for lithium–sulfur batteries. *Advanced Functional Materials* **24**, 6105-6112 (2014).

52 Singhal, R., Chung, S.-H., Manthiram, A. & Kalra, V. A free-standing carbon nanofiber interlayer for high-performance lithium–sulfur batteries. *Journal of Materials Chemistry A* **3**, 4530-4538 (2015).

53 Zheng, G. *et al.* Amphiphilic surface modification of hollow carbon nanofibers for improved cycle life of lithium sulfur batteries. *Nano letters* **13**, 1265-1270 (2013).

54 Papandrea, B. *et al.* Three-dimensional graphene framework with ultra-high sulfur content for a robust lithium–sulfur battery. *Nano research* **9**, 240-248 (2016).

55 Jiang, Y. *et al.* Inhibiting the shuttle effect of Li–S battery with a graphene oxide coating separator: Performance improvement and mechanism study. *Journal of Power Sources* **342**, 929-938 (2017).

56 Xu, G. *et al.* A thin multifunctional coating on a separator improves the cyclability and safety of lithium sulfur batteries. *Chemical science* **8**, 6619-6625 (2017).

57 Li, Z. *et al.* A polar TiO/MWCNT coating on a separator significantly suppress the shuttle effect in a lithium-sulfur battery. *Electrochimica Acta* **310**, 1-12 (2019).

58 Zhang, Y. *et al.* A graphene-oxide-based thin coating on the separator: an efficient barrier towards high-stable lithium–sulfur batteries. *2D Materials* **2**, 024013 (2015).

59 Zeng, P. *et al.* Enhanced catalytic conversion of polysulfides using bimetallic Co7Fe3 for high-performance lithium–sulfur batteries. *ACS nano* **14**, 11558-11569 (2020).

60 Zhong, Y. *et al.* Surface Chemistry in Cobalt Phosphide-Stabilized Lithium-Sulfur Batteries. *J Am Chem Soc* **140**, 1455-1459 (2018).

61 Yuan, Z. *et al.* Powering lithium–sulfur battery performance by propelling polysulfide redox at sulfiphilic hosts. *Nano letters* **16**, 519-527 (2016).

62 Liu, D. *et al.* Catalytic effects in lithium–sulfur batteries: promoted sulfur transformation and reduced shuttle effect. *Advanced science* **5**, 1700270 (2018).

63 Zhao, Y. *et al.* A Nitrogen-Doped Carbon Matrix Aiming at Inhibiting Polysulfide Shuttling for Lithium–Sulfur Batteries. *Energy & Fuels* **34**, 10188-10195 (2020).

64 Du, Z. *et al.* Cobalt in Nitrogen-Doped Graphene as Single-Atom Catalyst for High-Sulfur Content Lithium-Sulfur Batteries. *J Am Chem Soc* **141**, 3977-3985 (2019).

65 Al Salem, H., Babu, G., Rao, C. V. & Arava, L. M. Electrocatalytic Polysulfide Traps for Controlling Redox Shuttle Process of Li-S Batteries. *J Am Chem Soc* **137**, 11542-11545 (2015).

66 Tao, X. *et al.* Balancing surface adsorption and diffusion of lithium-polysulfides on nonconductive oxides for lithium–sulfur battery design. *Nature communications* **7**, 1-9 (2016).

67 Li, H. *et al.* Ultra-thin Fe3C nanosheets promote the adsorption and conversion of polysulfides in lithium-sulfur batteries. *Energy storage materials* **18**, 338-348 (2019).

68 Zhao, M. *et al.* Electrochemical phase evolution of metal-based pre-catalysts for high-rate polysulfide conversion. *Angewandte Chemie* **132**, 9096-9102 (2020).

69 Li, C. *et al.* Conductive and Polar Titanium Boride as a Sulfur Host for Advanced Lithium–Sulfur Batteries. *Chemistry of Materials* **30**, 6969-6977 (2018).

70 Peng, L. *et al.* A fundamental look at electrocatalytic sulfur reduction reaction. *Nature Catalysis* **3**, 762-770 (2020).

71 Zhao, C.-Z. *et al.* Li2S5-based ternary-salt electrolyte for robust lithium metal anode. *Energy Storage Materials* **3**, 77-84 (2016).

72 Yan, C. *et al.* Lithium metal protection through in-situ formed solid electrolyte interphase in lithium-sulfur batteries: The role of polysulfides on lithium anode. *Journal of Power Sources* **327**, 212-220 (2016).

73 Li, W. *et al.* The synergetic effect of lithium polysulfide and lithium nitrate to prevent lithium dendrite growth. *Nature communications* **6**, 1-8 (2015).

74 Zhang, S. S. Role of LiNO3 in rechargeable lithium/sulfur battery. *Electrochimica Acta* **70**, 344-348 (2012).

75 Kang, H.-K. *et al.* Few-layer graphene island seeding for dendrite-free Li metal electrodes. *Acs Applied Materials & Interfaces* **8**, 26895-26901 (2016).

76 Yan, K. *et al.* Ultrathin two-dimensional atomic crystals as stable interfacial layer for improvement of lithium metal anode. *Nano letters* **14**, 6016-6022 (2014).

77 Kim, Y. *et al.* Two-dimensional phosphorene-derived protective layers on a lithium metal anode for lithium-oxygen batteries. *ACS nano* **12**, 4419-4430 (2018).

78 Bobnar, J. *et al.* Fluorinated reduced graphene oxide as a protective layer on the metallic lithium for application in the high energy batteries. *Scientific reports* **8**, 1-10 (2018).

79 Cha, E. *et al.* 2D MoS2 as an efficient protective layer for lithium metal anodes in high-performance Li–S batteries. *Nature nanotechnology* **13**, 337-344 (2018).

80 Lin, D. *et al.* Layered reduced graphene oxide with nanoscale interlayer gaps as a stable host for lithium metal anodes. *Nature nanotechnology* **11**, 626-632 (2016).

81 Su, Y.-S., Fu, Y., Cochell, T. & Manthiram, A. A strategic approach to recharging lithium-sulphur batteries for long cycle life. *Nature communications* **4**, 1-8 (2013).

82 Huang, X. *et al.* Cyclic voltammetry in lithium–sulfur batteries—challenges and opportunities. *Energy Technology* **7**, 1801001 (2019).

83 Cuisinier, M. *et al.* Sulfur Speciation in Li–S Batteries Determined by Operando X-ray Absorption Spectroscopy. *The Journal of Physical Chemistry Letters* **4**, 3227-3232 (2013).

84 Zou, Q. & Lu, Y. C. Solvent-Dictated Lithium Sulfur Redox Reactions: An Operando UV-vis Spectroscopic Study. *J Phys Chem Lett* **7**, 1518-1525 (2016).

85 Assary, R. S., Curtiss, L. A. & Moore, J. S. Toward a Molecular Understanding of Energetics in Li–S Batteries Using Nonaqueous Electrolytes: A High-Level Quantum Chemical Study. *The Journal of Physical Chemistry C* **118**, 11545-11558 (2014).

86 Lu, Y.-C., He, Q. & Gasteiger, H. A. Probing the Lithium–Sulfur Redox Reactions: A Rotating-Ring Disk Electrode Study. *The Journal of Physical Chemistry C* **118**, 5733-5741 (2014).

87 Barchasz, C. *et al.* Lithium/sulfur cell discharge mechanism: an original approach for intermediate species identification. *Anal Chem* **84**, 3973-3980 (2012).

88 Zheng, D. *et al.* Investigation of the Li–S battery mechanism by real-time monitoring of the changes of sulfur and polysulfide species during the discharge and charge. *ACS applied materials & interfaces* **9**, 4326-4332 (2017).

89 Dominko, R. *et al.* Polysulfides formation in different electrolytes from the perspective of X-ray absorption spectroscopy. *Journal of The Electrochemical Society* **165**, A5014 (2017).

90 Conder, J. *et al.* Direct observation of lithium polysulfides in lithium-sulfur batteries using operando X-ray diffraction. *Nature Energy* **2** (2017).

91 Lei, T. *et al.* Inhibiting Polysulfide Shuttling with a Graphene Composite Separator for Highly Robust Lithium-Sulfur Batteries. *Joule* **2**, 2091-2104 (2018).

92 Hagen, M. *et al.* In-Situ Raman Investigation of Polysulfide Formation in Li-S Cells. *Journal of the Electrochemical Society* **160**, A1205-A1214 (2013).

93 Chen, W. *et al.* A New Hydrophilic Binder Enabling Strongly Anchoring Polysulfides for High-Performance Sulfur Electrodes in Lithium-Sulfur Battery. *Advanced Energy Materials* **8**, 1702889 (2018).

94 Wu, H. L., Huff, L. A. & Gewirth, A. A. In situ Raman spectroscopy of sulfur speciation in lithium-sulfur batteries. *ACS Appl Mater Interfaces* **7**, 1709-1719 (2015).

95 Zhang, L. *et al.* In situ optical spectroscopy characterization for optimal design of lithium–sulfur batteries. *Chemical Society Reviews* **48**, 5432-5453 (2019).

96 Chen, J.-J. *et al.* Conductive Lewis Base Matrix to Recover the Missing Link of Li2S8 during the Sulfur Redox Cycle in Li–S Battery. *Chemistry of Materials* **27**, 2048-2055 (2015).

97 Chen, H. *et al.* Progress in electrical energy storage system: A critical review. *Progress in natural science* **19**, 291-312 (2009).

98 Chu, C. *et al.* Recent advanced skeletons in sodium metal anodes. *Energy & Environmental Science* (2021).

99 Sun, B. *et al.* Design strategies to enable the efficient use of sodium metal anodes in high-energy batteries. *Advanced Materials* **32**, 1903891 (2020).

100 Wang, N. *et al.* High-performance room-temperature sodium–sulfur battery enabled by electrocatalytic sodium polysulfides full conversion. *Energy & Environmental Science* **13**, 562-570 (2020).

101 Yu, X. & Manthiram, A. A progress report on metal–sulfur batteries. *Advanced Functional Materials* **30**, 2004084 (2020).

102 Eng, A. Y. S. *et al.* Room-temperature sodium–sulfur batteries and beyond: realizing practical high energy systems through anode, cathode, and electrolyte engineering. *Advanced Energy Materials* **11**, 2003493 (2021).

103 Xu, X. *et al.* A room-temperature sodium–sulfur battery with high capacity and stable cycling performance. *Nature communications* **9**, 1-12 (2018).

104 Zhang, B.-W. *et al.* Atomic cobalt as an efficient electrocatalyst in sulfur cathodes for superior room-temperature sodium-sulfur batteries. *Nature communications* **9**, 1-11 (2018).

105 Yan, Z. *et al.* Nickel sulfide nanocrystals on nitrogen-doped porous carbon nanotubes with high-efficiency electrocatalysis for room-temperature sodium-sulfur batteries. *Nature communications* **10**, 1-8 (2019).

106 Li, X., Yu, J., Wageh, S., Al-Ghamdi, A. A. & Xie, J. Graphene in photocatalysis: a review. *Small* **12**, 6640-6696 (2016).

107 Novoselov, K. S. *et al.* Electric field effect in atomically thin carbon films. *science* **306**, 666-669 (2004).

108 Nair, R. R. *et al.* Fine structure constant defines visual transparency of graphene. *science* **320**, 1308-1308 (2008).

109 Stoller, M. D., Park, S., Zhu, Y., An, J. & Ruoff, R. S. Graphene-based ultracapacitors. *Nano letters* **8**, 3498-3502 (2008).

110 Bolotin, K. I. *et al.* Ultrahigh electron mobility in suspended graphene. *Solid state communications* **146**, 351-355 (2008).

111 Raccichini, R., Varzi, A., Passerini, S. & Scrosati, B. The role of graphene for electrochemical energy storage. *Nature materials* **14**, 271-279 (2015).

112 Zhou, G. *et al.* Graphene-wrapped Fe3O4 anode material with improved reversible capacity and cyclic stability for lithium ion batteries. *Chemistry of materials* **22**, 5306-5313 (2010).

113 Kumar, R. *et al.* Heteroatom doped graphene engineering for energy storage and conversion. *Materials Today* **39**, 47-65 (2020).

114 Wu, Z.-S. *et al.* Graphene/metal oxide composite electrode materials for energy storage. *Nano Energy* **1**, 107-131 (2012).

115 Meng, X. *et al.* Cobalt sulfide/graphene composite hydrogel as electrode for high-performance pseudocapacitors. *Scientific reports* **6**, 1-9 (2016).

116 Sun, Z. *et al.* Conductive porous vanadium nitride/graphene composite as chemical anchor of polysulfides for lithium-sulfur batteries. *Nature Communications* **8**, 14627 (2017).

117 Das, T. K. & Prusty, S. Graphene-Based Polymer Composites and Their Applications. *Polymer-Plastics Technology and Engineering* **52**, 319-331 (2013).

118 Xu, Y. *et al.* Holey graphene frameworks for highly efficient capacitive energy storage. *Nature communications* **5**, 1-8 (2014).

119 Xu, Y. *et al.* Solution processable holey graphene oxide and its derived macrostructures for high-performance supercapacitors. *Nano letters* **15**, 4605-4610 (2015).

120 Yi, M. & Shen, Z. A review on mechanical exfoliation for the scalable production of graphene. *Journal of Materials Chemistry A* **3**, 11700-11715 (2015).

121 Chen, J., Yao, B., Li, C. & Shi, G. An improved Hummers method for eco-friendly synthesis of graphene oxide. *Carbon* **64**, 225-229 (2013).

122 Zhang, L. *et al.* Size-controlled synthesis of graphene oxide sheets on a large scale using chemical exfoliation. *Carbon* **47**, 3365-3368 (2009).

123 Deng, B., Liu, Z. & Peng, H. Toward Mass Production of CVD Graphene Films. *Advanced Materials* **31**, 1800996 (2019).

124 Antonatos, N., Ghodrati, H. & Sofer, Z. Elements beyond graphene: Current state and perspectives of elemental monolayer deposition by bottom-up approach. *Applied Materials Today* **18**, 100502 (2020).

125 Gupta, B. *et al.* Role of oxygen functional groups in reduced graphene oxide for lubrication. *Sci Rep* **7**, 45030 (2017).

126 Yan, J.-A. & Chou, M. Y. Oxidation functional groups on graphene: Structural and electronic properties. *Physical Review B* **82**, 125403 (2010).

127 Sun, H. *et al.* Three-dimensional holey-graphene/niobia composite architectures for ultrahigh-rate energy storage. *Science* **356**, 599-604 (2017).

128 Xu, Y., Sheng, K., Li, C. & Shi, G. Self-assembled graphene hydrogel via a one-step hydrothermal process. *ACS nano* **4**, 4324-4330 (2010).

129 Wang, Z. *et al.* Effect of drying conditions on the structure of three-dimensional N-doped graphene and its electrochemical performance. *RSC Advances* **5**, 19838-19843 (2015).

130 Pan, Z. *et al.* Achieving commercial-level mass loading in ternary-doped holey graphene hydrogel electrodes for ultrahigh energy density supercapacitors. *Nano Energy* **46**, 266-276 (2018).

131 Zhou, G. M., Paek, E., Hwang, G. S. & Manthiram, A. Long-life Li/polysulphide batteries with high sulphur loading enabled by lightweight three-dimensional nitrogen/sulphur-codoped graphene sponge. *Nature Communications* **6** (2015).

132 Verma, P., Maire, P. & Novák, P. A review of the features and analyses of the solid electrolyte interphase in Li-ion batteries. *Electrochimica Acta* **55**, 6332-6341 (2010).

133 Fang, R. *et al.* More Reliable Lithium-Sulfur Batteries: Status, Solutions and Prospects. *Advanced Materials* **29**, 1606823 (2017).

134 Pang, Q., Liang, X., Kwok, C. Y. & Nazar, L. F. Advances in lithium-sulfur batteries based on multifunctional cathodes and electrolytes. *Nature Energy* **1** (2016).

135 Zhang, S. S. Liquid electrolyte lithium/sulfur battery: Fundamental chemistry, problems, and solutions. *Journal of Power Sources* **231**, 153-162 (2013).

136 Aurbach, D. *et al.* On the surface chemical aspects of very high energy density, rechargeable Li–sulfur batteries. *Journal of the Electrochemical Society* **156**, A694 (2009).

137 Jaumann, T. *et al.* Role of 1, 3-dioxolane and LiNO3 addition on the long term stability of nanostructured silicon/carbon anodes for rechargeable lithium batteries. *Journal of The Electrochemical Society* **163**, A557 (2016).

138 Gofer, Y., Ely, Y. E. & Aurbach, D. Surface chemistry of lithium in 1, 3-dioxolane. *Electrochimica acta* **37**, 1897-1899 (1992).

139 Rosenman, A. *et al.* The Effect of Interactions and Reduction Products of LiNO3, the Anti-Shuttle Agent, in Li-S Battery Systems. *Journal of The Electrochemical Society* **162**, A470 (2015).

140 Shim, J., Ko, T. J. & Yoo, K. Study for an effect of LiNO3 on polysulfide multistep reaction in Li/S battery. *Journal of Industrial and Engineering Chemistry* **80**, 283-291 (2019).

141 Ye, Y. *et al.* Lithium nitrate: A double-edged sword in the rechargeable lithium-sulfur cell. *Energy Storage Materials* **16**, 498-504 (2019).

142 Xie, X. & Gao, L. Characterization of a manganese dioxide/carbon nanotube composite fabricated using an in situ coating method. *Carbon* **45**, 2365-2373 (2007).

143 Chen, W., Fan, Z., Gu, L., Bao, X. & Wang, C. Enhanced capacitance of manganese oxide via confinement inside carbon nanotubes. *Chemical Communications* **46**, 3905-3907 (2010).

144 Mikhaylik, Y. V. & Akridge, J. R. Polysulfide shuttle study in the Li/S battery system. *Journal of the Electrochemical Society* **151**, A1969-A1976 (2004).

145 Sun, Z. *et al.* Conductive porous vanadium nitride/graphene composite as chemical anchor of polysulfides for lithium-sulfur batteries. *Nat Commun* **8**, 14627 (2017).

146 Xu, Z. L. *et al.* Exceptional catalytic effects of black phosphorus quantum dots in shuttling-free lithium sulfur batteries. *Nat Commun* **9**, 4164 (2018).

147 Ji, X., Lee, K. T. & Nazar, L. F. A highly ordered nanostructured carbon–sulphur cathode for lithium–sulphur batteries. *Nature Materials* **8**, 500-506 (2009).

148 Jayaprakash, N., Shen, J., Moganty, S. S., Corona, A. & Archer, L. A. Porous hollow carbon@sulfur composites for high-power lithium-sulfur batteries. *Angew Chem Int Ed Engl* **50**, 5904-5908 (2011).

149 Jana, M. *et al.* Rational design of two-dimensional nanomaterials for lithium–sulfur batteries. *Energy & Environmental Science* **13**, 1049-1075 (2020).

150 Li, G. *et al.* Polysulfide Regulation by the Zwitterionic Barrier toward Durable Lithium-Sulfur Batteries. *J Am Chem Soc* **142**, 3583-3592 (2020).

151 Liu, F. *et al.* Dual redox mediators accelerate the electrochemical kinetics of lithium-sulfur batteries. *Nat Commun* **11**, 5215 (2020).

152 Wang, N. *et al.* Thickness-independent scalable high-performance Li-S batteries with high areal sulfur loading via electron-enriched carbon framework. *Nat Commun* **12**, 4519 (2021).

153 Wang, L. *et al.* A quantum-chemical study on the discharge reaction mechanism of lithium-sulfur batteries. *Journal of Energy Chemistry* **22**, 72-77 (2013).

154 He, Q., Freiberg, A. T. S., Patel, M. U. M., Qian, S. & Gasteiger, H. A. Operando Identification of Liquid Intermediates in Lithium-Sulfur Batteries via Transmission UV-vis Spectroscopy. *Journal of the Electrochemical Society* **167** (2020).

155 Wild, M. *et al.* Lithium sulfur batteries, a mechanistic review. *Energy & Environmental Science* **8**, 3477-3494 (2015).

156 Wujcik, K. H. *et al.* Fingerprinting Lithium-Sulfur Battery Reaction Products by X-ray Absorption Spectroscopy. *Journal of the Electrochemical Society* **161**, A1100-A1106 (2014).

157 Zhu, W. *et al.* Investigation of the reaction mechanism of lithium sulfur batteries in different electrolyte systems by in situ Raman spectroscopy and in situ X-ray diffraction. *Sustainable Energy & Fuels* **1**, 737-747 (2017).

158 Zhu, X. *et al.* A Highly Stretchable Cross-Linked Polyacrylamide Hydrogel as an Effective Binder for Silicon and Sulfur Electrodes toward Durable Lithium-Ion Storage. *Advanced Functional Materials* **28**, 1705015 (2018).

159 Zhu, X. *et al.* In Situ Assembly of 2D Conductive Vanadium Disulfide with Graphene as a High-Sulfur-Loading Host for Lithium–Sulfur Batteries. *Advanced Energy Materials* **8**, 1800201 (2018).

160 Huang, S. *et al.* Regulating the polysulfide redox conversion by iron phosphide nanocrystals for high-rate and ultrastable lithium-sulfur battery. *Nano Energy* **51**, 340-348 (2018).

161 Zhao, Q. *et al.* Sulfur Nanodots Electrodeposited on Ni Foam as High-Performance Cathode for Li–S Batteries. *Nano Letters* **15**, 721-726 (2015).

162 Song, Y. *et al.* Synchronous immobilization and conversion of polysulfides on a VO2–VN binary host targeting high sulfur load Li–S batteries. *Energy & Environmental Science* **11**, 2620-2630 (2018).

163 Song, Y. *et al.* Vanadium Dioxide-Graphene Composite with Ultrafast Anchoring Behavior of Polysulfides for Lithium–Sulfur Batteries. *ACS Applied Materials & Interfaces* **10**, 15733-15741 (2018).

164 Kresse, G. & Hafner, J. Ab initio molecular dynamics for liquid metals. *Physical review B* **47**, 558 (1993).

165 Sun, J., Ruzsinszky, A. & Perdew, J. P. Strongly constrained and appropriately normed semilocal density functional. *Physical review letters* **115**, 036402 (2015).

166 Mathew, K., Sundararaman, R., Letchworth-Weaver, K., Arias, T. & Hennig, R. G. Implicit solvation model for density-functional study of nanocrystal surfaces and reaction pathways. *The Journal of chemical physics* **140**, 084106 (2014).

167 Hannauer, J. *et al.* The Quest for Polysulfides in Lithium-Sulfur Battery Electrolytes: An Operando Confocal Raman Spectroscopy Study. *ChemPhysChem* **16**, 2709-2709 (2015).

168 He, J. *et al.* Freestanding 1T MoS2/graphene heterostructures as a highly efficient electrocatalyst for lithium polysulfides in Li–S batteries. *Energy & Environmental Science* **12**, 344-350 (2019).

169 Zheng, J. *et al.* Lewis Acid–Base Interactions between Polysulfides and Metal Organic Framework in Lithium Sulfur Batteries. *Nano Letters* **14**, 2345-2352 (2014).

170 Gong, K., Du, F., Xia, Z., Durstock, M. & Dai, L. Nitrogen-Doped Carbon Nanotube Arrays with High Electrocatalytic Activity for Oxygen Reduction. *Science* **323**, 760-764 (2009).

171 Liang, H.-W., Zhuang, X., Brüller, S., Feng, X. & Müllen, K. Hierarchically porous carbons with optimized nitrogen doping as highly active electrocatalysts for oxygen reduction. *Nature Communications* **5**, 4973 (2014).

172 Joo, S. H. *et al.* Ordered nanoporous arrays of carbon supporting high dispersions of platinum nanoparticles. *Nature* **412**, 169-172 (2001).

173 Zhu, Y. P., Guo, C., Zheng, Y. & Qiao, S.-Z. Surface and Interface Engineering of Noble-Metal-Free Electrocatalysts for Efficient Energy Conversion Processes. *Accounts of Chemical Research* **50**, 915-923 (2017).

174 Guo, D. *et al.* Active sites of nitrogen-doped carbon materials for oxygen reduction reaction clarified using model catalysts. *Science* **351**, 361-365 (2016).

175 Wang, D.-W. & Su, D. Heterogeneous nanocarbon materials for oxygen reduction reaction. *Energy & Environmental Science* **7**, 576-591 (2014).

176 Ding, W. *et al.* Space-Confinement-Induced Synthesis of Pyridinic- and Pyrrolic-Nitrogen-Doped Graphene for the Catalysis of Oxygen Reduction. *Angewandte Chemie International Edition* **52**, 11755-11759 (2013).

177 Wu, J. *et al.* Nitrogen-Doped Graphene with Pyridinic Dominance as a Highly Active and Stable Electrocatalyst for Oxygen Reduction. *ACS Applied Materials & Interfaces* **7**, 14763-14769 (2015).

178 Dorjgotov, A., Ok, J., Jeon, Y., Yoon, S.-H. & Shul, Y. G. Activity and active sites of nitrogen-doped carbon nanotubes for oxygen reduction reaction. *Journal of Applied Electrochemistry* **43**, 387-397 (2013).

179 Yu, X. & Manthiram, A. Capacity Enhancement and Discharge Mechanisms of Room-Temperature Sodium–Sulfur Batteries. *ChemElectroChem* **1**, 1275-1280 (2014).

180 Dong, C. *et al.* Enabling high-performance room-temperature sodium/sulfur batteries with few-layer 2H-MoSe2 embellished nitrogen-doped hollow carbon spheres as polysulfide barriers. *Journal of Materials Chemistry A* **9**, 3451-3463 (2021).

181 Dong, C. *et al.* Inhibited shuttle effect by functional separator for room-temperature sodium-sulfur batteries. *Journal of Materials Science & Technology* **113**, 207-216 (2022).

182 Wang, C. *et al.* Robust Room-Temperature Sodium-Sulfur Batteries Enabled by a Sandwich-Structured MXene@C/Polyolefin/MXene@C Dual-functional Separator. *Small* **18**, 2106983 (2022).

183 Chen, D., Wen, K., Lv, W., Wei, Z. & He, W. Separator Modification and Functionalization for Inhibiting the Shuttle Effect in Lithium-Sulfur Batteries. *physica status solidi (RRL) – Rapid Research Letters* **12**, 1800249 (2018).